CALCIUM AS A SECOND MESSENGER IN NEURONAL GROWTH CONES

Robin Angus Silver

A thesis submitted for the degree of
Doctor of Philosophy
in the
University of London

Department of Physiology
University College London
May 1990

ProQuest Number: 10630900

All rights reserved

INFORMATION TO ALL USERS
The quality of this reproduction is dependent upon the quality of the copy submitted.

In the unlikely event that the author did not send a complete manuscript
and there are missing pages, these will be noted. Also, if material had to be removed,
a note will indicate the deletion.

ProQuest 10630900

Published by ProQuest LLC (2017). Copyright of the Dissertation is held by the Author.

All rights reserved.
This work is protected against unauthorized copying under Title 17, United States Code
Microform Edition © ProQuest LLC.

ProQuest LLC.
789 East Eisenhower Parkway
P.O. Box 1346
Ann Arbor, MI 48106 – 1346

Abstract

Calcium is thought to be involved in the regulation of motility and growth in the neuronal growth cone. The aim of this work was to investigate the role of cytosolic free calcium concentration ($[Ca^{2+}]_i$) and voltage-gated calcium influx in controlling growth cone behaviour and neurite elongation. $[Ca^{2+}]_i$ and voltage-gated calcium influx was measured using digital imaging fluorescence microscopy (DIFM) and the whole-cell patch-clamp technique.

The behaviour of growth cones of N1E-115 mouse neuroblastoma was observed and categorized into five classes. The spatial distribution of $[Ca^{2+}]_i$ associated with these behavioural states was measured. True growth occurred only at the lowest $[Ca^{2+}]_i$ levels. Any spontaneous elevation of $[Ca^{2+}]_i$ above this level was associated with an inhibition of neurite elongation. Large elevations of $[Ca^{2+}]_i$ were associated with specific morphological changes.

L- and T-type voltage gated calcium currents were measured during differentiation. All cells possessing neurites had T-type currents. T-type current density was higher in cells with neurites than in cells without. There was no other detectable change in the characteristics of either current during differentiation.

The spatial distribution of voltage-dependent calcium influx through L- and T-type channels was measured at the growth cone. L-type channels were found to be clustered in the growth cone membrane, whereas T-type channels were uniformly distributed. Activation of L-channel clusters caused $[Ca^{2+}]_i$ 'hotspots' in which $[Ca^{2+}]_i$ rose to micromolar levels during 1 s depolarizations. Localized morphological changes at the site of the hotspot were observed during action potentials.

Preface

The complex nature of the experiments described in this thesis required that some of them be carried out in collaboration with others. Apart from this necessary help (see below) all the thesis is my work: I was responsible, with normal supervision, for initiating the work described, doing the experiments and analysing the results. All the writing was done by me.

In Chapter 3, cell counting for figure 3.1 was done by Dr S. Bolsover. In chapter 4, 30% of the experiments were done in collaboration with either Dr S. Bolsover or Ms A. Lamb; I manipulated the cells while my co-workers controlled the computer. The actin control experiment was done with Dr S. Bolsover and Dr M. Dickens. I did almost all the analysis for the chapter.

In Chapter 5, Dr S. Bolsover or Ms A. Lamb controlled the Microvax computer and I did the patch clamping, all the patch-clamp analysis and about 50% of the image analysis.

R. Angus Silver (candidate)   Stephen Bolsover (supervisor)

Contents

Abstract 2

Preface 3

Contents 4

List of figures 9

List of tables 11

Acknowledgements 12

Publications 13

Abbreviations 14

Chapter 1 Introduction 16

1.1 What is a neuronal growth cone? 16

1.2 Why are growth cones interesting? 17

1.3 Calcium regulation in the growth cone 19

1.4 The role of $[Ca^{2+}]_i$ in neurite outgrowth and growth cone motility: A historical review 22

1.5 The significance of this study 28

Chapter 2 Methods 31

2.1 The digital imaging fluorescence microscope 31

2.1.1 Calibration of the camera linearity and image processor acquisition rate 34

2.2 Spatial resolution of the digital imaging fluorescence microscope 37

2.2.1 Calculation of the resolution for point fluorescent images 37

2.2.2 Measurement of depth of focus for a point source 37
2.2.3 Outline of the problem of resolution with three-dimensional fluorescent sources 37
2.2.4 Measurement of the point spread function 40
2.2.5 The contribution of defocused information from any given plane 47
2.2.6 The spatial resolution of images of three-dimensional fluorescent specimens 47
2.3 Calcium measurement using a fluorescent dye 51
2.3.1 The basis of calcium ion measurement using a fluorescent probe 51
2.3.2 Spectrofluorimetry measurements using fura-2 52
2.3.3 Calculation of calcium concentration using the ratio method 55
2.3.4 Calibration of the DIFM for $[Ca^{2+}]_i$ measurement 56
2.3.5 Calculation of calcium changes using the single wavelength method 57
2.3.6 Calculation of dye concentration 64
2.3.7 Problems encountered using quantitative fluorescent measurement 64
2.4 Cell culture 67
2.5 Correlation of growth cone behavioural states with $[Ca^{2+}]_i$ 67
2.5.1 Experimental procedure.. 67
2.5.2 Image analysis 68
2.5.3 Control experiments 69
2.6 Measurement of calcium currents in differentiated N1E-115 cells 69
2.6.1 Whole-cell patch-clamp recording 69

2.6.2 Measurement of capacitance and series resistance when whole-cell patch-clamping 73
2.6.3 Separation of T- and L-type calcium currents using two voltage protocols 74
2.6.4 Data acquisition and analysis 81
2.6.5 Voltage-clamp quality in differentiated N1E-115 cells 81
2.7 Simultaneous patch-clamp and single wavelength imaging 82
2.8 Microelectrode and single wavelength recording 82
2.9 Statistical treatment 83

Chapter 3 Correlation of calcium currents with morphological differentiation in N1E-115 cells 84
3.1 Calcium currents in N1E-115 neuroblastoma cells 84
3.2 L-type current washout 85
3.3 Correlation of calcium currents with morphology 85
3.3.1 The T-type current 85
3.3.2 The L-type current 88
3.4 Differentiation induced by dibutyryl cyclic AMP 91
3.5 Discussion of the results: calcium currents and morphological differentiation. 91
3.5.1 T-type currents 92
3.5.2 L-type currents 92
3.5.3 Agent used to differentiate cells 93
Chapter 4 Correlation of neuronal growth cone behaviour with cytosolic calcium concentration 94
4.1 Growth cone behavioural states 94
4.2 Measurement of $[Ca^{2+}]_i$ in neuronal growth cones 95

4.2.1 Injection of fura-2 does not distort $[Ca^{2+}]_i$ 95

4.2.2 Quiescent growth cones 96

4.2.3 Motile advancing growth cones 96

4.2.4 Motile non-advancing growth cones 101

4.2.5 Flattening growth cones 104

4.2.6 Retracting growth cones 104

4.3 Spatial gradients of $[Ca^{2+}]_i$ 109

4.4 Control experiments 113

4.4.1 Control for the effect of DMSO on behaviour and $[Ca^{2+}]_i$ 113

4.4.2 Injection of ANTS 116

4.4.3 Fura-2 AM loading 116

4.5 Discussion of results: correlation of growth cone behaviour with $[Ca^{2+}]_i$ 121

Chapter 5 The spatial distribution of voltage-gated calcium influx and associated morphological changes at the neuronal growth cone 125

5.1 Changes in fluorescence intensity at the growth cone indicate a change in $[Ca^{2+}]_i$ 125

5.2 The spatial distribution of calcium influx through L- and T-type channels in the neuronal growth cone 126

5.2.1 $[Ca^{2+}]_i$ changes caused by influx through L-type channels 126

5.2.2 $[Ca^{2+}]_i$ changes caused by influx through T-type channels 130

5.2.3 Different spatial distributions of $[Ca^{2+}]_i$ caused by activation of L- and T-type channels occur during small $[Ca^{2+}]_i$ changes 130

5.3 Morphological changes associated with localized voltage gated calcium influx 133

5.3.1 Correlation of hotspot position and growth cone shape 133

5.3.2 Hotspot activation causes localized margin outgrowth 133

5.4 Discussion of results: the spatial distribution of voltage-gated calcium influx in the neuronal growth cone 136

5.4.1 The mechanism of 'hotspot' formation 137

Chapter 6 Discussion 139

6.1 How do growth cones grow? 139

6.2 What are the molecular events underlying growth cone growth and neurite elongation? 140

6.3 How do growth cones navigate? 149

6.3.1 Extrinsic factors: adhesive substrates 150

6.3.2 Neuronal guide-posts 151

6.3.3 Diffusible factors 151

6.3.4 Are intracellular $[Ca^{2+}]_i$ gradients likely to be important *in vivo*? 152

6.3.5 Intrinsic factors: the cytoskeleton 154

6.3.6 Electrical activity 155

6.4 Are $[Ca^{2+}]_i$ hotspots precursors to active zones? 155

6.5 How important is $[Ca^{2+}]_i$ to growth cone growth? A summary 156

References 157

List of Figures

Chapter 2

2.1 Schematic diagram of the digital fluorescence microscope 32

2.2 Characterization of the SIT camera input-output relation and gain 35

2.3 Intensity fall off from a point source with distance from the focal plane 38

2.4 Schematic diagram of light collection from a spherical cell injected with fura-2 41

2.5 Intensity profile cross-sections for focal planes above a point source 43

2.6 The point spread function 45

2.7 Point fluorescence intensity as a function of dye drop thickness 48

2.8 Fura-2 excitation spectrum *in vitro* and *in vivo* 53

2.9 Calibration of ratio units 59

2.10 Capacity transient analysis 71

2.11 Voltage-clamp quality and voltage-dependence of calcium currents in differentiated N1E-115 cells 77

2.12 Inactivation of T-type and activation of L-type calcium currents 79

Chapter 3

3.1 The fraction of cells without neurites as a function of time in the differentiation medium 86

3.2 Peak T- and L-type calcium current density as a function of total neurite length 89

Chapter 4

4.1 Fura-2 ratio imaging of a quiescent growth cone 97
4.2 Fura-2 ratio imaging of a motile advancing growth cone 99
4.3 Fura-2 ratio imaging of a motile non-advancing growth cone 102
4.4 Fura-2 ratio imaging of a flattening growth cone 105
4.5 Fura-2 ratio imaging of a retracting growth cone 107
4.6 Recovery of motility coincides with a fall of $[Ca^{2+}]_i$................. 110
4.7 $[Ca^{2+}]_i$ in a growth cone differentiating in the absence of DMSO 114
4.8 Apparent spatial gradients of $[Ca^{2+}]_i$ in cells loaded by incubation in fura-2 AM 117
4.9 Mean ratio values with corresponding $[Ca^{2+}]_i$ for the five growth cone behavioural states 119

Chapter 5

5.1 Calcium hotspots at the neuronal growth cone 127
5.2 Selective Cd^{2+} block of L-type current and calcium hotspot...... 131
5.3 Calcium hotspots observed under physiological conditions 134

List of Tables

Chapter 2

2.1 Calcium buffers for calibration of DIFM 58

2.2 Patch pipette solutions 75

2.3 External media 76

Acknowledgements

It is a pleasure to thank Stephen Bolsover for his guidance, advice, criticism and encouragement throughout the period of this work. I would also like to thank Angela Lamb and everyone in David Attwell and Peter Mobbs's group for making my time here stimulating and enjoyable.

In addition, I would like to thank the following for helpful discussion on various aspects of this work: David Allen, Michael Dickens, Michael Duchen, Ann Silver and Michael Whitaker.

I am very grateful to both the Medical Research Council of Great Britain for the award of a postgraduate research studentship and the Department of Physiology, for six months' extension. Finally, I would like to thank Henrietta for her love, encouragement and tolerance.

Publications

Bolsover, S.R., Lamb, A.G. and Silver, R.A. (1988). Measurement of $[Ca^{2+}]_i$ in neuronal growth cones of N1E-115 neuroblastoma cells of the mouse. Journal of Physiology, 407, 87P.

Silver, R.A., Lamb, A.G. and Bolsover, S.R. (1989). Elevated cytosolic calcium in the growth cone inhibits neurite elongation in neuroblastoma cells: Correlation of behavioural states with cytosolic calcium concentration. Journal of Neuroscience 9, 4007-4020.

Bolsover, S.R., Lamb, A.G. and Silver, R.A. (1989). A Digital Imaging Fluorescence Microscope to measure spatial gradients of calcium within growing growth cones of mouse neuroblastoma cells. Journal of Physiology 415, 8P.

Allen, D.G., Bolsover, S.R., Lamb, A., Lee, J.A., Silver, R.A. and Westerblad, H. (1989). Gradients of intracellular calcium during fatigue in isolated single muscle fibres from *Xenopus laevis*. Journal of Physiology 415, 120P.

Silver, R.A., Lamb, A.G. and Bolsover, S.R. (1990) Calcium hotspots caused by L-channel clustering promote morphological changes in neuronal growth cones. Nature 343, 751-754.

Abbreviations

ABP = actin binding protein
ANTS = 8-aminonaphthalene-1,3,6-trisulphonic acid
AM = acetoxymethyl ester
ATP = adenosine triphosphate
BAPTA = 2-bis(2-aminophenoxy)ethane N,N,N',N'-tetraacetic acid
$[Ca^{2+}]_i$ = cytosolic free calcium concentration
cAMP = adenosine 3',5'-cyclic monophosphate
cGMP = guanosine 3',5'-cyclic monophosphate
CCD = Charge coupled device
CNS = central nervous system
dBcAMP = dibutyryladenosine 3',5'-cyclic monophosphate
DAG = diacylglycerol
DIFM = digital imaging fluorescence microscope
DMEM = Dulbeccos's modification of Eagles medium
DMSO = dimethyl sulphoxide
DRG = dorsal root ganglion
EGTA = ethylene glycol-bis(β-aminoethyl ether) N,N,N',N'-tetraacetic acid
GAP-43 = growth associated protein 43
HEPES = N-[2-hydroxyethyl]piperazine-N'-[2-ethanesulfonic acid]
IP_3 = inositol 1,4,5-trisphosphate
MAP-2 = microtubule associated protein 2
NA = numerical aperture
N-CAM = neuronal cell adhesion molecule
NGF = nerve growth factor
NMDA = N-methyl-D-aspartate

PIP$_2$ = phosphatidylinositol 4,5-bisphosphate

PSF = point spread function

SIT = silicon-intensified target

TEA = tetraethylammonium

TTX = tetrodotoxin

Chapter 1

Introduction

1.1 What is a neuronal growth cone?

Neurons are unique in that they can extend processes over large distances; these cylindrical, often branched, processes are called neurites. Neurites can be subdivided into two classes: a single axon which is usually the longest process, and many dendrites. Neuronal growth cones are the structures at the ends of extending axons and dendrites. The terminal structures of nerve processes were first described by Ramon y Cajal a century ago; he called them growth cones because they had a conical geometry (Ramon y Cajal, 1890). The term growth cone has been universally accepted even though subsequent studies have described a wide variety of growth cone shapes (Bray, 1982; Bastiani *et al.*, 1985; Bentley and Toroian-Raymond, 1986). Cajal proposed that amoeboid movement of the growth cone led the advance of extending neurites and had a central role in the connection of neural networks. Growth cone locomotion was confirmed by Harrison (1907, 1910) who, using a novel tissue culture technique watched living growth cones. In fact, because of the inaccessibility of growth cones *in vivo*, most of our present understanding is based on studies *in vitro*.

The ultrastructure of growth cones has been extensively studied with both electron and light microscopy (Yamada *et al.*, 1971; Bray and Bunge, 1973; Tosney and Wessells, 1983; Goldberg and Burmeister, 1986; Forscher and Smith, 1988). These investigations have demonstrated the presence of organelles similar to those seen in other parts of the cell, but the spatial distribution of organelles and, more strikingly, the cytoskeleton is unique to the growth cone. Microtubules which are arranged in longitudinal bundles constrain the neurite to a cylindrical shape (Matus, 1988). They terminate in the proximal region of the growth cone

(Forscher *et al.*, 1987). Within the palm of the growth cone there is a dense network of actin filaments (microfilaments). Often, bundles of microfilaments radiate from the central region and form long thin finger-like extensions called filopodia (Letourneau, 1983). Growth cones exhibit a complex and rapidly changing morphology, extending and then retracting filopodia (Argiro *et al.*, 1985) or flat featureless membrane veils (Tosney and Wessells, 1983) over the substrate. The surface of the growth cone bears complex motile ruffles (Connolly *et al.*, 1985). The movement of filopodia, veils and ruffles on the growth cone is termed motility. Motile activity seems to have two roles; first it may act as a motor for forward growth and second it aids exploration of the immediate environment around the growth cone.

Growth at the growth cone consists of advance at two locations. The leading edge of the growth cone is pulled forward by the tension in filopodia (Bray, 1987) or moves forward by extending veils (Goldberg and Burmeister, 1986). The boundary between the neurite and the growth cone moves forward by an extension of the microtubule/neurofilament cytoskeleton (Goldberg and Burmeister, 1986), probably by addition of monomers at the neurite/growth cone boundary (Bamburg *et al.*, 1986). During this process it is likely that membrane is added at the growth cone (Bray, 1970; Landis, 1983).

1.2 Why are growth cones interesting?

The mammalian central nervous system (CNS) is made up of approximately 10^{10} neurons, each of which has up to 200,000 connections (Kuffler *et al.*, 1984). Neuronal growth cones play a central role in the formation of brain circuitry during development. They utilize both intrinsic and extrinsic cues to navigate through tissue to find their correct target cell. Filopodia extend from the growth cone and probe the surroundings to find information necessary for navigation (Bentley and Toroian-Raymond, 1986). Once the target cell is reached the growth cone or part of it is transformed into synaptic connections.

The growth cone is sensitive to many extrinsic stimuli. Extracellular matrix molecules such as fibronectin and laminin, cell surface adhesion molecules, growth factors that are secreted by some target tissues, and neurotransmitters all modulate the direction or extent of neurite outgrowth (Dodd and Jessell, 1988; Lipton and Kater, 1989). The mechanisms of signal transduction which result in directed outgrowth have not been elucidated but there is growing evidence that three pathways familiar from other systems, involving respectively the intracellular messengers, cytosolic free calcium concentration ($[Ca^{2+}]_i$), cyclic nucleotides and inositol phosphates are involved. I will briefly discuss the evidence for involvement of the cyclic nucleotides and the inositol phosphates in neurite outgrowth before going on to the main topic of $[Ca^{2+}]_i$.

Nerve growth factor (NGF) stimulates the formation of neurites in sympathetic neurons (Levi-Montalcini *et al.*, 1954) and PC12 cells (Schubert *et al.*, 1978). Application of NGF elevates adenosine 3',5'-cyclic monophosphate (cAMP) and addition of the non-hydrolysable cAMP analog, dibutyryladenosine 3',5'-cyclic monophosphate (dBcAMP) to the medium, stimulates neurite outgrowth and increases cell substrate adhesion (Schubet *et al.*, 1978). Incubation in culture medium containing dBcAMP also induces differentiation in neuroblastoma cells (Chalazonitis and Greene, 1974), and Gundersen and Barrett (1980) showed that individual chick dorsal root ganglion (DRG) growth cones grow towards sources of dBcAMP and guanosine 3',5'-cyclic mono phosphate (cGMP). However, the opposite effect is seen in *Helisoma* where application of forskolin, which raises [cAMP], inhibits growth cone motility and neurite outgrowth (Mattson *et al.*, 1988a). S. Bolsover and I. Spector (personal communication) injected a number of putative second messengers into neuroblastoma cells and found that the cyclic nucleotides cAMP and cGMP had opposite effects: cAMP promoted motility, but cGMP froze motile structures. Inositol 1,4,5-trisphosphate (IP_3) caused retraction of motile structures on the growth cone possibly by releasing Ca^{2+} from intracellular stores. Another role for inositol phosphates in modulating growth cone function is suggested by the finding that phosphatidylinositol 4,5-bisphosphate (PIP_2) can control the activity of actin binding, severing and nucleation proteins (Forscher, 1989). The evidence suggests that each of the second messenger systems produces an effect but, at this stage, it impossible to determine their relative importance.

1.3 Calcium regulation in the growth cone

The cytoplasmic calcium concentration of neurons at rest is 10^{-7} M as compared with 10^{-3} M in the extracellular fluid. $[Ca^{2+}]_i$ can be increased either by influx of Ca^{2+} through the plasma membrane or by release from intracellular stores. Calcium crosses the plasma membrane by passive movement through voltage-gated calcium channels, ligand-gated calcium channels (for example the NMDA receptor-activated channel) or by reversal of the electrogenic Na^+/Ca^{2+} exchanger. Experimental or transmitter-mediated depolarization of the membrane will therefore cause Ca^{2+} influx. Of these three components, the influx through voltage-gated channels seems to be the most important.

Three types of voltage-gated calcium channel have been identified in vertebrate neurons (Nowycky *et al.*, 1985). The T-type channel has a small unit conductance (8 pS in Ba^{2+}), is activated above -70 mV, is fully inactivated at a holding potential of -40 mV and inactivates with a time constant of 20-50 ms (at 0 mV in 10 mM extracellular Ca^{2+} at 20 °C). The N-type channel has a unit conductance of approximately 13 pS in Ba^{2+}, is activated above -20 mV and inactivates with a moderately fast time course of 50-80 ms (0 mV, 10mM Ca^{2+} at 20 °C). The L-type channel has a large unit conductance (25 pS in Ba^{2+}), is activated above -20 mV and inactivates very slowly with a time constant of >500 ms (Tsien *et al.*, 1988). Several studies have demonstrated that depolarization causes calcium influx at the neuronal growth cone (Anglister *et al.*, 1982; Bolsover and Spector, 1986; Cohan *et al.*, 1987) and in 1988 Lipscombe *et al.* demonstrated unequivocally the presence of voltage-gated calcium channels at the growth cone.

The spatial distribution of Ca^{2+} channels is likely to be very important to the localization and magnitude of voltage-induced changes in $[Ca^{2+}]_i$ and therefore to functional specialization (Miller, 1987). Gross $[Ca^{2+}]_i$ gradients have been observed during depolarization, with larger $[Ca^{2+}]_i$ increases in terminal dendrites and growth cones than in proximal dendrites (Tank *et al.*, 1988; Regehr *et al.*, 1989). These results have been interpreted as showing an inhomogeneous calcium channel distribution, although the influence of inhomogeneous calcium buffering and surface area have not been determined. On a smaller scale, patch clamp (Fox *et al.*, 1987; Lipscombe *et al.*, 1988; Thompson and Coombs, 1988), toxin binding (Jones *et al.*, 1989) and freeze fracture studies (Pumplin *et al.*, 1981) have shown that calcium channels are sometimes grouped into clusters. However, so far there is no evidence that calcium channel clusters produce $[Ca^{2+}]_i$ gradients or that they have any physiological role.

Intracellular stores including endoplasmic reticulum (ER) and mitochondria can also release Ca^{2+} into the cytoplasm. The two intracellular messengers that are known to cause release from intracellular stores under physiological conditions are IP_3 and Ca^{2+} itself. IP_3, a soluble cytosolic molecule, acts by carrying a signal from the plasma membrane to intracellular calcium stores. Binding of agonist to cell surface receptors activates phospholipase C, which splits phosphatidylinositol 4,5-bisphosphate into diacylglycerol (DAG) and IP_3. IP_3 then binds to the endoplasmic reticulum (Berridge and Irvine, 1984). IP_3 receptors, which have been purified from neuronal tissue (Suppattapone *et al.*, 1988), cause release of Ca^{2+} from the endoplasmic reticulum by opening a 10 pS calcium channel (Berridge and Irvine, 1989). A common property of systems expressing IP_3 receptors is a tendency for Ca^{2+} release to be 'all or nothing', so that addition of agonist produces one or more 'Ca^{2+} spikes' in which $[Ca^{2+}]_i$ rises transiently to a high level. Variation of agonist concentration alters the fraction of cells showing Ca^{2+} spikes, the latency of the response and the frequency of Ca^{2+} spikes, but not the $[Ca^{2+}]_i$ at the peak of each spike (Jacob *et al.*, 1988). The second release mechanism from intracellular stores is Ca^{2+}-induced Ca^{2+} release. This allows relatively small Ca^{2+} signals resulting from entry of Ca^{2+} across the plasma membrane to be greatly amplified by Ca^{2+} release from intracellular stores. A Ca^{2+}-release channel that binds ryanodine is thought to be important in calcium-induced calcium release (Lai *et al.*, 1988). O'Sullivan *et al.*, (1989) have shown that application of the agonists nicotine and muscarine to adrenal chromaffin cells produce different spatial distributions of $[Ca^{2+}]_i$. They propose that this effect is due to activation of two different calcium pathways: nicotine, by depolarizing, activates calcium influx across the membrane, and muscarine stimulates the production of IP_3 which induces release from intracellular stores. The different spatial distributions of $[Ca^{2+}]_i$ produced by these two agonists differ greatly in their potency because only Ca^{2+} influx across the membrane raises $[Ca^{2+}]_i$ in the region close to the membrane to levels high enough to trigger exocytosis (Cheek *et al.*, 1989). It is possible that this type of spatial coding of increases in $[Ca^{2+}]_i$ may be important in the regulation of the growth cone.

Cytoplasmic Ca^{2+} is buffered by calcium binding proteins such as parvalbumen. These chemical buffers drastically reduce the instantaneous change in $[Ca^{2+}]_i$ for a given influx and reduce the ability of Ca^{2+} to diffuse from the influx site. Calcium is removed from the cytoplasm by sequestration into intracellular stores and by transport across the plasma membrane. Intracellular compartments thought to be important in calcium uptake include endoplasmic reticulum, mitochondria, calciosomes and synaptic vesicles. The uptake system of the ER has a higher affinity than that in mitochondria and will therefore be effective at lower concentrations. Long-term calcium regulation requires that plasma membrane calcium influx and efflux is equal. Efflux across the plasma membrane occurs via Ca-ATPase and Na^+/Ca^{2+} exchange mechanisms. The plasma membrane Ca^{2+}-ATPase is a high affinity (K_d = 0.2-0.3 μM) low-transport capacity system, whereas the bidirectional Na^+/Ca^{2+} exchange has a lower affinity for Ca^{2+} (K_d = 0.5-1 μM) but a higher transport capacity (Blaustein, 1988). Very little is known about the relative Ca^{2+}-buffering power of the plasma membrane, internal stores and chemical buffers in the growth cone. However, since the surface area to volume ratio is high in the growth cone it is likely that the plasma membrane component is very important.

1.4 The role of $[Ca^{2+}]_i$ in neurite outgrowth and growth cone motility: a historical review

Schubert *et al.* (1978) demonstrated in their paper on NGF that elevation of $[Ca^{2+}]_i$ by application of the calcium ionophore A23187 increased cell-substrate adhesion in a dose dependent manner. Stimulation of Ca^{2+} influx by potassium-induced depolarization promoted both adhesion, which was blocked by Co^{2+}, and neurite outgrowth. These results indicated a causal link between $[Ca^{2+}]_i$ and neurite outgrowth in NGF-dependent PC12 cells. Baccaglini (1978) showed that Ca^{2+} channels were expressed early in the development of primary frog spinal neurons, suggesting that voltage-gated calcium influx was also important in differentiation of nerve cells *in vivo*. This view was strengthened by the observation that chick DRG growth cones, when placed in a medium containing the calcium ionophore A23187, turn towards a pipette containing 20 mM $CaCl_2$

(Gundersen and Barrett, 1980). The authors suggested that turning could be produced by intracellular gradients of Ca^{2+} which act by altering the distribution of adhesion sites on the growth cone.

Using the loose patch technique Anglister *et al.* (1982) showed that voltage-activated Ca^{2+} channels are less abundant in the neurite than in the growth cone of N1E-115 neuroblastoma cells. They induced morphological changes at the growth cone by promoting calcium entry. Growth cones flattened onto the substrate and their area increased dramatically when the cells were electrically stimulated, depolarized with potassium or exposed to the calcium ionophore A23187. Micro-application of K^+ or Ca^{2+} showed that Ca^{2+} influx occurred at the growth cone. Substrate adhesion was measured using interference reflection microscopy and was found not to change during flattening. This result suggests that, rather than causing an increase in adhesion, $[Ca^{2+}]_i$ is acting at the level of the cytoskeleton, possibly by depolymerization of the actin filament network. Anglister *et al.* (1982) noted that membrane veil formation was extensive during the flattening process. Since observation of untreated growth cones with electron microscopy showed no evidence of membrane folds, they concluded that veil formation must occur by addition of new membrane, possibly by calcium-induced vesicle fusion. Finally they proposed that elevated $[Ca^{2+}]_i$ might cause neurite elongation, but it is unclear whether they meant elongation of the process caused by advance of the growth cone margin during flattening or elongation of the neurite proper.

Evidence against this convincing and simple 'calcium hypothesis' of neuronal outgrowth was provided early on by two studies. Kostenko *et al.* (1983) concluded from experiments using A23187, serotonin and low-Na^+ solutions that all treatments that promoted the increase of $[Ca^{2+}]_i$ inhibited neurite formation and caused retraction of neurites that had already been formed. Blixby and Spitzer

(1984) demonstrated that, rather than inhibiting neurite outgrowth, block of Na^+ and Ca^{2+} influx by medium containing tetrodotoxin (TTX) and Mg^{2+}-EGTA promoted neurite outgrowth in *Xenopus* embryonic spinal neurons. The stimulation of neurite elongation by removal of extracellular calcium, in cells shown to have a long-duration Ca^{2+} action potential, was difficult to reconcile with previous ideas.

Evidence for the presence of a steady Ca^{2+} influx during growth cone motility was provided by Freeman *et al.* (1985). This group developed a sensitive vibrating probe to measure extracellular current density. Using this technique they discovered that electrical currents flow into the tip of filopodia during active outgrowth of goldfish neurons. Ion substitution showed that the majority of the current was carried by Ca^{2+} ions which, they suggested, flowed through voltage-gated calcium channels. They proposed that these steady calcium currents may cause localized exocytosis and autofocusing of receptor molecules by electrophoresis. Electrical activity has a variety of inhibitory effects on *Helisoma* growth cones *in vitro*. Electrical stimulation at the cell body resulted in reversible suppression of neurite elongation, a reduction of growth cone size and a decrease in the number of filopodia (Cohan and Kater, 1986). In the mid 1980s the body of contradictory evidence concerning the calcium hypothesis of neurite outgrowth was very confusing because no direct measurement of $[Ca^{2+}]_i$ was possible and the existing data could be used to argue for or against it. The first direct measurements of growth cone $[Ca^{2+}]_i$ changes were made using the metallochromic dye Arsenazo III by Bolsover and Spector (1986) who showed that voltage-gated changes in $[Ca^{2+}]_i$ were greater in the growth cone and soma than in the neurite. This result agreed with the findings of Anglister *et al.* (1982) and with what was known about the sensitivity of microtubules to calcium-induced depolymerization (Schliwa, 1976; Kiehart, 1981; Keith *et al.*, 1983).

Connor (1986) used the calcium indicator fura-2 and a digital imaging fluorescence microscope (DIFM) to measure the spatial distribution of $[Ca^{2+}]_i$ within growing embryonic rat neurons. His results showed a correlation between neurite outgrowth and elevated levels of measured $[Ca^{2+}]_i$. In cells that were not differentiated or that had processes but were not actively growing, $[Ca^{2+}]_i$ was low (30-70 nM). In neurons that were extending processes, $[Ca^{2+}]_i$ was high (200-1000 nM). Connor also demonstrated a high correlation between filopodial outgrowth and localized areas of high $[Ca^{2+}]_i$ within the growth cone, as would be predicted by the finding of Freeman *et al.* (1985). However he could not rule out the possibility of artifacts caused by loading intracellular compartments, other than the cytoplasm, with fura-2.

Cohan, Connor and Kater (1987) used fura-2 to measure $[Ca^{2+}]_i$ in *Helisoma* neurons under a number of different conditions. They confirmed Connor's (1986) result that $[Ca^{2+}]_i$ was higher in motile as compared with non motile growth cones. Stimulation of action potentials, which was known to inhibit motility, caused substantial calcium influx in the growth cone. The changes in $[Ca^{2+}]_i$ were much higher in the growth cone than in the neurite, in agreement with previous reports. Hyperpolarization caused a reduction in the growth cone $[Ca^{2+}]_i$ consistent with a steady calcium influx through voltage-gated channels. Application of the neurotransmitter serotonin was found to raise $[Ca^{2+}]_i$ only in those cells (*Helisoma* B19) in which it inhibited motility. This suggested that neurotransmitter actions on growth cone motility acted via $[Ca^{2+}]_i$. From this and previous data Cohan *et al.* (1987) suggested a model for the role of calcium in neuronal outgrowth. In this model, growth cone motility and neurite elongation occurs over a small range of $[Ca^{2+}]_i$ between 100 and 300 nM, if $[Ca^{2+}]_i$ falls below or rises above this range growth cone stabilization occurs. The sensitivity of neurite elongation, filopodia and membrane veils to inhibition by raised $[Ca^{2+}]_i$ was demonstrated by applying increasing concentrations of the calcium ionophore A23187 (Mattson and Kater, 1987). These authors found that high concentrations of inorganic calcium channel blockers also suppressed neurite elongation and growth cone motility. This implied that both an increase and a total block of Ca^{2+} influx into the growth cone could stop motility and neurite elongation. However organic calcium channel blockers and danrolene, which blocks Ca^{2+}-induced Ca^{2+} release, had little effect. This raises the possibility that high concentrations of La^{3+}, Co^{2+} and Cd^{2+} did not act by causing a reduction of $[Ca^{2+}]_i$, but had a toxic effect, but this possibility was not considered. At lower concentrations of these blockers, filopodia were significantly reduced but neurite elongation was enhanced. A similar result was obtained by lowering the extracellular calcium concentration. Finally Mattson and Kater found that serotonin sensitivity of *Helisoma* B19 neurons was dependent on Ca^{2+} influx. In a later paper Mattson *et al.* (1988a) showed that inhibition of *Helisoma* B19 and B5 growth cone motility and neurite elongation produced by an increase of cAMP was caused by an increased calcium influx and could be blocked by La^{3+} or low extracellular calcium. However, this mechanism was not general even within a small population since motility of other neurons from the same ganglia was inhibited by cAMP independently of Ca^{2+}.

Kater's group proposed a more detailed version of the model for calcium regulation at the growth cone (Kater *et al.*, 1988). According to this influential model neurite elongation and growth cone motility are both sensitive to $[Ca^{2+}]_i$ but the two processes have a different optimal $[Ca^{2+}]_i$. Neurite elongation has a lower Ca^{2+} optimum than growth cone motility. If $[Ca^{2+}]_i$ rises above or falls below the range of $[Ca^{2+}]_i$ permitting growth both motility and elongation are inhibited and the neurite stabilizes. By assuming that the resting level of $[Ca^{2+}]_i$ in neurons can be above or below the 'growth range' they were able to explain much of the previously conflicting evidence.

A combined approach using a DIFM and cell-attached patch clamping was used by Lipscombe *et al.* (1988) to investigate calcium regulation in different regions of frog neurons. They showed unequivocally that N- and L-type calcium channels are present in the soma, neurite, and growth cone membrane and that they are often located in clusters, sometimes dominated by one channel type. Imaging of the cell $[Ca^{2+}]_i$ showed that concentration changes caused by Ca^{2+}-release from caffeine-sensitive intracellular stores were much larger in the soma than in the growth cone. This implies that calcium stores are not important in stimulus-induced increases in $[Ca^{2+}]_i$ at the growth cone.

Hippocampal pyramidal neurons grown in culture have a morphology similar to that *in vivo* (Banker and Cowan, 1979). When the cultures are grown at low density, axons and dendrites can easily be identified by their morphology. The accuracy of this method of identification was checked using fluorescent antibodies to growth associated protein (GAP-43), which is axon specific and microtubule associated protein (MAP-2), which is dendrite specific. Mattson *et al.* (1988b) used this preparation and found that axonal growth was unaffected by the presence of glutamate while dendritic growth was severely inhibited. This inhibition was mediated by Ca^{2+} influx via voltage-gated calcium channels and they attributed the different sensitivity of axons and dendrites to the presence of the glutamate receptor on the dendritic tree but not on the axon.

Goldberg (1988) has used electronically enhanced interference microscopy to study the role of $[Ca^{2+}]_i$ in *Aplysia* growth cone motility. Reduction of extracellular calcium or application of 20 mM Co^{2+} caused a reduction in area of immature membrane veils. Veil formation in low extracellular calcium could be induced by application of 5 μM A23187 ruling out extracellular Ca^{2+}-dependent adhesion as a possible explanation. Furthermore, he demonstrated that focal application of 22 mM Ca^{2+} caused localized veil formation when growth cones were perfused with a low-calcium medium (0.5 mM). Veil maturation, called engorgement in the model of growth cone growth proposed by Goldberg and Burmeister (1989), continued in low calcium while the formation of new veil was inhibited.

To sum up, a model for $[Ca^{2+}]_i$ regulation of growth cone motility and neurite elongation has been proposed by Kater *et al.* (1988). The current view of calcium regulation at the growth cone is based on their model. There seem to be two locations at which $[Ca^{2+}]_i$ acts: at the neurite where calcium affects microtubule/neurofilament polymerization, and at the growth cone where calcium affects motility. These two locations have different $[Ca^{2+}]_i$ sensitivities. Neurite elongation is maximal at relatively low $[Ca^{2+}]_i$ and is therefore promoted by reducing calcium influx (assuming a resting level above this optimum). Growth cone motility such as filopodia and lamelipodia formation and movement has a higher optimum for $[Ca^{2+}]_i$, is inhibited by channel blockers and is promoted by the application of high extracellular calcium or ionophore (assuming a resting level below this optimum). The range of $[Ca^{2+}]_i$ over which neurite growth and growth cone motility occurs, is small. If $[Ca^{2+}]_i$ falls below or rises above this range growth and motility stop and the growth cone stabilizes or retracts.

1.5 The significance of this study

This section briefly summarizes the most important new findings of the work presented here. The N1E-115 mouse neurobastoma cell line was used for this study because the cells have large growth cones in which $[Ca^{2+}]_i$ can be easily imaged. Two aspects of growth cone $[Ca^{2+}]_i$ were investigated: steady state $[Ca^{2+}]_i$ in growth cones growing in isolation with no external stimuli, and secondly, transient changes of $[Ca^{2+}]_i$ which were caused by electrical stimulation.

In Chapter 2 I describe a method for determining the absolute resolution of calcium gradients measured in thin biological specimens using a digital imaging fluorescence microscope. This spatial limitation has not been considered in previous imaging studies. Data presented in Chapter 3 demonstrate that T-type channels are always expressed before the cell forms neurites. This is consistent with calcium channel expression during development of chick motoneurons (McCobb *et al.*, 1989). Once expressed, the characteristics of the L- and T-type currents do not change during diffentiation.

In Chapter 4 I describe data correlating $[Ca^{2+}]_i$ and growth cone behaviour. Most of the results are consistent with the model proposed by Kater *et al.* (1988) but some of the findings cannot be explained with this model. The most important 'inconsistent' finding is that true growth, that is elongation of the cylindrical neurite and advance of the growth cone, occurred only at basal $[Ca^{2+}]_i$, the same $[Ca^{2+}]_i$ that is found in quiescent or stabilized growth cones. Any elevation above this basal level was associated with an inhibition of neurite elongation. Growth cone motility was observed at basal $[Ca^{2+}]_i$ but was less sensitive than neurite elongation to raised $[Ca^{2+}]_i$. Veil formation during flattening behaviour previously reported by Anglister *et al.* (1982) was associated with raised $[Ca^{2+}]_i$. I was also able to show that loading of fura-2 using the acetoxymethylester (AM) of fura-2 can produce artifactual $[Ca^{2+}]_i$ gradients around the cell body and at the tip of growth cones. Since Connor (1986) used a similar protocol it is likely that his report of a correlation between filopodial extension and localized elevated $[Ca^{2+}]_i$ was an artifact of the dye loading procedure.

In Chapter 5 data are presented that demonstrate the presence of T- and L-type calcium channels at the growth cone and show that the two calcium channel types have different spatial distributions. The L-type channel is clustered in one to five discrete locations in the growth cone membrane whereas the T-type channel is uniformly distributed. Activation of L-type channel clusters by action potentials produces $[Ca^{2+}]_i$ hotspots which rise on average by 89 nM per action potential, that is in twelve action potentials hotspot $[Ca^{2+}]_i$ will reach micromolar levels. This highly localized increase in $[Ca^{2+}]_i$ causes morphological changes such as veil formation at the site of the hotspot.

The results from this study provide evidence that voltage-gated calcium influx is an important modulator of growth cone behaviour but that low $[Ca^{2+}]_i$ is essential for neurite elongation to occur.

Chapter 2

Methods

2.1 The digital imaging fluorescence microscope

The digital imaging fluorescence microscope consisted of an ultraviolet (UV) light source, an inverted microscope, a low light level video camera and a computer controlled image processor (Fig. 2.1). Ultraviolet light from a 150 W xenon arc lamp (Osram, W. Germany) encased in an Ealing Stabilarc 250 housing was passed through a Schott KG1 heat filter, a UV-pass filter (Ealing 0X1) and one of a set of two alternating narrow-band filters. The 350 nm and 380 nm narrow band filters (DF series, Glen Spectra) were rotated in and out of the UV beam by a stepper motor controlled by an Apple computer. The lamp and lamp-housing mirror were adjusted to give Köhler illumination. Filtered light then entered a Zeiss IM microscope, was reflected by a dichroic mirror (400 nm longpass, Glen Spectra), and focused onto the specimen through a 100x glycerol immersion Nikon Neofluor UV-F objective of numerical aperture (NA) 1.3. The system is epifluorescent and therefore there is only one lens for focusing excited light on the specimen and collecting longer wavelength (500 nm) emitted light from the fluorescing specimen. Thus light passed through the objective twice giving a fourth power dependence on numerical aperture. The light then passed through the dichroic mirror and a broad-band filter of centre wavelength 510 nm (DF510/30, Glen Spectra) before it was directed either to the eyepieces or a silicon-intensified target (SIT) video camera (type 5153-7000, COHU, USA).

The video signal was digitized, averaged and stored as an array of 512 x 512 bytes by a Gould FD 5000 image processor. Each byte or pixel contained 8 bits giving a 256 level grey scale. Image manipulation such as subtraction and division was done by the image processor but controlled by a suite of programs

Figure 2.1 Schematic diagram of the digital imaging fluorescence microscope

Solid lines indicate the UV light beam and arrows indicate direction of command and measurement signals.

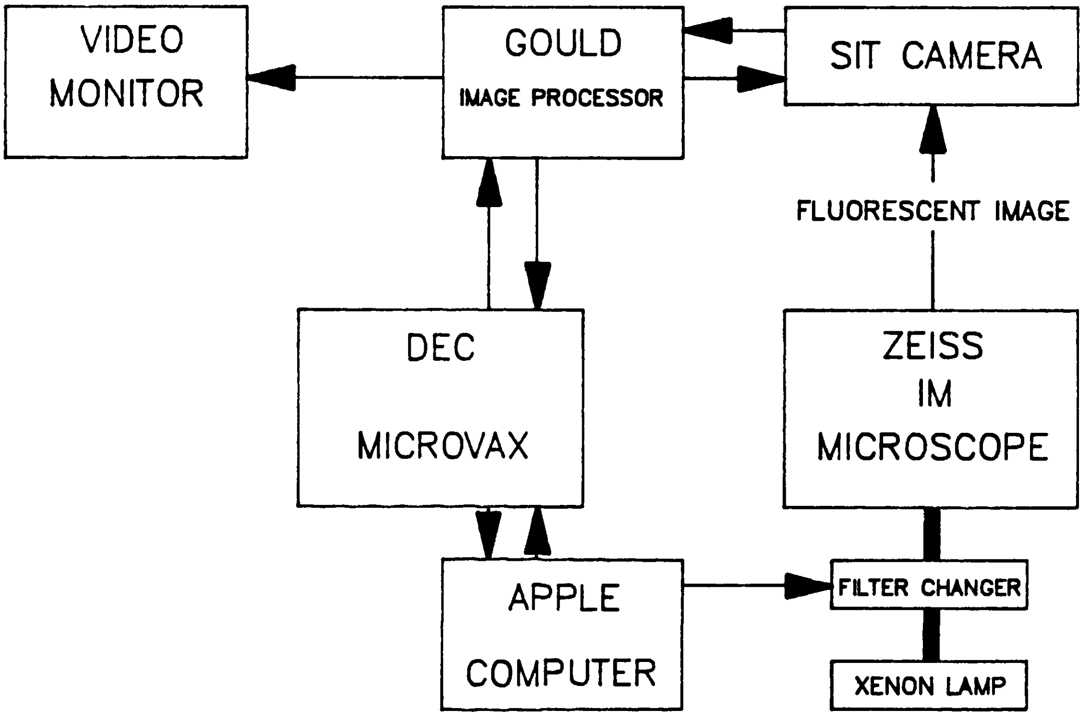
VIDEO MONITOR
GOULD IMAGE PROCESSOR
SIT CAMERA
FLUORESCENT IMAGE
DEC MICROVAX
ZEISS IM MICROSCOPE
APPLE COMPUTER
FILTER CHANGER
XENON LAMP

written by Angela G. Lamb and run on a DEC Microvax computer. Data were stored during the experiment on a 60 Mb hard disc and were then transferred to tape (90 Mb) for long-term storage.

2.1.1 Calibration of the camera linearity and image processor acquisition rate

For the system to provide quantitative and not just qualitative fluorescence data, the camera linearity and the gain had to be characterized. The input-output relationship of the camera was determined in its most linear mode (gamma correction = 1). The light incident on the camera was varied using neutral density filters and the amplitude of the video signal was averaged over 32 frames. Figure 2.2a shows the relationship between output signal intensity and incident light intensity. Figure 2.2b shows a plot of averaged signal amplitude against the voltage across the camera tube (gain). These results demonstrate that the camera output was linear with respect to both light input and high voltage gain.

Imaging at high temporal resolution required characterization of the camera dynamics and video acquisition timing. A step change in incident light intensity was produced using a NeuroLog pulse generator (Digitimer Ltd., Welwyn) connected to an light emitting diode. The analog video signal responded to a step change of light with a time constant of 150 ms, thus fast changes in fluorescence were filtered to this level. A second, absolute limit to the temporal resolution was set by the Gould image processor. When instructed to acquire images at the maximum rate and store them in its memory, the image processor stored one frame every 60 ms.

Figure 2.2 Characterization of the SIT camera input-output relation and gain

Part a shows the relationship between the video signal output and the incident light intensity input for a COHU 5000 silicon-intensified target camera with the gamma correction adjustment set to 1. Light intensity was varied from the saturating level by inserting calibrated neutral density filters into the beam. The video signal frames were digitized into an array of 512 x 512 pixels and 32 frames were averaged, the intensity of the field of view was measured by averaging all the pixels. The input-output relationship was highly linear and the straight line fit was by eye.

Part b shows the relationship between the video signal output and the voltage across the camera tube (camera gain with an arbitrary scale between 0 and 10, the background level was set to threshold during zero incident light) for a 9 μm diameter drop of 100 μM fura-2 illuminated with 350 nm light. The relationship is linear and the line was fitted by eye. The line intersects the X axis at -0.25 giving a real range of 0.25 to 10.25 for the camera gain.

a,

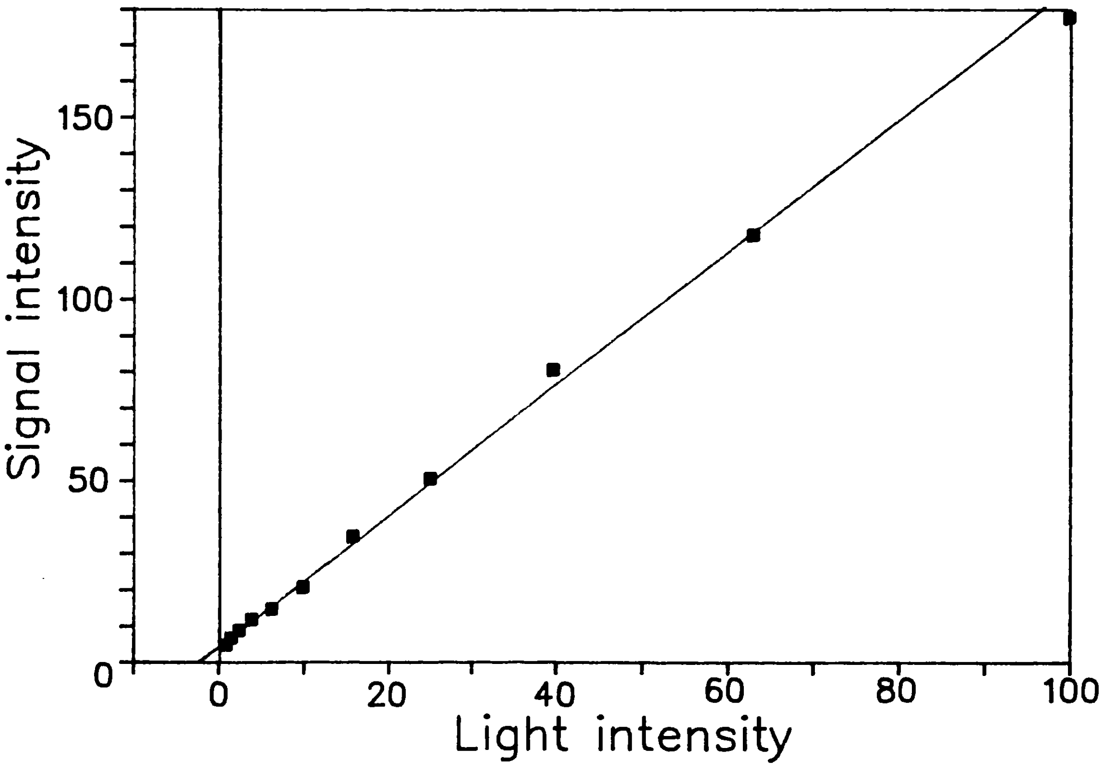
Signal intensity
150
100
50
0
0
20
40
60
80
100
Light intensity

b,

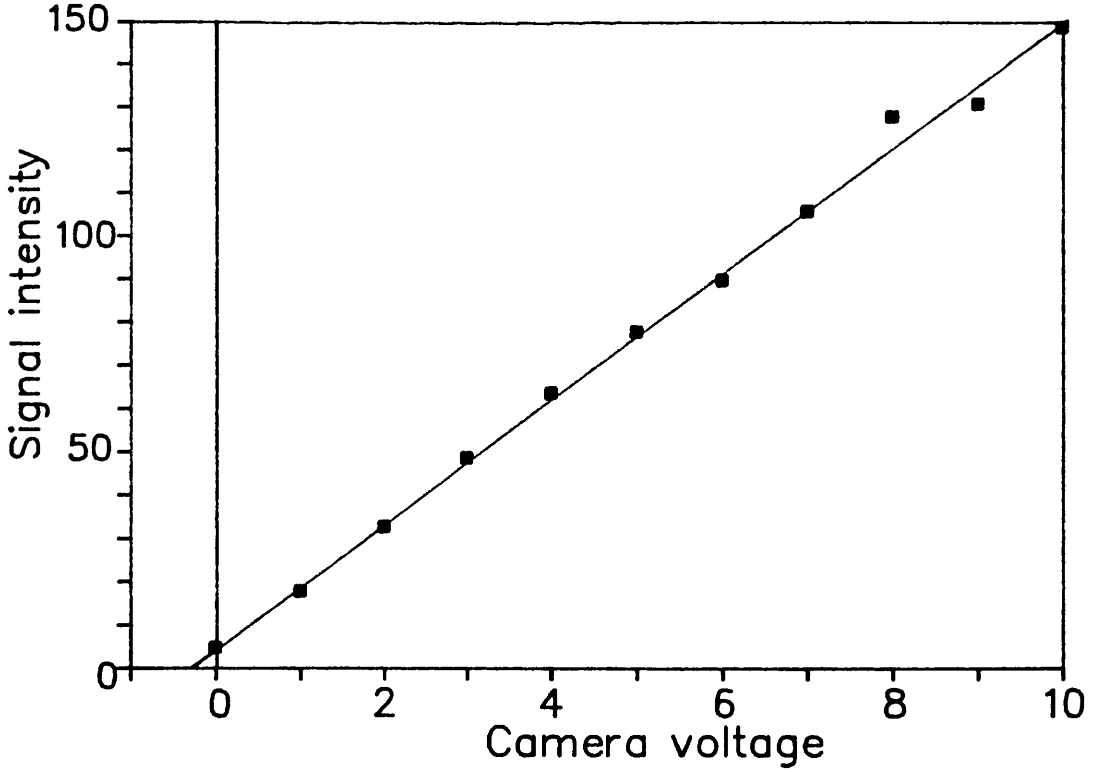
Signal intensity
150
100
50
0
0
2
4
6
8
10
Camera voltage

2.2 Spatial resolution of the digital imaging fluorescence microscope

2.2.1 Calculation of the resolution for point fluorescent images

The theoretical limit of resolution for two fluorescent point sources can be calculated from the numerical aperture of the objective and the wavelength of light used. The two points are said to be resolved when the central maximum of one Airy pattern falls over the first minimum of the other. This occurs at $D = 0.61\lambda/(n \sin \alpha)$ where λ is wavelength, n is refractive index and α is the half-angle of the emergent cone of rays. Substituting NA for $(n \sin \alpha)$ gave a resolution limit of 0.23 µm using the 1.3 NA objective and the fluorescent indicator fura-2 which emits around 500 nm. This limit of resolution can be approached only when there is no out-of-focus light that will distort the intensity profiles of the point sources.

2.2.2 Measurement of depth of focus for a point source

The intensity of a point source falls off as a function of the inverse square of the distance from the focal plane. Figure 2.3 shows a plot of fluorescent intensity against distance from the focal plane; the method of measurement is discribed in the legend. The depth of focus, which was defined by the Rayleigh quarter wavelength limit corresponds to a reduction in intensity at the centre of the pattern from unity to about 0.8 (Longhurst, 1973). This condition is marked by the rectangle on Fig. 2.3, giving a measured depth of focus of ± 1.8 µm. This value may be an overestimate caused by the finite size (0.3 µm diameter) of the fluorescent bead which was assumed to be a point source.

2.2.3 Outline of the problem of resolution with three-dimensional fluorescent sources

Fluorescence imaging often involves thick specimens (5-100 µm) in which the fluorescent indicator is distributed throughout the specimen. This situation occurs in a number of biological applications of fluorescent microscopy, most

Figure 2.3 Intensity fall off from a point source with distance from the focal plane

The graph shows the normalized spot intensity for a point source at different distances above and below (-) the focal plane. A 0.3 μm diameter fluorescent bead (Polysciences Inc., Warrington) suspended in agar (20 g/l made up in saline, Medium C, Table 2.3) and illuminated with 380 nm light was used as the point source. With the bead in focus, a circle with the same position and diameter as the bead was drawn on the image. The total fluorescent light falling on the circle was measured while the microscope was focused above and below the bead. The rectangle on the graph corresponds to the position where the intensity falls to 0.8 of the maximum (in focus) value and indicates a vertical depth of field of ±1.8 μm (Longhurst, 1973). Slack in the focusing mechanism caused the small shifted the position of the curve.

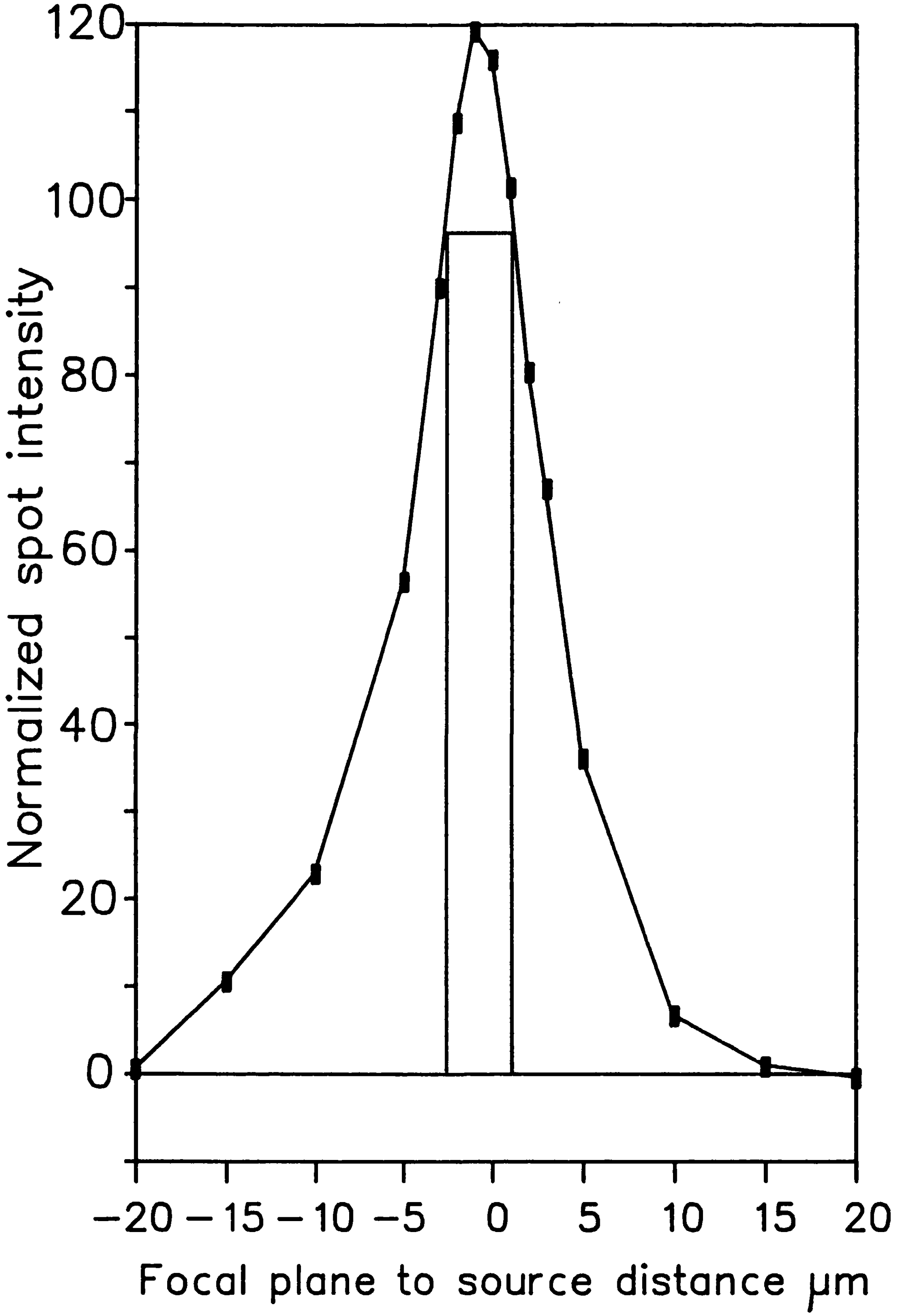
120
100
80
60
40
20
0
Normalized spot intensity
−20
−15
−10
−5
0
5
10
15
20
Focal plane to source distance μm

notably in the measurement of cytosolic calcium and pH. During excitation of the fluorophor the entire volume of the specimen in the microscope field of view emits light. This results in contamination of the image with out-of-focus information from planes above and below the focal plane (Fig. 2.4). The defocused projections from other focal planes seriously impair the spatial resolution that can be achieved. In order to extract quantitative results from such images, the resolution attainable with three-dimensional fluorescent sources has to be determined. The deterioration in resolution dependes on how much defocused light is being collected by the objective. This type of optical behaviour is described by the microscope's point spread function (PSF) (Agard, 1984).

2.2.4 Measurement of the point spread function

The microscope point spread function was measured using a 0.3 μm diameter fluorescent bead (Polysciences Inc., Warrington) suspended in agar (see legend 2.3) as a point source. Images were acquired with the microscope focused above and below the bead. The out-of-focus images appeared as diffraction patterns (Fig. 2.5).

The envelope of the PSF gives the effective acceptance angle of the objective which was found to be 32° (Fig. 2.6). This angle is less than half the theoretical acceptance angle calculated from the numerical aperture of the objective (77°). This mismatch probably arises from the fact that the theoretical acceptance angle represents the angle outside which no light can ever be collected, while the effective acceptance angle is the angle outside which the efficiency of light collection is too low to measure. An alternative explanation, that the NA of the microscope system was being reduced by some optical element beyond the objective was raised with engineers at Zeiss (Welwyn) who ruled out the possibility.

Figure 2.4 Schematic diagram of light collection from a spherical cell injected with fura-2

The diagram shows a cross-section through a lens and the light collection cone for a spherical cell filled with a uniformly distributed fluorescent indicator such as fura-2. Arrows define the Y and Z dimensions and r is the radius of the cell. α is the half-angle of the light collection cone which passes through point P, situated in the plane of focus. x indicates the distance between the focal plane and a disc, of thickness dx. D is equal to the resolution of this optical system. P' is the image of P.

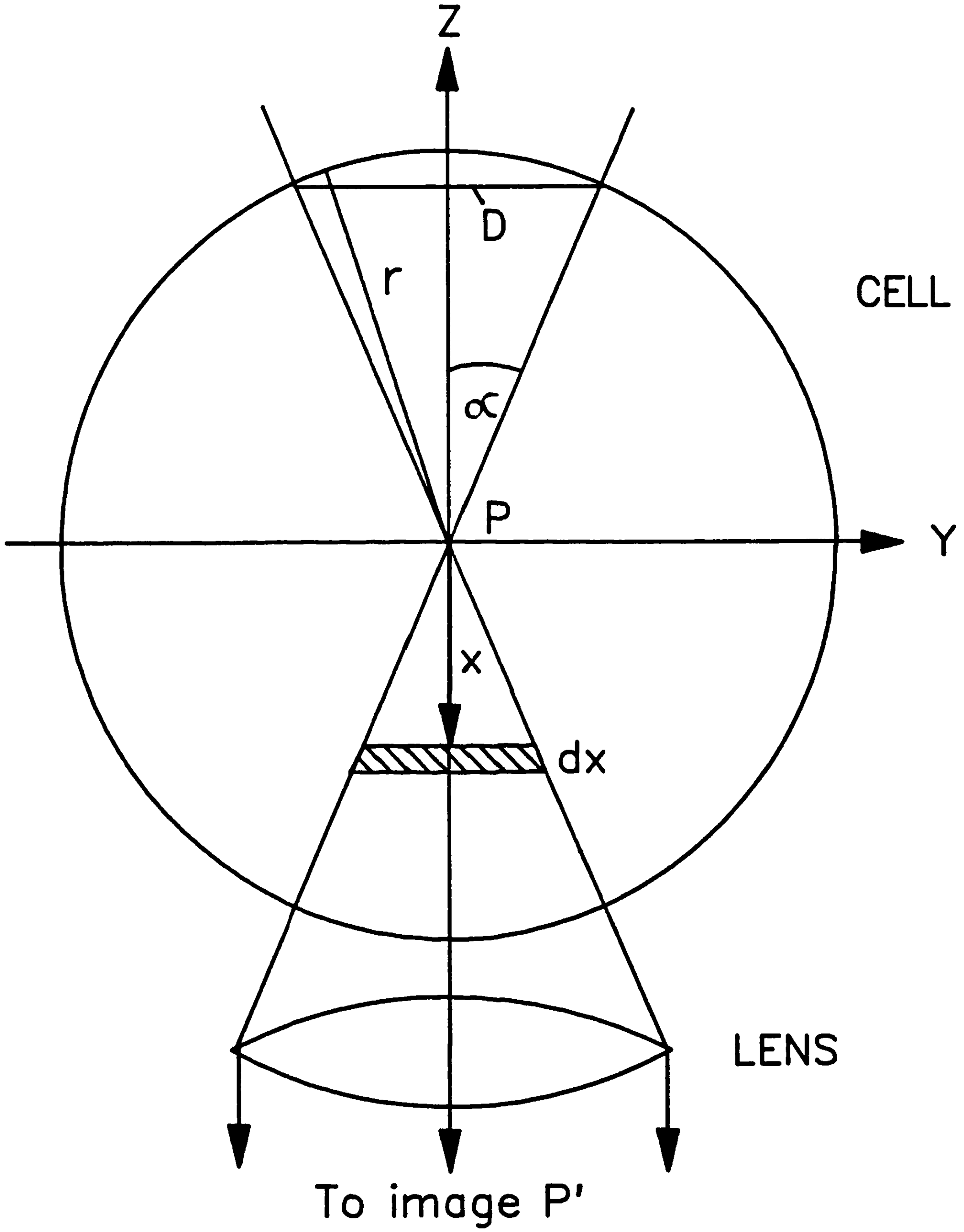
Z
D
r
CELL
α
P
Y
x
dx
LENS
To image P'

Figure 2.5 Intensity profile cross-sections for focal planes above a point source

The curves show cross-sections through the intensity distribution of light at focal planes 0 μm (blue) , 5 μm (green), 10 μm (red) and 15 μm (yellow) above a fluorescent point source for the DIFM fitted with a 1.3 NA Nikon 100x UV-F objective. The X axis is the distance in the X-Y plane from the point source. A fluorescent bead was used as a point source (see Figure legend 2.3). The intensity profiles were measured by placing a rectangle of dimensions 41.5 μm x 1.12 μm on the image with its centre at the position of the bead. The rectangle was divided into 100 segments of 0.42 μm x 1.12 μm, the pixels within each box were averaged, background subtracted and then plotted as a function of distance from the bead position. The secondary maxima seen in the 10 μm and 15 μm traces cannot be explained by geometrical optics and imply that diffraction is occurring.

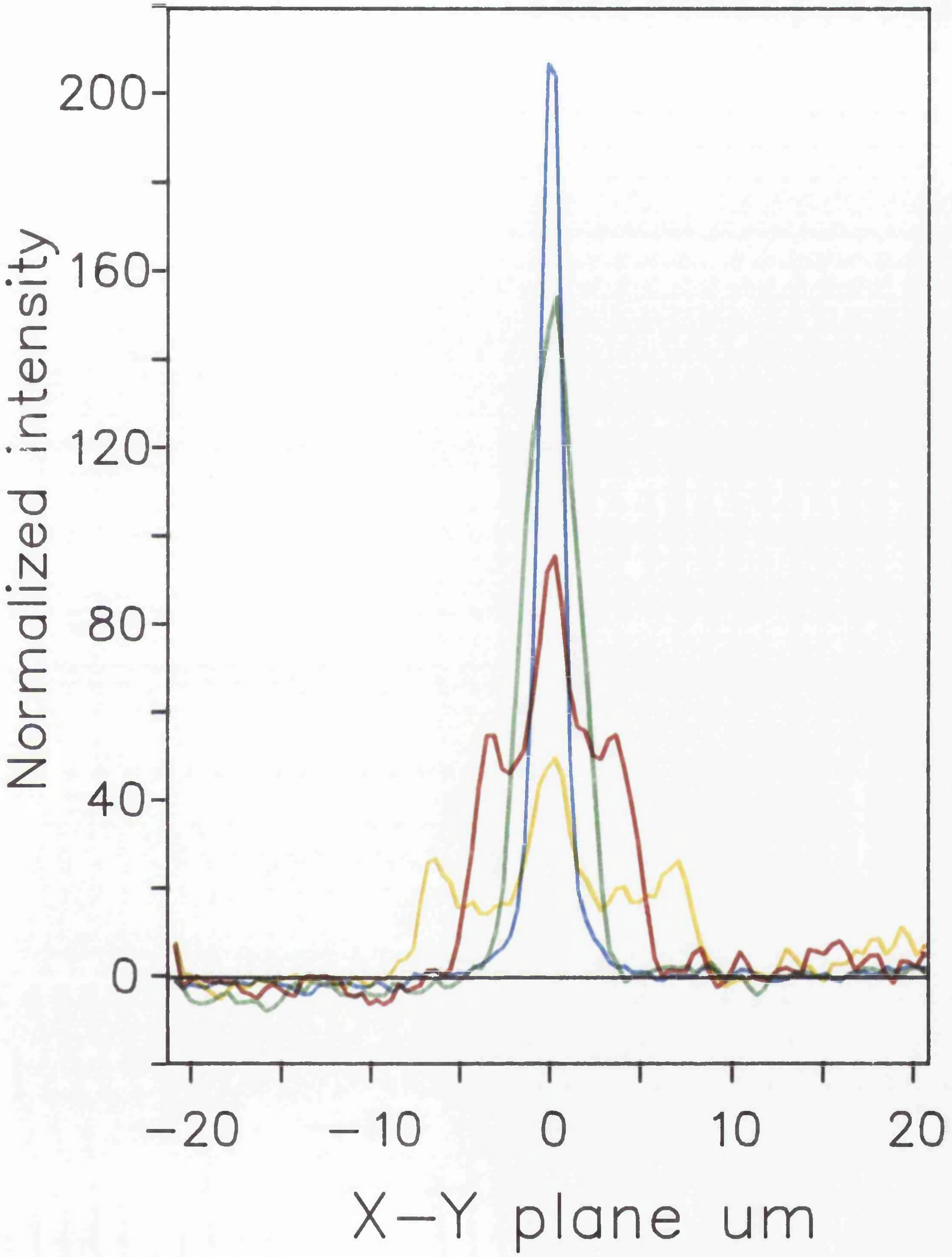
Normalized intensity
200
160
120
80
40
0
-20
-10
0
10
20
X-Y plane um

Figure 2.6 The point spread function

The graph shows a mid-line cross-section through the optical point spread function (PSF) for the DIFM fitted with a 1.3 NA Nikon 100x UV-F objective. The PSF was measured from the intensity profiles like those shown in Figure 2.5, at focal planes above (-) and below a point source (a fluorescent bead suspended in agar see legend 2.3). The envelope of the PSF was determined by measuring average distance from the centre of the point source (in the X-Y plane) at which the intensity profile reached zero (see Figure 2.5) and plotting it against the distance (in the Z-plane) between the point source and the focal plane. The half-angle of the PSF envelope is 32°. This compares with 77° calculated from the quoted NA of the lens 1.3.

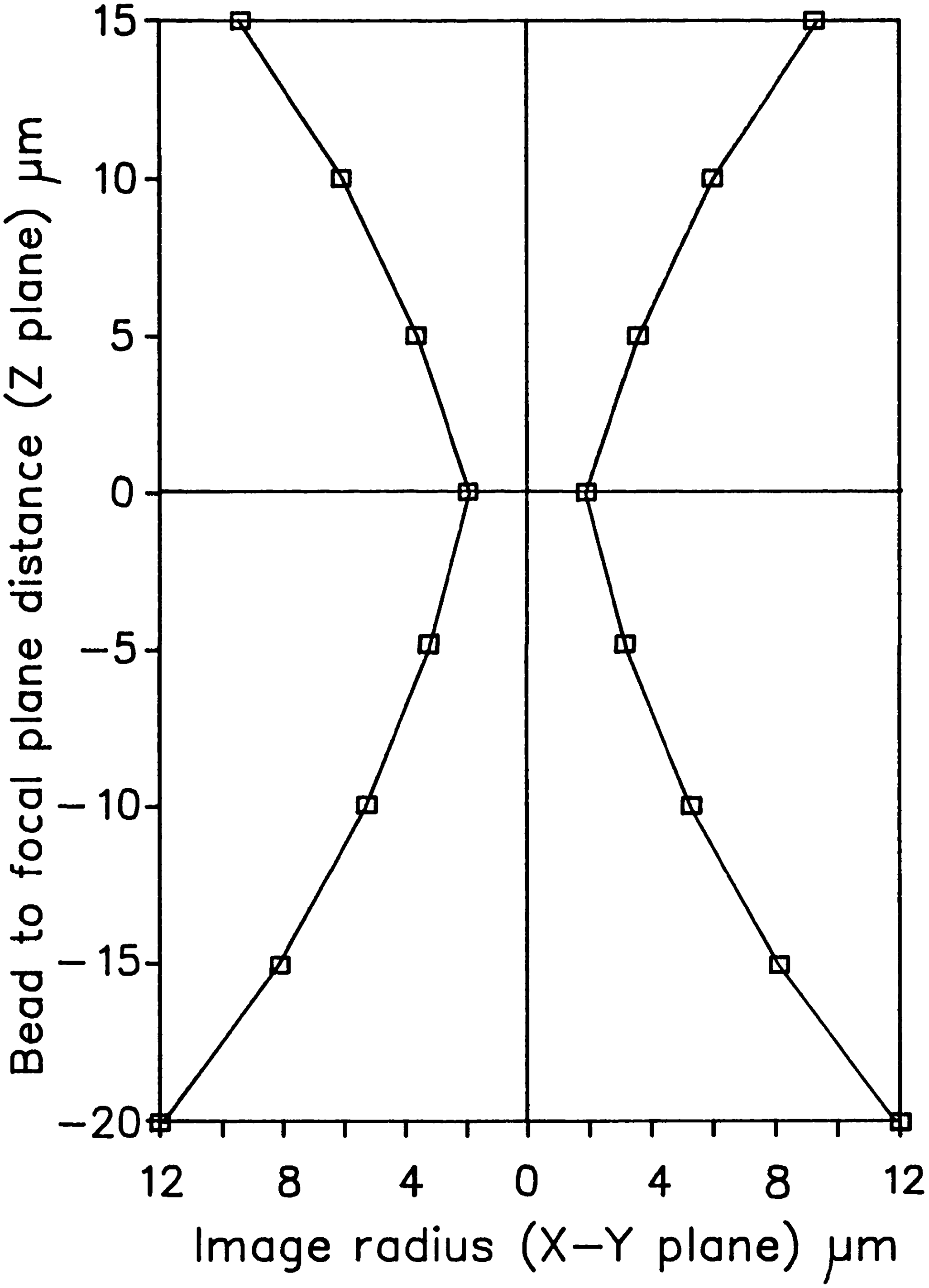
15
10
5
0
−5
−10
−15
−20
12
8
4
0
4
8
12
Bead to focal plane distance (Z plane) μm
Image radius (X−Y plane) μm

Quantitative interpretation of fluorescent images from thick specimens is not straight forward. Having determined the microscope PSF it is possible, using a series of optical sections, to eliminate the out-of-focus information from the image using deconvolution methods (Agard, 1984; Fay *et al.*, 1989; Carrington *et al.*, 1990). This type of analysis is complicated and involves many hours of computation for each image. A less time-consuming alternative was to determine the relationship between specimen thickness and resolution and apply this restriction when analysing images.

2.2.5 The contribution of defocused information from any given plane

The double cone within the cell that contributes light to the image point P' can be thought of as a stack of discs, of equal thickness dx (Fig. 2.4). The volume of a disc, distance x from the centre of the cell is $\pi(x \tan\alpha)^2 dx$, that is, the volume of each disc increases as a function of x^2. However, the contribution of light from each unit volume within the cone to the image at P' is proportional to $1/x^2$. The total contribution of light from each disc is therefore independent of its distance from the focal plane. The intensity at P' is the sum of the contributions of all the discs and will be directly proportional to the thickness of the sphere. For points on the equatorial plane closer to the edge of the cell, the intensity will fall off since the volume of the cell falling within the double cone declines. Figure 2.7 shows that the total light emitted from hemispherical droplets of fura-2 was directly proportional to diameter, as predicted for the analysis above. This result also demonstrates that self-shading of fura-2 will not be a problem for the concentrations used in the intracellular measurements.

2.2.6 The spatial resolution of images of three-dimensional fluorescent specimens

It has been shown that the intensity at any point on the image of a thick specimen is made up mainly from light coming from above and below the plane of focus (Fig 2.4). The resolution of the system in the X and Y directions is

Figure 2.7 Point fluorescence intensity as a function of dye drop thickness

The graph shows the relationship between the maximum point fluorescent intensity and the diameter of a hemispherical drop of 100 µM fura-2. Hemispherical drops were produced by pressure ejection of fura-2 (dissolved in a 100 nM [Ca^{2+}] calcium buffer, Table 2.1b) from a micropipette onto a silane coated coverslip, under liquid paraffin. Fluorescent intensity was measured at the centre of the drop and normalized by dividing by [camera voltage + 0.25]. The relationship was linear, indicating that self-shading (absorption) was negligible for specimens up to 25 µm thick. The line was fitted by eye.

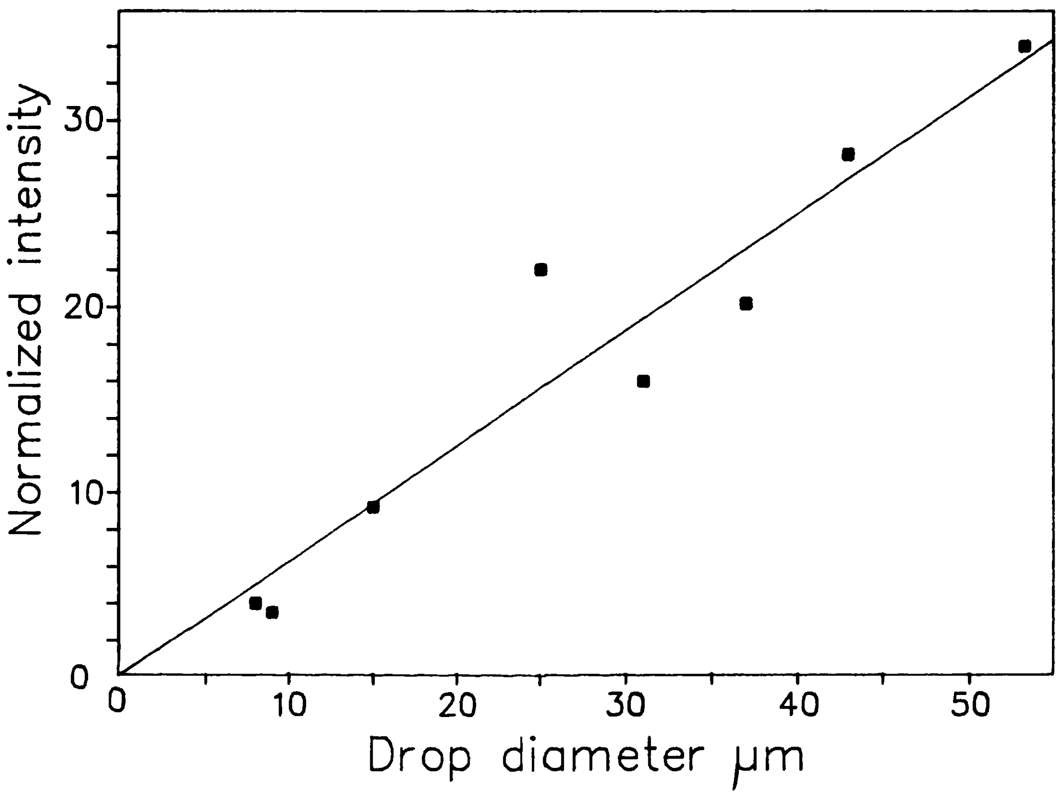

Normalized intensity
0
10
20
30
0
10
20
30
40
50
Drop diameter μm

therefore highly dependent on the Z dimension.

Using a spherical model cell (Fig 2.4) the worst resolution in the X-Y direction is equal to the maximum PSF cone diameter within the cell. Thus for the plane of focus at the equator, the resolution is:

$$D = 2\, r \sin \alpha$$

If α were 77°, the value calculated from the numerical aperture (1.3), then resolution would be extremely low, 97 μm for a 100 μm diameter cell! However, the measured acceptance angle, which was found to be 32°, is the appropriate value to use, giving a resolution of 53 μm for a 100 μm diameter cell. The resolution improves for points in the X-Y plane closer to the edge of the cell, but gets worse the further the focal plane from the equator.

The growth cones studied in this project approximate more closely to a disc of cytoplasm than a sphere. Growth cone thickness was measured to be 5.4 ± 0.5 μm (n=8). For such thin structures the microscope could be focused with an accuracy such that the focal plane was somewhere between the upper and lower growth cone membranes. For this case, a disc of thickness t and diameter greater than the maximum PSF cone diameter, will give a resolution of:

$$D = 2t \tan \alpha$$

Where t is the growth cone thickness and α is the acceptance angle of the lens (32°). This gives an X-Y resolution of 7 μm for a 5.4 μm thick growth cone. This limit is highly dependent on accurate focusing.

2.3 Calcium measurement using a fluorescent dye

2.3.1 The basis of calcium ion measurement using a fluorescent probe

Fluorescence is the photon emission from a paired electron returning from an excited to a lower electron state. This type of transition, which occurs without any change in spin multiplicity, has a nanosecond time scale. Fluorescence should not be confused with phosphorescence which is the emission of photons from transitions between states of different multiplicity. The necessary 'flip' in the spin to a singlet state has a low probability which explains the much slower decay times for phosphorescent materials. Excitation of the fluorophor occurs by absorption of a photon of sufficient energy to produce transition from the ground state to the first or higher electronic states, each of which has several vibrational levels. Since vibration is much faster than the fluorescent lifetime, most of the excess vibrational energy dissipates through collisions with the surroundings. This decay from excited to ground vibrational levels explains the Stokes shift in the wavelength between the excitation and emission spectra of the fluorophor.

Changes in the excitation and emission spectra and quantum efficiency of fluorescent dyes during selective binding of an ion species can be used to measure concentration of that species. Fura-2, which is based on the calcium chelator ethylene glycol-bis(β-aminoethylester) N,N,N',N'-tetraacetic acid (EGTA), is a fluorescent dye which has a high selectivity for Ca^{2+} (Grynkiewicz *et al.*, 1985). The excitation spectrum of fura-2 shifts to shorter wavelengths on binding Ca^{2+} and the quantum efficiency of the Ca^{2+}-bound species is approximately double that of the free dye. Both of these changes are used to indicate $[Ca^{2+}]$. Fura-2 was used in the present study to measure cytosolic calcium concentration for several reasons. Fura-2 has a dissociation constant of 224 nM at 36 °C (Grynkiewicz *et al.*, 1985) which is in the middle of the physiological range of calcium concentrations, it binds calcium with high selectivity over other divalent ions and its high quantum efficiency and large shift in excitation spectra on binding calcium make it highly suited to the ratio imaging technique.

2.3.2 Spectrofluorimetry measurements using fura-2

The excitation spectrum of fura-2 was measured (using a Perkin-Elmer 650-10S fluorescence spectrophotometer) in the presence of calcium-free and calcium-saturated solutions. Figure 2.8a shows such excitation spectra. The peak of the spectrum occurred at an excitation wavelength of 368 nm for the free dye and 340 nm for the calcium-bound form. This result is similar to that found by Grynkiewicz *et al.* (1985). Cd^{2+}, a calcium channel blocker, was used during some imaging experiments. Although Cd^{2+} is unlikely to enter the growth cone during calcium current activation (Lansman *et al.*, 1986) it was important to determine the effect of Cd^{2+} on fura-2. The peak of the spectrum of cadmium-bound fura-2 occurred at the same excitation wavelength as the calcium-bound form, however the fluorescence emission was greater, indicating a higher quantum efficiency for the cadmium-bound species.

The fura-2 excitation spectra was measured within the cell cytoplasm in collaboration with Dr R. Jacob at the Smith Klien and French laboratories. Figure 2.8b shows a calcium saturated *in vivo* and *in vitro* spectrum measured using a Spex microfluorimeter connected to a Zeiss IM microscope and Nikon UV-F objective. The shape of the *in vivo* and *in vitro* spectra was the same; this shows that the calcium-bound form of the dye was unaffected by the cytoplasmic environment. The calcium buffers used in the *in vitro* calcium saturated spectra of Figs 2.8a and 2.8b were identical. The apparent shift of the spectrum towards longer wavelengths, and the maximum at 360 nm in Fig. 2.8b, was caused by heavy filtering of short wavelengths by the microscope objective.

Figure 2.8 Fura-2 excitation spectra *in vitro* and *in vivo*

Part a shows the uncorrected excitation spectrum of calcium-free and calcium-bound fura-2. Each spectrum was measured for excitation wavelengths between 290 nm and 450 nm, and a collection wavelength of 510 nm, on a fluorescence spectrophotometer (Perkin Elmer 650-10S) with a solution containing 0.6 µM fura-2 at 20 °C. The calcium-free and saturated solutions had an ionic composition similar to the intracellular environment (solutions 0 and SAT Table 2.1b). The peak fluorescence occurred at an excitation wavelength of 368 nm for the free dye (Ca++ free) and 340 nm for the calcium-bound form (Ca++ saturating).

Part b shows the uncorrected excitation spectrum of calcium-bound fura-2 measured in a cuvette (in vitro) and in the cytoplasm (in vivo) of a N1E-115 neurobastoma cell. The spectra were measured for excitation wavelengths between 330 nm and 400 nm on a Spex microfluorimeter (model CM3) at 20 °C, the cytoplasmic concentration of the dye was unknown. The solution used for the in vitro measurement was the same as Part a. The calcium bound form of the dye was unchanged by the cytoplasmic environment, as the shape of the spectrum was not changed by the cytoplasmic environment. The shape of the specrtum in Part b with peaks at 343 nm and 358 nm and fall off at shorter wavelengths is the result of filtering by the microscope objective and sensitivity function of the microfluorimeter.

a,

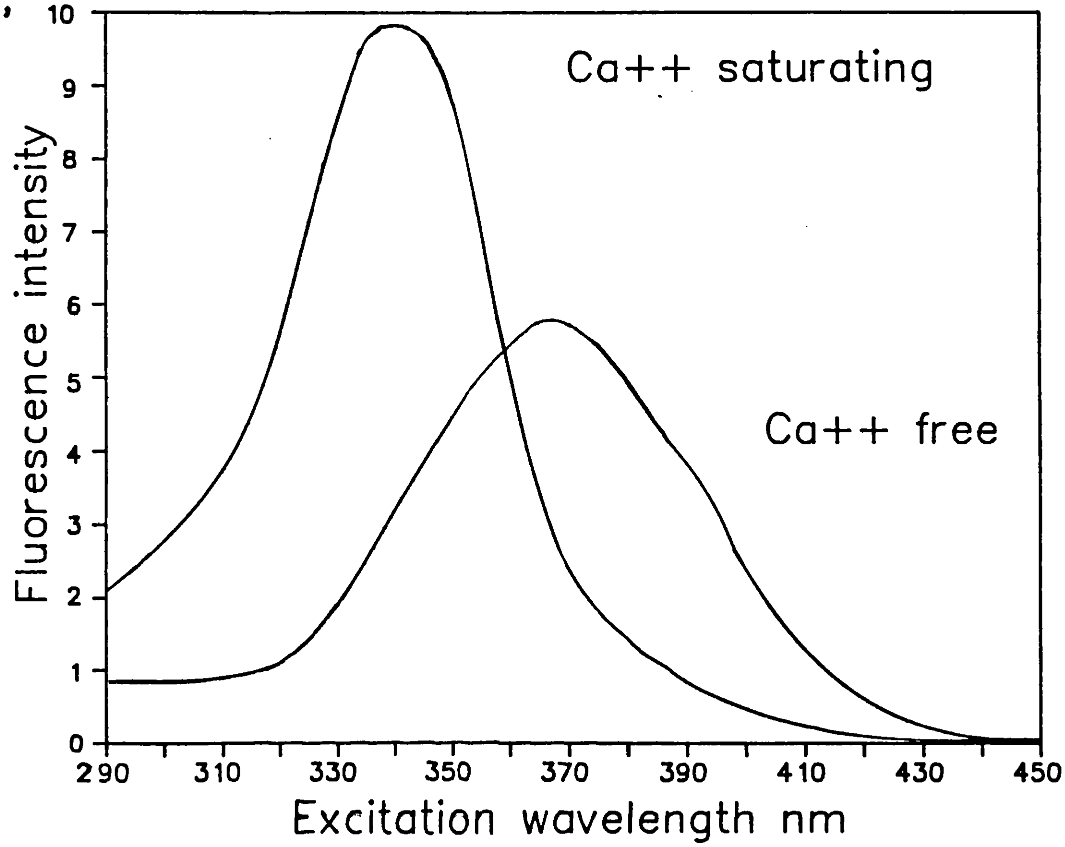
Ca++ saturating
Ca++ free
Fluorescence intensity
0
1
2
3
4
5
6
7
8
9
10
290
310
330
350
370
390
410
430
450
Excitation wavelength nm

b,

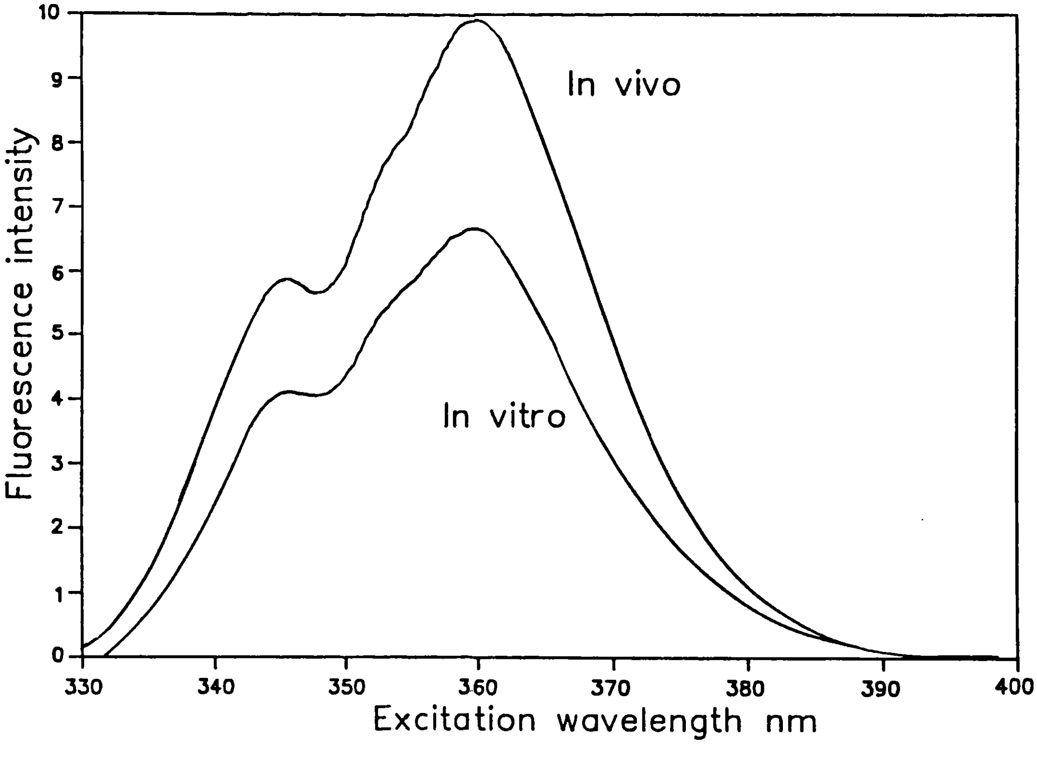
In vivo
In vitro
Fluorescence intensity
0
1
2
3
4
5
6
7
8
9
10
330
340
350
360
370
380
390
400
Excitation wavelength nm

2.3.3 Calculation of calcium concentration using the ratio method

The shift in the excitation spectrum of fura-2 on binding calcium (Fig. 2.8a) can be used to calculate $[Ca^{2+}]$, independent of total dye concentration, path length, or absolute sensitivity of the instrument (Grynkiewicz *et al.*, 1985). As shown above (Fig. 2.7) self-shading is not a problem with the range of path lengths encountered, so the fluorescence intensity from any given fluorophor is proportional to the concentration of that species. If the dye is excited at two different wavelengths 350 nm and 380 nm, the corresponding total fluorescent intensities will be I_{350} and I_{380}. Each of these intensities will be composed of light originating from two dye species, calcium free and calcium bound. The fluorescence emission from each dye species is a product of the dye concentration of that species (C_f and C_b) and a species-specific coefficient (S_f and S_b) which includes a number of factors such as excitation intensity, path length, quantum efficiency and instrument efficiency.

Excitation at 350 nm gives

$$I_{350} = S_{f350}\ C_f + S_{b350}\ C_b \qquad (1)$$

and excitation at 380 nm gives

$$I_{380} = S_{f380}\ C_f + S_{b380}\ C_b \qquad (2)$$

Fura-2 complexes calcium with 1 : 1 stoichiometry thus

$$\underset{C_f}{\text{free dye}} + \underset{[Ca^{2+}]}{Ca^{2+}} \leftrightarrow \underset{C_b}{Ca^{2+}\text{ bound dye}} \qquad (3)$$

The law of mass action gives

$$C_b = C_f\ [Ca^{2+}]\ /\ Kd \qquad (4)$$

where Kd is the dissociation constant. The fluorescence ratio R is

$$R = I_{350}\ /I_{380} = (S_{f350}\ C_f + S_{b350}\ C_b)\ /\ (S_{f380}\ C_f + S_{b380}\ C_b) \qquad (5)$$

substituting for C_b, equation (4)

$$R = (S_{f350} + S_{b350}\ [Ca^{2+}]\ /\ Kd)\ /\ (S_{f380} + S_{b380}\ [Ca^{2+}]\ /\ Kd) \qquad (6)$$

This can be rearranged to give an expression for $[Ca^{2+}]$

$$[Ca^{2+}] = Kd\ (\{\ R - (S_{f350}/S_{f380})\}\ /\{(S_{b350}/S_{b380}) - R\}\ )\ (S_{f380}/S_{b380}) \qquad (7)$$

S_{f350}/S_{f380} is the limiting value that R can have at zero $[Ca^{2+}]$ (R_o). Similarly S_{b350}/S_{b380} is the ratio value at saturating calcium (R_{sat}).

Thus

$$[Ca^{2+}] = Kd\ (\ S_{f380}/S_{b380}\ )\ (\ R - R_o\ )\ /\ (\ R_{sat} - R\ ) \qquad (8)$$

Where Kd (S_{f380}/S_{b380}) is system dependent and is the $[Ca^{2+}]_i$ at which R is midway between R_o and R_{sat} (Fig. 2.9).

2.3.4 Calibration of the DIFM for $[Ca^{2+}]_i$ measurement

The absolute ratio, r, was calculated by dividing the background-subtracted fluorescence image during 350 nm excitation by the background-subtracted fluorescence image during 380 nm excitation. The absolute value of the ratio depends on the relative intensity of the two excitation wavelengths. The ratio was normalized such that R = r / r' where r' was the ratio for a standard Ca^{2+}-free solution (solutions Table 2.1). This procedure compensates for any day to day variation in the relative beam intensities. Day to day variation was not a problem with a single light source, however the normalization was carried out because the image acquisition software was constructed from programmes purchased from Dr. R. Tsien, who has a DIFM fitted with a dual light source.

The parameters Kd (S_{f380}/S_{b380}), R_o and R_{sat} were determined (Fig.2.9) for the DIFM using calcium EGTA-buffers containing 100μM fura-2. The free calcium concentration of the ionic strength and temperature corrected calcium EGTA buffers was calculated using the stability constants (Martell and Smith, 1974). The buffers had an ionic composition and pH similar to the intracellular environment (Table 2.1). The values at 34 °C were R_o=1 (R measured for solutions of zero calcium, Table 2.1a), R_{sat}=21.9 (R measured for solutions of saturating calcium, Table 2.1a) and Kd (S_{f380}/S_{b380})= 3.9 μM ([Ca^{2+}] for which R was midway between R_o and R_{sat}, using buffers 0 to SAT in Table 2.1a for the curve, Fig. 2.9). The values at room temperature (20 °C) were R_o=1 (Table 2.1b), R_{sat} (Table 2.1b) = 14.1 and Kd(S_{f380}/S_{b380})= 2.13 μM (buffers 0 to sat in Table 2.1b).

The spatial distribution of the fluorescence ratio was presented as a pseudocolour image made up of an array of 512 x 512 pixels, with a colour scale running from blue to red to indicate the pixel ratio and therefore $[Ca^{2+}]_i$ (Fig. 4.1).

2.3.5 Calculation of calcium changes using the single wavelength method

If the absolute value is known, changes in $[Ca^{2+}]_i$ can be calculated from the change in the fluorescence intensity at one excitation wavelength. This

Table 2.1

a, Calcium EGTA buffers at 36 °C

Buffers contained 19.1mM EGTA (purity measured to be 95.5%), 20mM HEPES and 70mM KCl at pH 7.0 and ionic strength 0.16M. The free and added calcium concentrations were:

$[\mathrm{Ca}^{2+}]_{\mathrm{Free}}$ nM	$[\mathrm{CaCl_2}]_{\mathrm{Added}}$ mM
0	0.000
100	4.391
500	11.438
1000	14.309
3000	17.185
5000	17.906
7000	18.235
SAT	30.000

b, Calcium EGTA buffers at 20 °C

The buffers contained 10mM EGTA, 10mM HEPES, 75mM KCl, 10mM NaCl and 1mM free Mg at pH 7.0. The free calcium and added calcium and magnesium were:

$[\mathrm{Ca}^{2+}]_{\mathrm{Free}}$ nM	$[\mathrm{CaCl_2}]_{\mathrm{Added}}$ mM	$[\mathrm{MgCl_2}]_{\mathrm{Added}}$ mM
0	0.000	1.280
100	2.108	1.218
500	5.720	1.120
1000	7.270	1.075
3000	8.890	1.030
SAT	15.000	1.000

Figure 2.9 Calibration of ratio units

The graph shows fluorescent ratio measurements for a range of calcium concentrations using the DIFM fitted with a 1.3 NA Nikon 100x UV-F objective at 34 °C. Calibration solutions were made up by adding 100 μM fura-2 to the calcium buffers listed in Table 2.1a. A 10 μl drop of calibration solution was sandwiched between two coverslips and images were taken during illumination with 350 nm and 380 nm light. Ratios were calculated by dividing the background-subtracted 350 nm image by the background-subtracted 380 nm image, the ratios were then normalized by dividing by the ratio obtained for the calcium-free solution. R_o the ratio for the calcium-free solution, R_{sat} the ratio for a calcium saturated solution and Kd (s_{f380}/S_{f350}) the calcium concentration corresponding to the mid-point between R_o and R_{sat} (dotted line). The data are fitted by the theoretical relationship $[Ca^{++}] = Kd(S_{f380}/S_{f350})(R - R_o)/(R_{sat} - R)$, where $R_o = 1$, $R_{sat} = 21.9$ and $K_d(s_{f380}/S_{f350}) = 3.9$ μM (see Section 2.3.3).

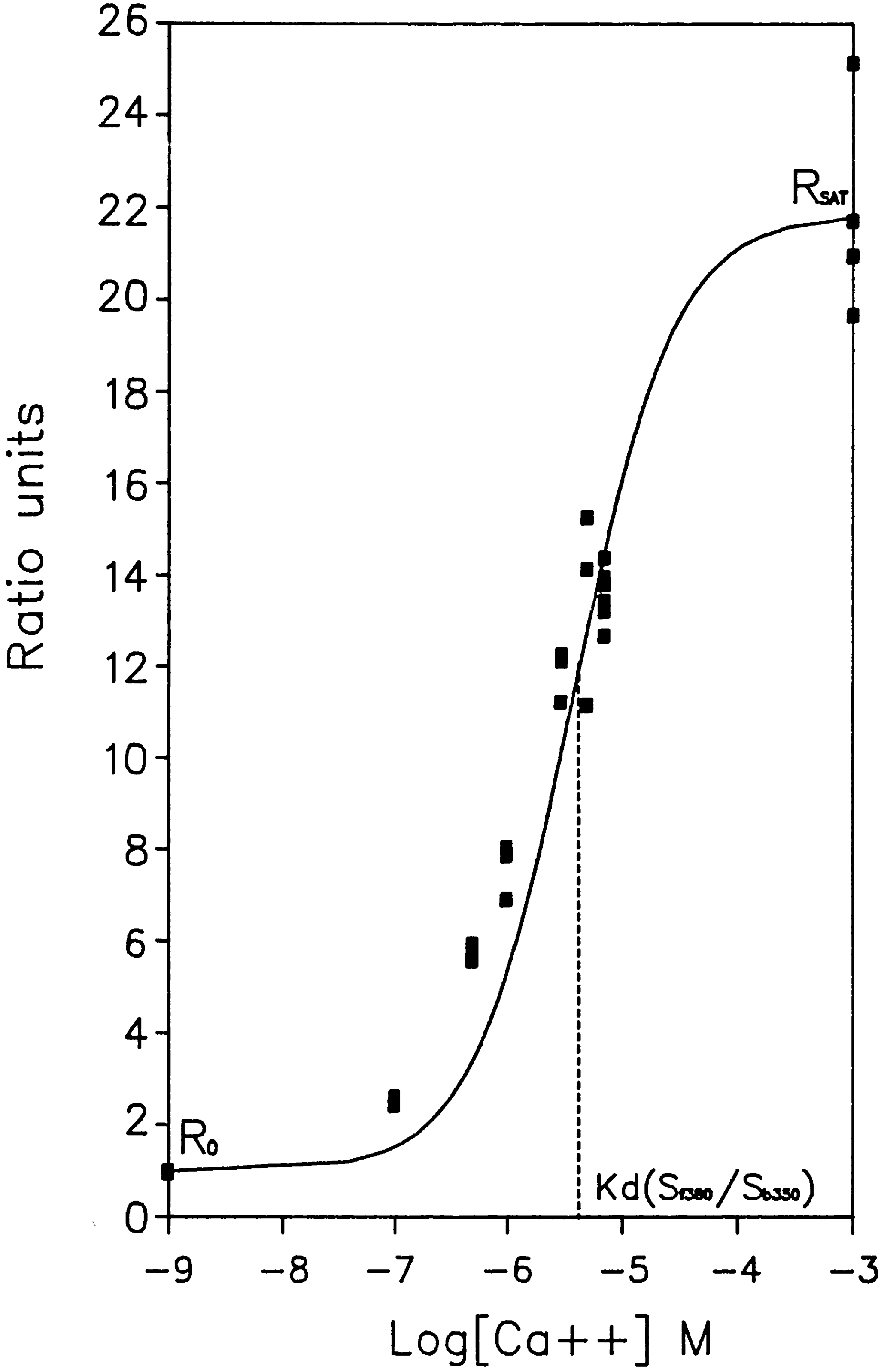

Ratio units
26
24
22
20
18
16
14
12
10
8
6
4
2
0
R_{SAT}
R_0
$Kd(S_{f380}/S_{b350})$
−9
−8
−7
−6
−5
−4
−3
Log[Ca++] M

approach, although more prone to problems, is useful because it increases the temporal resolution of the DIFM from several seconds to 60 ms by eliminating the requirement for the narrow-pass filters to be mechanically swiched. This time resolution is essential for investigating problems such as the spatial distribution of voltage-dependent calcium influx.

Fura-2 binds calcium with a 1 : 1 stoichiometry (Grynkiewicz *et al.*, 1985) giving (as above)

free dye + Ca^{2+} ↔ Ca^{2+} bound dye

C_f $[Ca^{2+}]$ C_b

Then, if the total [dye], $C_t = C_f + C_b$ (1)

from the law of mass action

$[Ca^{2+}] = Kd\ C_b / C_f$ (2)

The total fluorescence emitted by fura-2, at a constant concentration C_t, when it is excited with 380 nm light is the sum of fluorescence emitted by the calcium-free and calcium-bound species of the dye. Assuming negligible absorption the total fluorescence, I_{380} is linearly proportional to the concentrations of the fluorescent species:

$I_{380} = S_{f380}\ C_f + S_{b380}\ C_b$ (3)

Now for a Ca^{2+}-free solution $C_b \rightarrow 0$ therefore $C_f = C_t$ and $I_{380} \rightarrow I_{max}$ thus

$$S_{f380} = I_{max} / C_t \qquad (4)$$

similarly for a Ca^{2+} saturating solution $C_f \rightarrow 0$ therefore $C_b = C_t$ and $I_{380} \rightarrow I_{min}$

$$S_{b380} = I_{min} / C_t \qquad (5)$$

Substituting equation (4) and (5) into equation (3) gives

$$I_{380} = I_{max} C_f / C_t + I_{min} C_b / C_t \qquad (6)$$

substituting equation (1) for C_t and multiplying out the brackets gives

$$I_{380} C_f + I_{380} C_b - I_{max} C_f - I_{min} C_b = 0$$

rearranging gives

$$C_b / C_f = (I_{max} - I_{380}) / (I_{380} - I_{min}) \qquad (7)$$

By substituting (7) into (2) concentration of dye species are replaced by measurable fluorescence intensities. The relationship between calcium concentration and fluorescence is therefore

$$[Ca^{2+}] = Kd\ (I_{max} - I_{380}) / (I_{380} - I_{min}) \qquad (8)$$

The parameters I_{max} and I_{min} were determined *in situ* with calcium-saturating and calcium-free solutions during excitation with 380 nm light. At 20 °C with 100 μM fura-2 and EGTA buffers 0 and SAT (Table 2.1b) $I_{min} = 0.102\ I_{max}$. At 34 °C with buffers 0 and SAT (Table 2.1a) $I_{min} = 0.119\ I_{max}$.

Thus

$$[Ca^{2+}] = Kd\ (I_{max} - I_{380})/(I_{380} - f\ I_{max}) \qquad (9)$$

where f = 0.102 at 20 °C; 0.119 at 34 °C.

Rearranging this equation gives a formula for I_{max} in terms of $[Ca^{2+}]$ and I_{380}:

$$I_{max} = I_{380}\ ([Ca^{2+}] + Kd)/(f\ [Ca^{2+}] + Kd) \qquad (10)$$

The experimental protocol was as follows. First, the resting level of $[Ca^{2+}]$ was measured using the ratio method (see section 2.3.3 above). The intensity of fluorescence for 380 nm excitation (I_{380}) at this resting level of $[Ca^{2+}]$ was designated I_o. Experimental manipulation of the membrane potential caused a fall in the signal from I_o to a particular level I_{380}.

I_{max} was calculated by entering the values of rest $[Ca^{2+}]$ and I_o (the I_{380} value at resting $[Ca^{2+}]$) in equation 10. The value of $[Ca^{2+}]$ corrisponding to a particular I_{380} was then calculated using equation 9. The results were expressed as the change of $[Ca^{2+}]$ from the resting level.

Pseudocolour images with a colour scale to indicate change in calcium concentration from the resting level are used to present the data (Fig. 5.1). These images were produced by dividing background-subtracted images during the response, by a background-subtracted control image. Each of the pixels in the resulting image was coded with a colour scale running from blue representing no change in calcium concentration to red indicating a large change.

2.3.6 Calculation of dye concentration

It was important to estimate the concentration of fluorescent dye in the cytoplasm because the indicator acts as a strong buffer and might have toxic effects at high levels. Figure 2.7 shows that the relationship between signal intensity and the maximum thickness of a hemispherical drop of 100 μM fura-2 under liquid paraffin was linear. This demonstrates that the self-shading of both the excitation light and emitted fluorescence was negligible for the path lengths used. The slope of the graph gave the constant of proportionality between the normalized signal intensity and specimen thickness. Multiplying both sides by [dye], substituting and then rearranging gave:

$$[\text{dye}] = \text{Const} \times \text{Normalized intensity} \,/\, \text{specimen thickness}$$

where the constant of proportionality was dye specific (for fura-2 during 350 nm excitation, const = 129) and normalized intensity = signal intensity / (camera tube voltage on an arbitry scale from 0.25 to 10.25). The specimen thickness was estimated assuming that the cross-section of the cell body at its shortest diameter was a semicircle.

2.3.7 Problems encountered using quantitative fluorescence measurement

Several factors in both the ratio and single wavelength fluorescence techniques can lead to errors in $[Ca^{2+}]_i$ measurement. The calculation of $[Ca^{2+}]_i$ assumes that fura-2 behaves in the same way within the cell cytoplasm as in the calibration solutions. Although there is some evidence that the behaviour of fura-2 does change in the cytoplasm of skeletal muscle (Konishi *et al.*, 1988) there was no evidence that this occurred in cytoplasm of N1E-115 cells. The *in vivo* and *in vitro* calcium-saturated excitation spectra was similar (Fig. 2.8b) and the calculated $[Ca^{2+}]_i$ values were in the same range as those recorded in nerve cells using calcium-sensitive intracellular microelectrodes (Alvarez-Leefmans *et al.*, 1981; Silver and Erecinska, 1990). These findings do not rule out the possibility of errors arising from changes in the dye environment, however the important findings of this thesis are not dependent on the absolute level of $[Ca^{2+}]_i$. A more serious problem would arise if spatial variations of dye behaviour within the cytoplasm, caused by specimen thickness, UV absorbance, scattering and beam inhomogeneity gave rise to apparent spatial gradients of $[Ca^{2+}]_i$. To test for possible artifacts of this sort, the cells were injected with the dye 8-aminonaphthalene-1,3,6-trisulphonic acid (ANTS, Molecular Probes, Oregon), which has similar excitation and emission spectra to fura-2 but is unaffected by pH, $[Ca^{2+}]$ or $[Mg^{2+}]$. Images of growth cones injected with ANTS represent a pixel by pixel plot of R, where R was normalized such that R=1 for ANTS in the *in vitro* Ca^{2+}-free standard solution (Table 2.1a). Although there was a shift in the fluorescence ratio when the ANTS entered the cytoplasm, the spatial distribution of the ratio signal was completely uniform.

Growth cones, or regions of growth cones that differ in motility may have different concentrations of either f-actin or g-actin. In order to test for a possible effect of f-actin or g-actin on either the spectra or Kd of fura-2, the spectrum of 1 μM fura-2 was measured in a buffer of 100 mM KCl, 5.67 mM $CaCl_2$, 8 mM BAPTA (Tsien, 1980), 0.2 mM mercaptoethanol, 0.2 mM adenosine triphosphate and 1 mM tris(hydroxymethyl)aminomethane, pH 8.0. In this buffer approximately 40% of fura-2 was bound to Ca^{2+}, therefore a change in Kd, or a spectral change of either the free or calcium-bound dye, would change the measured spectrum. However, the presence of g-actin at 1 mg/ml had no effect on the spectrum. Addition of spermine in a final concentration of 60 μM polymerized the actin (Grant *et al.*, 1983), but did not alter the spectrum.

Fura-2 is a high affinity calcium buffer. The concentration of fura-2 necessary to produce a fluorescence intensity sufficient to be detected by the camera ranged from 105 μM to 1037 μM (average 390 μM). Although the buffering capacity of the growth cone is not known this concentration of fura-2 must represent a significant increase in buffering power. It was necessary therefore, to investigate the effect of this added buffering component on the magnitude of both the resting levels and gradients of calcium. The effective diffusion constant for Ca^{2+} in nerve cell cytoplasm has been measured as 8.3×10^{-7} cm^2/sec (Nasi and Tillotson, 1985). After injection of fura-2 most of the freely diffusible Ca^{2+} will be bound to fura-2. The effective diffusion constant of fura-2 inside cells is equal to the value in free solution, 3.6×10^{-7} cm^2/sec (Baylor and Hollingworth, 1988) which is approximately half the effective diffusion constant for Ca^{2+}. Thus injection of fura-2 might be expected to increase the amplitude of spatial gradients slightly. However, the presence of fura-2 will not change the direction of $[Ca^{2+}]_i$ gradients. Injection of fura-2 might be expected to reduce the resting level of $[Ca^{2+}]_i$, with the greatest reduction of $[Ca^{2+}]_i$ being seen in those cells with the highest intracellular concentration of fura-2. However, R values for the cell body (mean = 1.46 ± 0.04, $[Ca^{2+}]_i = 88 \pm 7$ nM, n=19) showed no statistical correlation with fura-2 concentration (Bulmer, 1967) (correlation coefficient = -0.10). This implies that the injection of fura-2 to these levels does not disturb the ability of the cells to regulate $[Ca^{2+}]_i$ in the long term.

Autofluorescence from the cells, measured before injection of fura-2 was negligible compared with the fura-2 fluorescence signal and therefore was not corrected for. Bleaching of fura-2 and dye loss from the cell was monitored by measuring the change in fluorescence with time at both excitation wavelengths. Both these factors were negligible over the period taken to make ratio or single wavelength measurement.

Single wavelength measurements were tested for possible artifacts, such as a change in fura-2 concentration or specimen thickness, by measuring the intensity change while membrane potential was kept constant and also by showing that the direction of the change reversed when exciting at 350 nm instead of 380 nm light.

2.4 Cell culture

N1E-115 neuroblastoma cells were maintained in Dublecco's modification of Eagles medium (DMEM) buffered with 1.21 g/l $NaHCO_3$ and supplemented with 6% fetal calf serum in an atmosphere of 5% CO_2 at 36 °C. Cells to be used for experimentation were suspended in the same medium and plated onto glass coverslips that had been bathed in a solution containing 20 μg/ml polylysine (Sigma). Either immediately or two days after plating, dimethyl sulphoxide (DMSO; 2% by volume) or 0.5 mM dibutyryl cyclic adenosine monophosphate (dBcAMP) was added to the bathing medium to promote differentiation (Kimhi *et al.*, 1976; Chalazonitis and Greene, 1974). After one to sixteen days in the differentiating medium coverslips were transferred to the microscope stage and bathed in DMEM or one of the external media listed in Table 2.3.

2.5 Correlation of growth cone behavioural states with $[Ca^{2+}]_i$

2.5.1 Experimental procedure

In experiments where growth cone behaviour was studied, DMSO-differentiated cells were bathed in differentiation medium in which 10 mM N-[2-hydroxyethyl]piperazine-N'-[2-ethanesulfonic acid] (HEPES) replaced $NaHCO_3$. The bathing solution was maintained between 34 and 36 °C and covered with a layer of paraffin oil, to improve thermal insulation and reduce evaporation.

Individual cell bodies were impaled with a pipette. These were pulled from pyrex glass (Clark electromedical, GC150F-10) on a Kopf vertical microelectrode puller (David Kopf Instruments, Cal) and had a resistance of about 20 MΩ when filled with 2 M KCl. The pipettes contained 10 mM fura-2 (Molecular Probes, Oregon), 140 mM KCl and 5 mM HEPES, pH 7.0. Fura-2 was injected by applying pressure to the back of the pipette or by iontophoresis at 0.1-0.5 nA. The pipette was then removed. Fura-2 diffused to growth cones located up to 400 μm from the cell body in 10-20 minutes. The final intracellular concentration of fura-2 (mean, 390 ± 57 μM, n=19) was estimated using the method described in Section 2.3.6. Transmitted light (bright field) images of the growth cone were recorded to monitor behaviour during the experiment. Following observation for 10-30 minutes growth cone behaviour was classified into one of five defined states. The spatial distribution of growth cone $[Ca^{2+}]_i$ was measured using ratio imaging and correlated with behavioural state. Fluorescent images were taken only every 10 minutes because prolonged exposure to UV light was found to damage the cells.

2.5.2 Image analysis

Overall ratio (R) for a particular cell region was calculated as the average of pixels within that region, weighted by the total fluorescence intensity at each pixel. Values of growth cone R were calculated by averaging all those pixels of intensity greater than an arbitrary cut off (1/8 camera saturation) which lay distal to the neurite growth cone junction. In order to measure R in a specific localized region of the growth cone a circle was drawn around particular regions on the transmitted light image, a circle of the same position and radius was placed on the fura-2 ratio image and calculated the weighted average of R for pixels within the circle.

2.5.3 Control experiments

The presence of 2% DMSO in the differentiation and recording medium might distort calcium levels or calcium gradients. In the absence of DMSO, N1E-115 cells extend neurites in the first 2 days after plating on polylysine coated coverslips, but then pull in these neurites and re-enter the cell cycle. In order to test for an artifact due to DMSO $[Ca^{2+}]_i$ was measured within DMSO-free growth cones during this 2 day post-plating period.

The effect of introducing fura-2 into N1E-115 cells by the method of acetoxymethylester (AM) loading (Tsien, 1981) was investigated in order to compare results with previous findings. Cells were bathed in differentiation medium containing 20 μM fura-2 AM (Molecular Probes, Oregon) for 30 to 60 minutes. The medium was then changed to differentiation medium without fura-2 AM and the cells left for at least 90 minutes. The medium was then changed for HEPES-buffered DMEM, and $[Ca^{2+}]_i$ measured. For consistency with the experiments of Connor (1986) loading was performed at 36 °C.

2.6 Measurement of calcium currents in differentiated N1E-115 cells

2.6.1 Whole-cell patch-clamp recording

The whole-cell variant of the patch-clamp technique (Hamill *et al.*, 1981) was used to study L- and T-type calcium currents of N1E-115 neuroblastoma cells. Micropipettes for whole-cell recording were pulled on a Kopf 720 two-stage puller (David Kopf Instruments, California) from pyrex glass with a microfilament insertion (GC150TF10, Clark Electromedical). Micropipette resistance in recording medium was 0.5-5.0 MΩ.

To obtain a whole-cell recording, a patch pipette filled with the appropriate internal solution (Table 2.2) was brought close to the cell membrane, and gentle suction was applied to the pipette resulting in the formation of a high resistance seal (usually in the range 5 - 50 GΩ) between the pipette and the cell membrane. After formation of a high resistance cell-attached seal, 30-60 seconds was allowed for the intracellular solution to diffuse back into the tip of the electrode, then a further pulse of suction produced a low-resistance pathway into the cell. Over a subsequent period of about 1-2 minutes, potassium currents declined as caesium and TEA diffused out of the pipette and throughout the cell cytoplasm. The cell could then be voltage-clamped, with the current being measured as the voltage drop across the 500 MΩ resistor of a current-to-voltage converter (List Electronics, EPC-7). The indifferent electrode was either a Ag/AgCl pellet or a 150 mM NaCl agar salt bridge connected to a Ag/AgCl wire placed in the recording chamber.

The series resistance in the pathway from the patch pipette to the cell was measured from the current response to a hyperpolarizing voltage-clamp step (Fig. 2.10a). Series resistance was typically 3.5 MΩ, though values as low as 1.0 MΩ and as high as 10 MΩ were occasionally found. The series resistance sometimes changed during the experiment and was therefore monitored throughout the experiment. The maximum series resistance error occurred during the peak of the T-type current and was typically < 3 mV (750 pA through 3.5 MΩ). Series resistance compensation was not used during the experiment. When correction for voltage error was necessary (noted in the results) it was calculated from the peak current and known series resistance.

Since the pipette and the bath contained different solutions, a junction potential existed at the tip of the pipette when it was in the bath solution prior to forming a seal (Fenwick *et al.*, 1982). Junction potentials were measured by comparing the zero current voltage obtained when the pipette and bath contained intracellular medium, with that obtained when the bath solution was replaced by

Figure 2.10 Capacity transient analysis

Part a shows a typical current response to a 10 mV hyperpolarizing step from -50 mV. Time zero was defined as the start of the hyperpolarization. The patch electrode contained Solution A (Table 2.2) and the cell was bathed in Medium A (Table 2.3). The transient was fitted by a single exponential with a time constant τ = 0.33 ms (correlation coefficient r = 0.9997). The instantaneous current, I_0, was determined by extrapolation to t = 0 ms and was -3260 pA, the steady state current, I_∞, was -30pA. The series resistance, R_s = 3.1 MΩ, capacitance, C = 110 pF, and input resistance, R_{in} = 330 MΩ, was calculated using the method described in this section.

Part b shows an equivalent circuit for the cell. R_p represents the pipette series resistance, C the cell capacitance and R_{in} a parallel combination of the cell resistance and that of the seal between the patch pipette and the cell. The resting potential of the cell, which could have been represented in this circuit by a battery, is omitted for simplicity.

a,

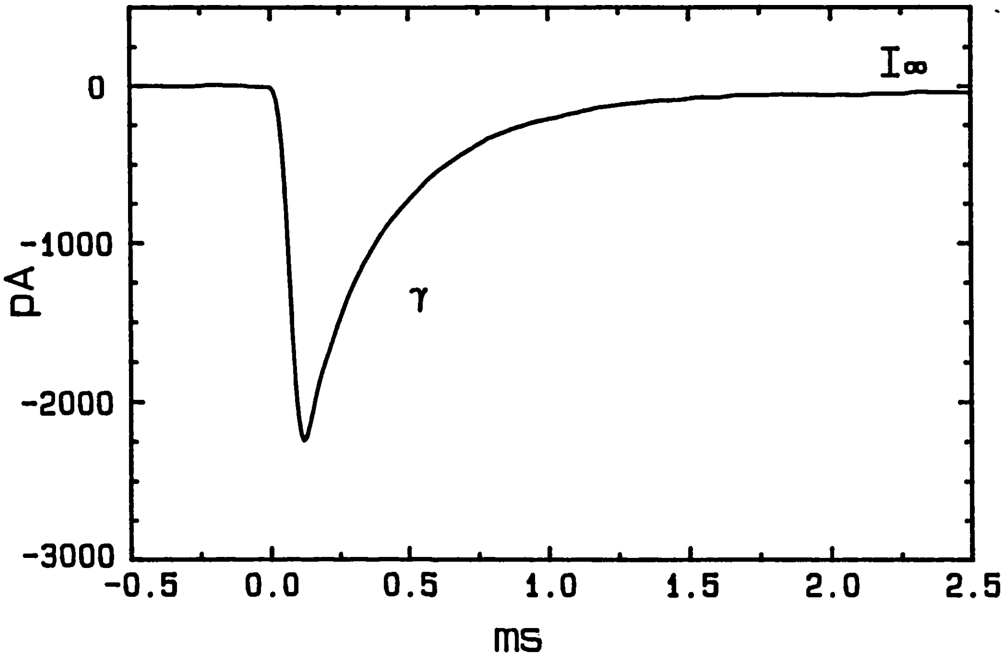

b,

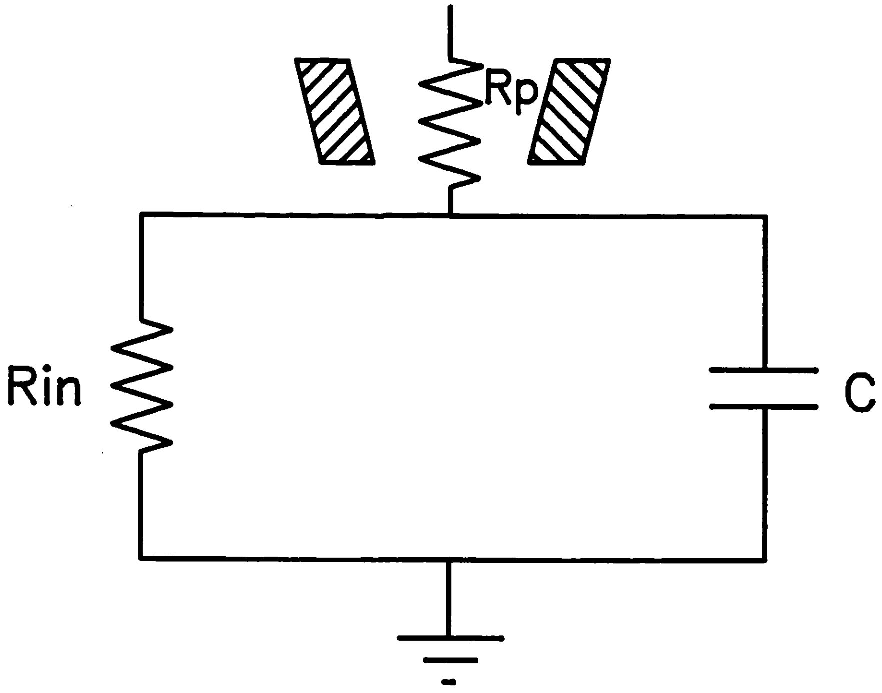

the extracellular medium used while forming a seal. The junction potentials measured for the different internal solutions were less than 1 mV and therefore ignored.

2.6.2 Measurement of capacitance and series resistance when whole-cell patch-clamping

The membrane capacitance, C, and series resistance of patch pipette, R_p, were measured from the current response to a 10 mV hyperpolarizing voltage-clamp step from a holding potential of -50 mV, where there is a minimal contribution from voltage-activated currents (Fig. 2.10a). The electrode and cell can be treated as the simple circuit shown in Fig. 2.10b. The time course of the change in current in response to a voltage clamp step for this circuit is predicted (Tessier-Lavigne *et al.*, 1988) to have the waveform:

$$I(t) = \frac{V}{R_{in} + R_p} \left(1 + \frac{R_{in} e^{-t/\tau}}{R_p}\right)$$

where t is the time after application of the voltage-clamp step, V is the amplitude of the step, and τ is the decay time constant of the transient:

$$\tau = C\, R_{in}\, R_p \,/\, (\, R_{in} + R_p \,)$$

Thus, the current amplitude at t=0 is :

$I_o = V / R_p$ allowing the calculation of R_p.

The steady state current is:

$I_\infty = V / (\, R_{in} + R_p \,)$ allowing calculation of R_{in}.

The membrane capacitance can then be calculated from the decay time constant of transient as:

$$C = \tau\, (\, R_{in} + R_p \,) \,/\, (\, R_{in}\, R_p \,)$$

This reduces to the more commonly quoted $C = \tau / R_p$ if the cell input resistance is very much larger than the pipette resistance. Figure 2.10a shows a typical capacity transient, used for these calculations, it was well fitted by a single exponential curve (τ = 0.3 ms), consistent with the simple model of Fig. 2.10b. Small deviations from the predicted exponential current decay were occasionally seen. In these cells the capacitance was also estimated by integrating the capacity transient and subtracting the resistive component to give charge movement (q). The capacitance of the cell was estimated from

$$C = q / V$$

This method agreed with the exponential analysis, to within 10%.

The membrane leak and reversal potential was estimated using a pulse protocol to -60, -50 and -40 mV from a holding level of -40 mV. The leak was subtracted from the currents to give the true amplitude of the calcium current.

2.6.3 Separation of T- and L-type calcium currents using two voltage protocols

N1E-115 mouse neuroblastoma cells express two types of calcium current (Bolsover, 1986; Narahashi *et al.*, 1987) similar to the T- and L-type calcium currents found in many neurons (Tsien *et al.*, 1988) although inactivation of the T-type current is slower than in other systems. Calcium currents could be measured when the potassium and sodium currents were blocked with 10 mM tetraethylammonium (TEA), 10 mM CsCl and 1 μM tetrodotoxin (TTX) in the extracellular medium (A, B Table 2.3) and CsCl and TEA in the internal medium (A, C Table 2.2). Using whole-cell patch-clamp of the cell soma, T- and L-type currents could be activated independently by the appropriate voltage protocol (Fig. 2.11a, b). T-type calcium currents were activated by depolarizing to -35 mV from a holding potential of -100 mV (Fig. 2.11c). L-type calcium currents were activated by a depolarizing to +10 mV from a holding potential of -40 mV (Fig. 2.11d). A clear separation of the two calcium currents was possible because the voltage dependence of activation and inactivation is different for the two currents (Fig. 2.12c).

Table 2.2

Patch pipette solutions

Constituents mM	Solution A	Solution B	Solution C
CsCl	135	–	140
KCl	–	130	–
NaCl	–	10	–
TEA	25	–	30
EGTA	10	10	–
HEPES	7.5	7.5	7.5
ATP	5	5	5
$CaCl_2$	1	1	–
$MgCl_2$	1	1	1
Fura–2	–	–	5
Leupeptin	0.1	0.1	0.1
pH	7.1	7.1	7.1
Free calcium	50nM	50nM	–

Osmolarity was checked and corrected for by addition of the major ion.

Table 2.3

External media

Constituents mM	Medium A	Medium B	Medium C
NaCl	120	120	120
KCl	5.5	5.5	5.5
$CaCl_2$	1.8	10	1.8
CsCl	10	10	–
$MgCl_2$	1	1	1
Glucose	25	25	25
TRIS	20	20	20
TEA	20	20	–
TTX	1×10^{-3}	1×10^{-3}	–

Osmolarity was checked and corrected using sucrose.

Figure 2.11 Voltage-clamp quality and voltage-dependence of calcium currents in differentiated N1E 115 cells

Voltage-clamp uniformity throughout the cell during activation of T- and L-type calcium currents by different voltage protocols applied through a patch pipette on the cell body. a: Voltage protocol used to activate a T-type current. b: Protocol used to activate an L-type current. c: T-type current recorded through the voltage-clamping pipette on the cell body. d: L-type current recorded through the voltage clamping pipette on the cell body. The the voltage-clamping patch pipette contained Solution A (Table 2.2) and the cells were bathed in Medium A (Table 2.3) at 20 °C. Currents are membrane-leak corrected. e, f: Membrane voltage at a growth cone 210 μm away from the cell body during depolarizing steps in respectively a and b that elicited currents in c and d. Growth cone membrane voltage was measured by whole-cell recording with a second patch pipette containing Solution B (table 2.2), connected to a high impendence amplifier. g shows the calcium current-voltage relation for two holding voltages, -100 mV (□) and,-40 mV (▼) measured 50 ms after the onset of depolarization.

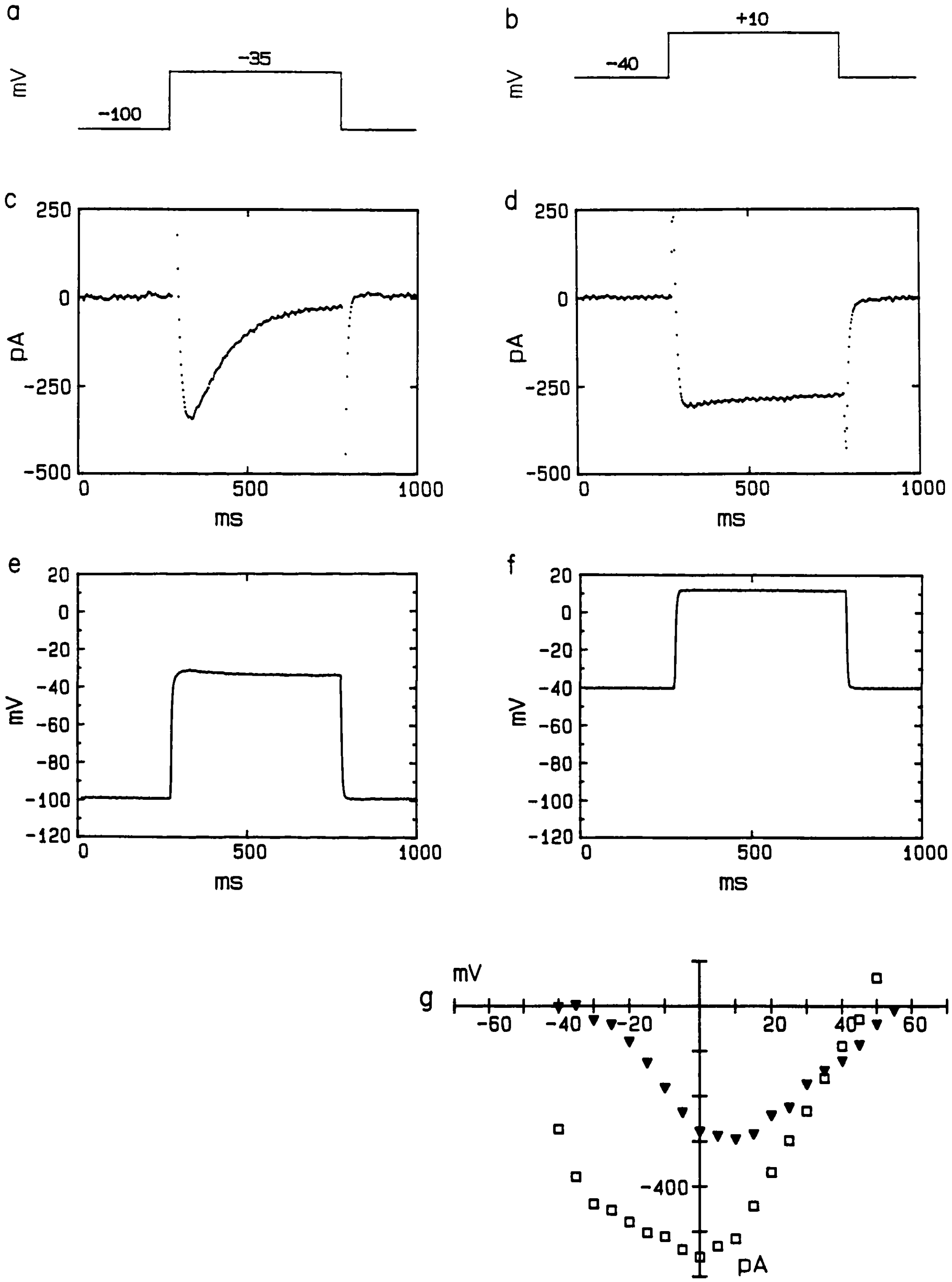
a
mV
-100
-35
b
mV
-40
+10
c
250
0
-250
-500
pA
0
500
1000
ms
d
250
0
-250
-500
pA
0
500
1000
ms
e
20
0
-20
-40
-60
-80
-100
-120
mV
0
500
1000
ms
f
20
0
-20
-40
-60
-80
-100
-120
mV
0
500
1000
ms
g
mV
-60
-40
-20
20
40
60
-400
pA

Figure 2.12 Inactivation of T-type and activation of L-type calcium currents

Inactivation of the T-type current was measured using the three-component voltage protocol shown in Part a. The conditioning pulse was initially at -100 mV and was increased by +5 mV for each of the subsequent 15 runs. The conditioning pulse was 1024 ms long (12 time consants) this produced a steady state level of inactivation. The membrane voltage was then stepped to -100 mV for 5 ms. This closed all the activation gates but the pulse was too brief to produce any significant recovery from inactivation (Matteson and Armstrong, 1986). This procedure ruled out any contamination from the activation gate as has been reported for the sodium current (Gillespie and Meves, 1980). In the final step of the voltage protocol, the T-type current was activated by stepping to -35 mV and measured 15 ms into the pulse. Part c shows the normalized peak current plotted against conditioning pulse voltage (+).

Part b shows the voltage protocol used to measure the voltage dependence of L-type current activation. The cell was held at -40 mV and stepped to a range of potentals from -50 mV to +25 mV. The L-type current was measured at 15 ms into the pulse. The conductance was calculated using $g = I/(V_{pulse}-V_{Ca})$ where g is the conductance, V_{pulse} is the activation pulse voltage and V_{Ca} is the reversal potential (measured as +48 mV, see Fig. 2.11g). The conductance was normalized and plotted against the pulse voltage (Part c, ■). Experiments were done on spherical cells (for fast voltage-clamp) bathed in Medium A (Table 2.3) at 32-36 °C, patch pipettes were filled with Solution A (Table 2.2). At -40 mV the T-type current is fully inactivated, so by holding at this potential the L-type current can be selectively activated. Since -35 mV is below the activation curve for the L-type current stepping to this value activates only the T-type current.

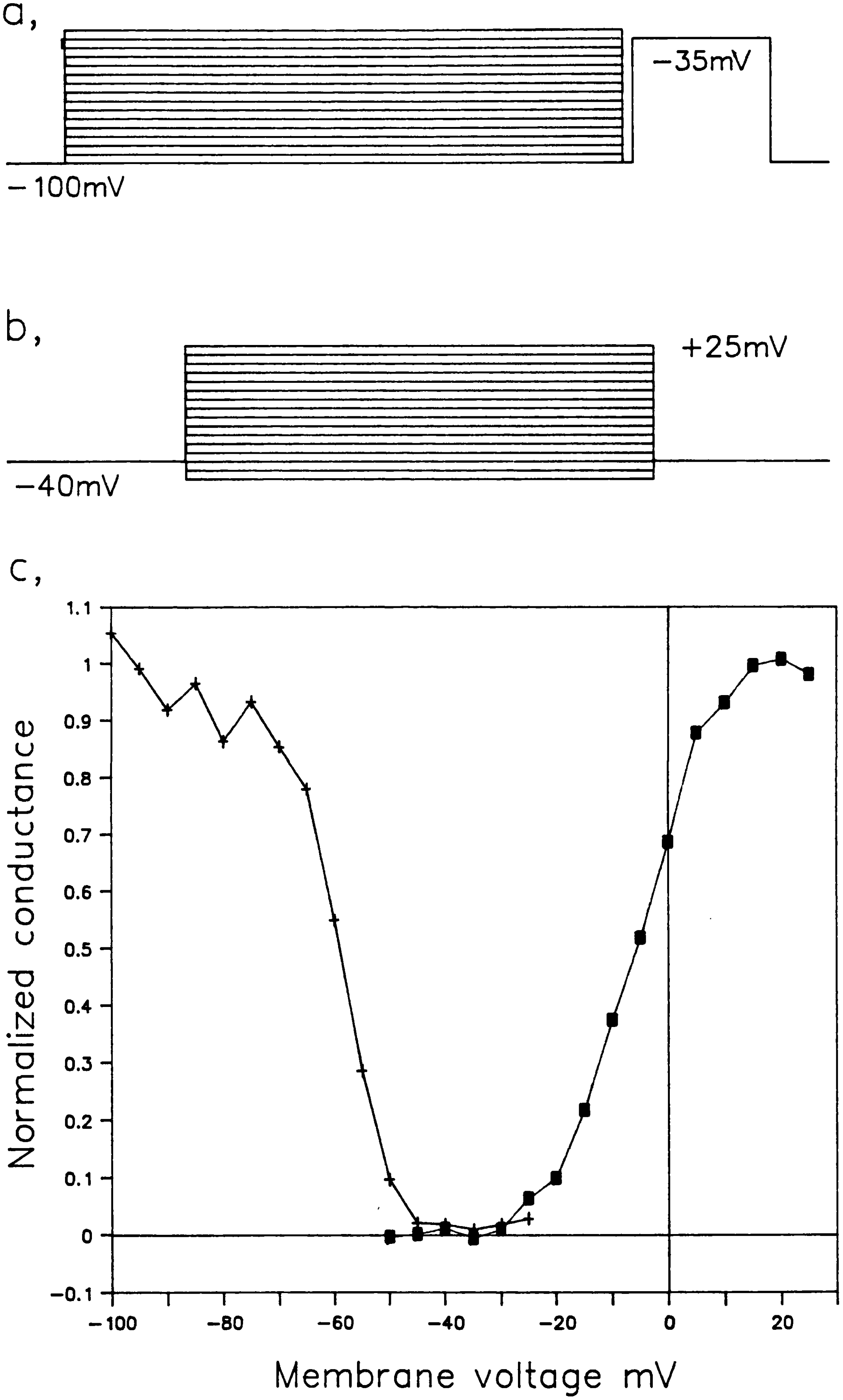
a,
−35mV
−100mV
b,
+25mV
−40mV
c,
1.1
1
0.9
0.8
0.7
0.6
0.5
0.4
0.3
0.2
0.1
0
−0.1
Normalized conductance
−100
−80
−60
−40
−20
0
20
Membrane voltage mV

2.6.4 Data acquisition and analysis

Membrane currents and voltages were acquired using a EP-7 patch-clamp amplifier (List Electronics, W. Germany) and computer operated pCLAMP programs (Axon Instruments Inc., California). The signals were filtered at 10000 Hz (EF5-02, Fern Developments), digitized (Labmaster board, Axon Instruments Inc.) and temporarily stored in coded files on a Del 286 computer hard disc (30 Mb). Data files were transferred to 1.6 Mb floppy discs for permanent storage.

Data were analysed using the pCLAMP analysis programs CLAMPFIT and CLAMPAN.

2.6.5 Voltage-clamp quality in differentiated N1E-115 cells

The non-spherical shape of differentiated N1E-115 cells raised the question of how uniform the electrical potential was in the dendrites during voltage-clamp applied at the soma. Construction of an accurate mathematical model to calculate the degree of voltage uniformity would have necessitated the use of some non-verified assumptions, including uniform membrane resistance, cytoplasmic resistance and simplified geometry.

To overcome these possible sources of error the voltage uniformity of differentiated N1E-115 cells was measured using a patch electrode (Fig. 2.11e,f). The patch electrode used to voltage-clamp the cell was filled with the normal CsCl intracellular solution (A, Table 2.2) and sealed cell-attached onto the soma membrane. A second, higher resistance electrode (2 - 5 MΩ), filled with a physiological medium (solution B, Table 2.2, to create the 'worst case' of intracellular perfusion of potassium channel blockers from the soma electrode) was then sealed onto growth cone or neurite of a cell with unbranched processes. Both electrodes were then 'sucked through' and 1-2 minutes was allowed for intracellular perfusion. The electrode at the soma was in a voltage-clamp mode, measuring membrane current while the electrode on the process was connected to a high impedence amplifier and recorded membrane voltage. In all the 7 cells examined, growth cones and neurites 270 µm or less from the cell body were voltage-clamped to within ± 2 mV of the soma pipette voltage within 13 ms of a change of holding voltage (Fig. 2.11e,f).

In order to ensure a uniform voltage-clamp, cells with branched dendrites were discarded from the study.

2.7 Simultaneous patch-clamp and single wavelength imaging

In order to investigate voltage-gated calcium influx into the growth cone, the whole-cell patch-clamp and single wavelength imaging techniques were applied simultaneously. Cells were bathed in Tris-buffered saline containing 1 µM TTX, 10 mM TEA and 10 mM CsCl (Medium B, Table 2.3) at 20 °C. The internal medium used to fill the tip of the patch pipettes had 5 mM fura-2 added to the backfill solution (Solution C, Table 2.2). The backfill solution contained no calcium buffer. Before the membrane patch was ruptured the background fluorescence of the growth cone was measured. After the patch was ruptured the cell was left for 5 to 20 minutes for the fura-2 to diffuse to the growth cone. The absolute resting level of $[Ca^{2+}]_i$ was measured at the holding potential using ratio imaging. The video acquisition and voltage-clamp protocol were triggered simultaneously and changes in the I_{380} signal and calcium current recorded.

2.8 Microelectrode and single wavelength recording

In order to examine the $[Ca^{2+}]_i$ changes at the growth cone under physiological conditions, a conventional microelectrode was used to pressure inject fura-2 (see Section 2.5.1) and electrically stimulate the cells by current injection (Fig. 5.3). The cells were bathed in a saline medium containing 1.8 mM calcium (Medium C, Table 2.3) and maintained at 32-36 °C. The behaviour of the growth cone was monitored by recording either 380 nm fluorescent images or bright field pictures for 5-15 minutes before and 4 minutes after electrical stimulation. Resting calcium was measured using ratio imaging. Changes in $[Ca^{2+}]_i$ from the resting level were measured using the single wavelength method during a train of five action potentials at 10 Hz. This was achieved by simultaneously triggering the video acquisition and current injection pulses.

2.9 Statistical treatment

Data is expressed as mean ± standard error of the mean. The significance of correlated data was tested using student's two tailed t-test and the χ^2-test (Snedecor and Cochran, 1976). Confidence limits for a proportion were calculated from the binomial distribution (Snedecor and Cochran, 1976).

Chapter 3

Correlation of calcium currents with morphological differentiation in N1E-115 cells

3.1 Calcium currents in N1E-115 neuroblastoma cells

N1E-115 neuroblastoma cells express two types of calcium current (Bolsover, 1986; Narahashi *et al.*, 1987), one transient and the other weakly-inactivating (Fig. 2.11c, d). Both currents were abolished by the addition of 10 mM $CoCl_2$ or the reduction of extracellular calcium to 100 μM. The two calcium currents could be activated independently by the appropriate voltage protocol (Fig. 2.11a, b). This is possible because the voltage dependence of activation and inactivation is different in the two currents (Fig. 2.12). The transient current had many of the properties of the T-type current described in chick sensory neurones by Nowycky *et al.*, (1985). The current was completely inactivated at a holding voltage of -40 mV (Fig 2.12), but could be activated from more negative holding voltages by depolarization to -35 mV (Fig. 2.11). The rate of inactivation of the current was slower than in other systems (Tsien *et al.*, 1988). At the -35 mV inactivation kinetics were: $\tau=51\pm4$ ms, n=49, at 34-36 °C in 1.8 mM extracellular Ca^{2+} and $\tau= 83\pm7$ ms, n=23, at 20 °C in 10 mM extracellular Ca^{2+}. The current was insensitive both to 70 μM $CdCl_2$ (Fig. 5.2) (peak current in 70 μM $CdCl_2$ = 105±5%, of control value, n=4) and to the dihydropyridine agonist, BAY K8644 (peak current in 1 μM BAY K8644 = 91±5% of control, n=5).

The weakly-inactivating current was similar to the L-type calcium current described in many systems (Tsien *et al.*, 1988). The current could be activated from the relatively depolarized voltage of -40 mV; maximal current activation was observed during depolarizing to +10 mV (Fig. 2.11d, g). This high threshold current was sensitive to 70 μM $CdCl_2$ (Fig 5.2) (peak current in 70 μM $CdCl_2$ was 28±5% of control, n=8) and to BAY K8644 (peak current in 1 μM BAY K8644 = 170±14% of control, n=8). The current inactivated at a variable rate with a time constant between $\tau=\infty$ and $\tau=200$ ms (usually >500 ms). All these characteristics indicate that the current was of the L-type.

3.2 L-type current washout

In many cells including N1E-115, the size of the L-type current declines during whole-cell patch clamping experiments. This phenomenon, called 'washout' is thought to occur as a result of the loss of cytosolic components up the patch pipette and subsequent proteolytic action on the channel (Chad and Eckert, 1986). Leupeptin, a proteolytic enzyme inhibitor, was included in the pipette solutions to minimize washout. Since the soma will lose components to the patch pipette first, washout would be expected to be fastest in the soma, artificially producing lower current readings in cells without neurites. In cells without neurites, L-type currents declined to 84±3%, n=8, in 1.5 minutes, 71±6%, n=8, in 3 minutes and 56±6%, n=7, in 5 minutes after going whole-cell (1.8 mM extracellular Ca^{2+}, 32-36 °C). All the measurements presented in this chapter were taken within 3 minutes of the onset of whole-cell recording. L-type currents in cells without processes will therefore be underestimated by no more than 29%.

3.3 Correlation of calcium currents with morphology

3.3.1 The T-type current

During the period 2 to 7 days after plating, cultures in medium containing the differentiating agent, included cells with and without neurites. The fraction of cells that did not have neurites declined with time (Fig. 3.1). Two groups, cells with and cells without neurites, were studied (in 1.8 mM extracellular Ca^{2+} at 32-

Figure 3.1 The fraction of cells without neurites as a function of time in the differentiation medium

Cells were grown in DMEM + 2% DMSO on polylysine coated coverslips. Each point represents one plate of cells fixed with Dulbecco's phosphate-buffered saline containing 3.5% formaldehyde at the indicated time after addition of DMSO to the growth medium. All the cells within a defined area were counted and the fraction with neurites was plotted as a function of time in the differentiation medium. The number of cells counted for each point from left to right was 118, 128, 119, 118, 125 and 141. The error bars indicate the 95% confidence limits (Snedecor and Cochran, 1976). The graph shows that the fraction of cells with neurites increases with time. The trend towards a value of 1, suggests that all cells in the population would eventually express neurites.

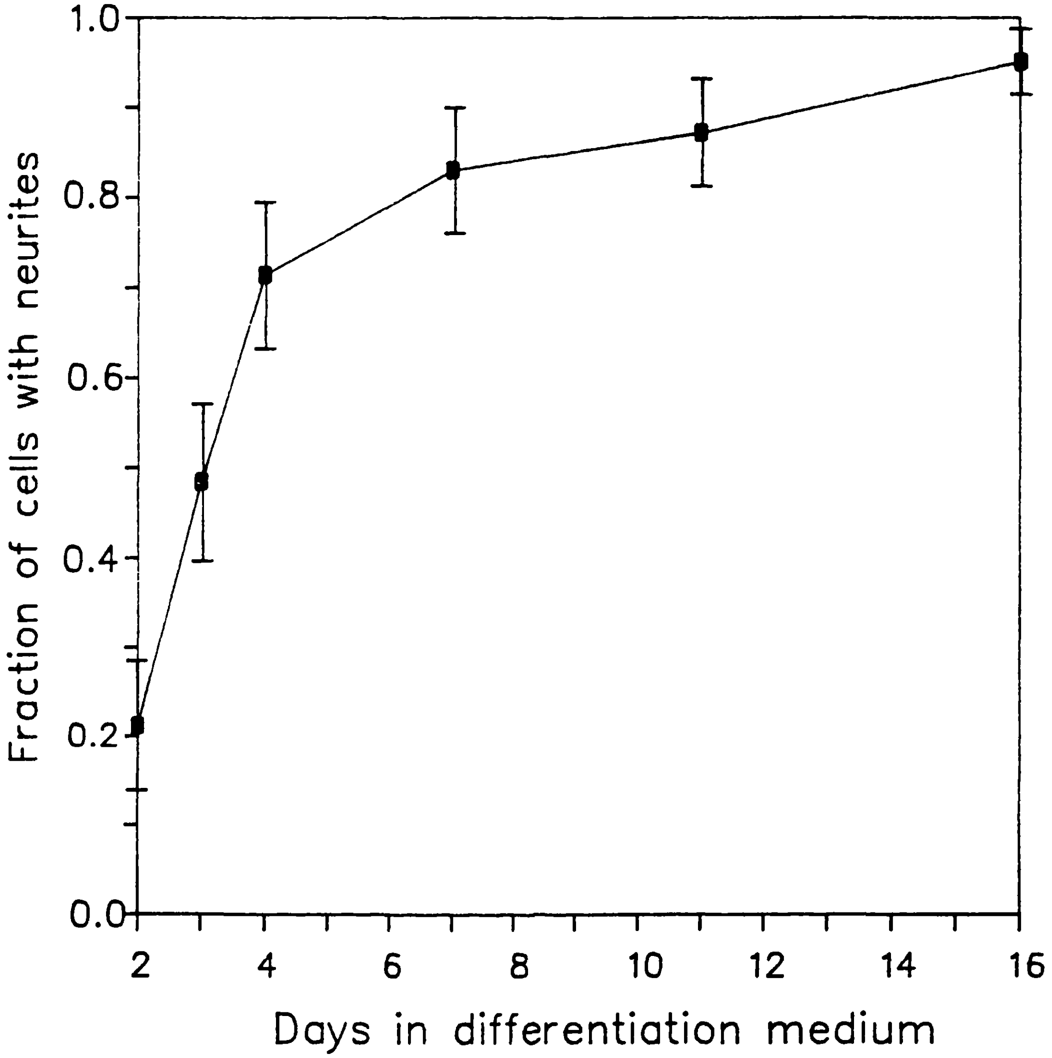

1.0
0.8
0.6
0.4
0.2
0.0
Fraction of cells with neurites
2
4
6
8
10
12
14
16
Days in differentiation medium

36 °C). Each of the 38 neurite bearing cells showed a significant T-type current (Fig. 3.2). In contrast 6 of the 46 cells without neurites had zero T-type current (Fig. 3.2). The difference between the two groups was significant ($p<0.05$, χ^2 test). In 40 cells without neurites that did show T-type currents, the current density was significantly smaller than the current density seen in cells with neurites (Figure legend 3.2). One interpretation of these results is that the cultures contained two distinct populations of cells. One differentiation-potent population expresses T-type channels at all times and extends neurites over a 7 day period in differentiating medium. Another, differentiation-impotent population never expresses T-type channels and cannot extend processes. Two pieces of evidence argue against this hypothesis. First, the increase with time of the fraction of cells bearing neurites tends to an asymptote of 1 (Fig. 3.1). This is inconsistent with the presence of a subpopulation of cells. Second, if the culture contained a differentiating-impotent population that neither expressed T-type currents nor extended neurites the population without neurites would become enriched in cells that did not show T-type currents. However, no enrichment was observed.

3.3.2 The L-type current

The relationship between cell differentiation and expression of the L-type current (in 1.8 mM extracellular Ca^{2+} at 32-36 °C) showed a similar but not identical pattern to the T-type current. All but 2 of the 45 neurite-bearing cells had L-type currents, while 11 of the 52 cells without neurites had no L-type current ($p<0.05$, χ^2 test). However, unlike the situation with T-type currents, those cells without processes that did express L-type currents did so at the same density as those with processes (Figure legend 3.2). Faster washout of L-current in cells without neurites may have caused the current to be underestimated by up to 29%, thus the true current density in these cells might have been 1193±148

Figure 3.2 Peak T- and L-type calcium current density as a function of total neurite length

Part a shows the relationship between peak T-type current density and total neurite length. All cells with neurites possessed a T-type current. Six cells without neurites had no T-type calcium current. When the six cells without neurites and T-type currents (at the origin) were eliminated, cells without neurites showed a lower T-type current density than cells with neurites (cells without neurites but with T-type currents, 1480±120 pA/nF, n=40; cells with neurites, 1920±150 pA/nF, n=38, t test, $p<0.05$); however, for cells with processes there was no dependence of current density on neurite length.

Part b shows the relationship between peak L-type current density and total neurite length. Two cells with neurites had no L-type current. When cells without L-type currents were eliminated, cells without neurites showed the same L-type current density as cells with neurites (cells without processes but with L-type currents, 847±105 pA/nF, n=41; cells with processes and L-type currents, 1010±97 pA/nF, n=43). Currents were measured in medium A, (table 2.2) with patch pipettes containing solution A, table 2.2 at 36 °C

a,

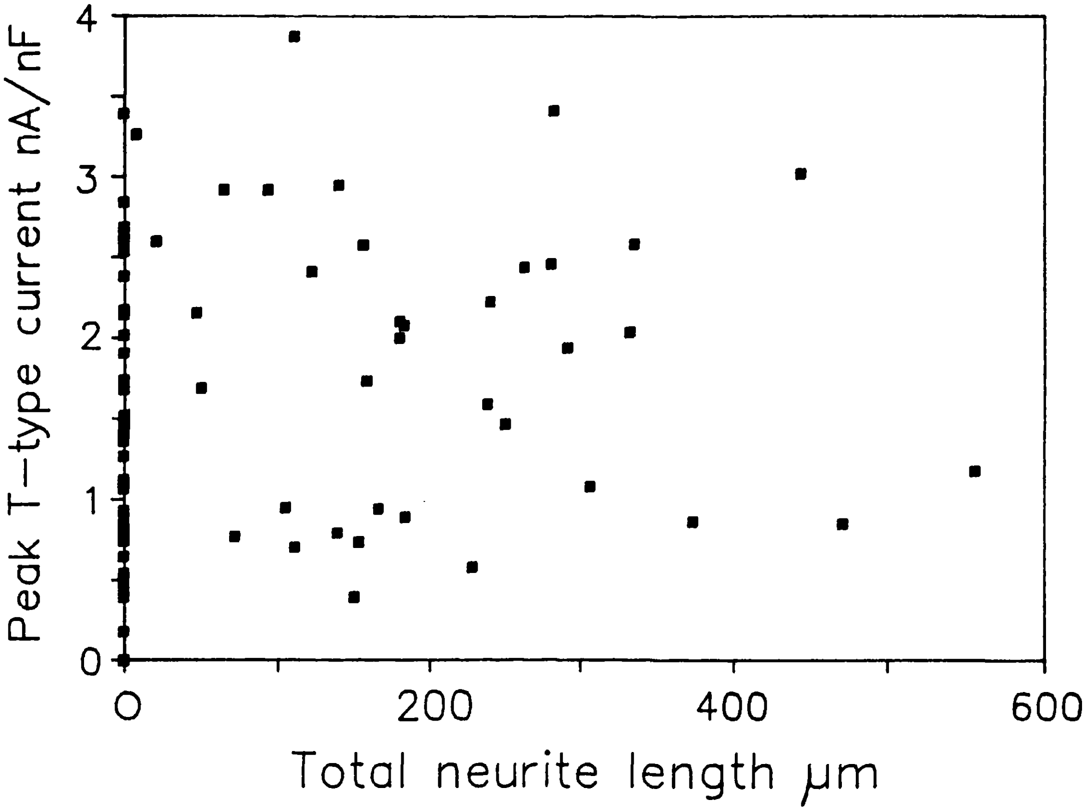
Peak T–type current nA/nF
0
1
2
3
4
0
200
400
600
Total neurite length µm

b,

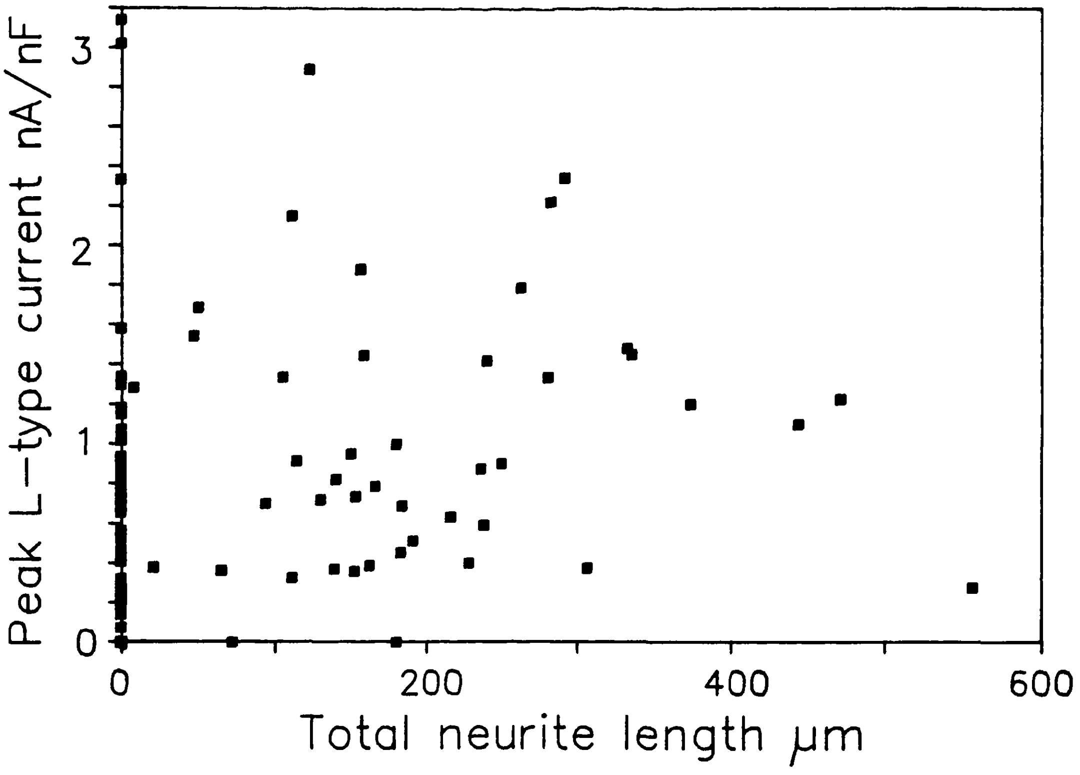
Peak L–type current nA/nF
0
1
2
3
0
200
400
600
Total neurite length µm

pA/nF, n=41. This value is not significantly different from the density in cells with processes. Within the population of cells with neurites, there was no correlation of T- or L-type current density with either total neurite length (Fig 3.2) or time in differentiation medium.

Other characteristics were monitored during differentiation (the voltage-clamp data in this section were corrected for series resistance). The inactivation kinetics and current activation curves were measured for T- and L- currents and the steady state inactivation (h_∞) half voltage was measured for the T-type current. There was no observed shift in any of these characteristics with time in the differentiation medium or with total neurite length.

3.4 Differentiation induced by dibutyryl cyclic AMP

As an alternative to DMSO, N1E-115 cells were induced to extend neurites by addition of 0.5 mM dibutyryladenosine 3'5'-cyclic monophosphate (dBcAMP) to the growth medium (Chalazonitis and Greene, 1974). Cells with neurites which had been differentiated in the presence of 0.5 mM dBcAMP were compared with those differentiated in 2% DMSO. Current densities of both the T- and L-type currents were the same in the two populations measured in 10 mM extracellular Ca^{2+} at 20°C (T-type current density, dBcAMP: 2.5±0.3 nA/nF, n=7; DMSO: 2.8±0.4 nA/nF, n=4. L-type current density, dBcAMP: 870±30 pA/nF, n=7; DMSO: 880±120 pA/nF, n=4).

3.5 Discussion of the results: Calcium currents and morphological differentiation

Mouse neuroblastoma cells can be induced to differentiate using a variety of agents (Spector, 1981). The sequence of maturation that they follow is very similar to that seen in neurones *in vivo* (Spitzer, 1979). The two calcium currents present in N1E-115 cells (Narahashi *et al.*, 1987) were examined under voltage-clamped conditions and correlated with neurite length and time in the differentiation medium.

3.5.1 T-type currents

All cells that possessed neurites also had a T-type calcium current. This suggests a model in which each N1E-115 cell exposed to the differentiation medium leaves the cell cycle (Kimhi *et al.*, 1976) and waits for a random event. When this event occurs the cell first expresses T-type channels and then extends neurites. In cells without neurites that did posess a T-current, the current density was lower than in cells without neurites. After neurite extension has started channel density remains constant. The data are compatible with the hypothesis that expression of T-type channels at a certain critical density is necessary for neurite outgrowth. A different hypothesis is that the correlation is not causal, it is possible that the genes coding for the T-channel, and the unrelated genes whose expression initiates neurite outgrowth, share a common control mechanism and are always expressed together. Once the T-type current appeared characteristics such as the inactivation rate, peak current voltage and the h_∞ half voltage did not change.

3.5.2 L-type currents

Two cells had neurites but no L-type currents. This result would appear to rule out an absolute requirement for L-type channels before neurite extension can proceed. However, given the lability of L-type currents (Chad and Eckert, 1986) it is possible that these two cells were damaged and the currents were washed out. Unlike the T-type current, the L-type current density was similar in cells with and without neurites. This finding is still valid even if the L-type current magnitude is corrected for washout. Thus, once expressed, the L-type channel density remained constant as the cells increased in size and extended neurites.

3.5.3 Agent used to differentiate cells

Current densities of both T- and L-type currents were identical in cells induced to differentiate with either dBcAMP (Chalazonitis and Greene, 1974) or DMSO. Addition of DMSO reduces cAMP levels in N1E-115 cells (Kimhi *et al.*, 1976), therefore its differentiating action cannot be cAMP-mediated. The similarity of the calcium current densities in cells induced to differentiate by the two agents implies that very similar differentiation pathways are activated by both agents.

Chapter 4

Correlation of neuronal growth cone behaviour with cytosolic calcium concentration

The experiments discribed in this chapter were done on unstimulated cells growing in growth medium at 36 °C. Neurite outgrowth and growth cone behaviour was observed for long periods under conditions in which there were no external stimuli. The calcium measurements in this chapter were made at a low time resolution (3 s) and therefore indicate the steady state calcium distribution.

4.1 Growth cone behavioural states

Growth cone varied widely in size (from less than 10 μm to greater than 100 μm in width), structural complexity and rate of change of morphology. Nevertheless it was possible to define five behavioural states into which most growth cones could be unequivocally sorted. The criteria defining each state were as follows:

(1) **Quiescent** growth cones showed no movement, either of the whole growth cone or of structures on the growth cone.

(2) **Motile advancing** growth cones showed both movement of structures upon the growth cone and forward movement of the neurite/growth cone boundary.

(3) **Motile non-advancing** growth cones showed movement of structures upon the growth cone, but no forward movement of the neurite/growth cone boundary.

(4) **Flattening** growth cones became very thin and usually expanded in area, without forward movement of the neurite/growth cone boundary.

(5) **Retracting** growth cones showed a withdrawal of motile structures into the growth cone followed by a withdrawal of the growth cone towards the cell body.

This classification differs from that used by Cohan *et al.*, (1987) in two ways. Motile growth cones were subdivided into motile-advancing and motile non-advancing, and a new category, flattening, was created. Anglister *et al.* (1982) have described behaviour similar to flattening, but have not defined it as a specific behavioural category.

4.2 Measurement of $[Ca^{2+}]_i$ in neuronal growth cones

4.2.1 Injection of fura-2 does not distort $[Ca^{2+}]_i$

Relatively high concentrations of fura-2 were injected into the cells to achieve a growth cone fluorescence image of sufficient intensity for the camera to detect. The concentration of fura-2 in the cell body (the site of injection) ranged from 105 μM to 1037 μM in the 19 cells in which it was measured. Fura-2 is a high-affinity calcium chelator, thus the injection of fura-2 might be expected to buffer and, therefore, reduce $[Ca^{2+}]_i$, with the greatest reduction of $[Ca^{2+}]_i$ occuring in those cells with the highest intracellular concentration of fura-2. This was not the case since cell body ratio values (mean = 1.46 ± 0.04, $[Ca^{2+}]_i$ = 88 ± 7 nM) showed no statistical correlation with fura-2 concentration (Bulmer, 1967) (correlation coefficient = -0.10). This implies that injection of fura-2 up to these concentrations does not disrupt the cell's ability to regulate $[Ca^{2+}]_i$. A similar result was observed in mouse thymocytes when quin-2 (another calcium indicator) was loaded to various concentrations (Tsien *et al.*, 1982). The authors suggested that $[Ca^{2+}]_i$ is maintained at a certain level by the plasma membrane which allows nett entry of Ca^{2+} during dye loading. Added calcium buffer would however reduce any calcium elevation above this level.

The effect of fura-2 on growth cone behaviour was tested by correlating the amount of fura-2 injected and the distribution of growth cones among the 5 behavioural states. (χ^2 test on a 2 x 5 contingency table, with growth cones divided into the 12 with highest [fura-2], and the 12 with the lowest [fura-2], gave $p > 0.05$). This result implies that the increased calcium buffering caused by fura-2 had no effect on the growth cone behaviour.

4.2.2 Quiescent growth cones

The defining feature of quiescent growth cones was that their appearance did not change over many minutes. Figure 4.1 illustrates a quiescent growth cone. The growth cone consisted of a rounded portion plus a flattened lobe (L). The neurite (N) ran to the cell body, which was out of the field of view. Twenty-seven minutes later (Fig 4.1C) the position and appearance of the growth cone had not changed. Figure 4.1B is a fura-2 ratio image, acquired 15 seconds before Figure 4.1C. Colours correspond to R values, and hence to $[Ca^{2+}]_i$, as indicated in the scale at the left, which applies to all the fura-2 ratio images in this chapter. Low values of R and $[Ca^{2+}]_i$ are represented by a blue colour. Higher values of $[Ca^{2+}]_i$ appear respectively as green, then yellow, with the highest values represented as red. The image in Figure 4.1B is mainly blue, indicating a low value of $[Ca^{2+}]_i$. This result was obtained consistently: in eight quiescent growth cones mean R was 1.29 ± 0.04, $[Ca^{2+}]_i = 55 \pm 7$ nM (Fig. 4.9).

4.2.3 Motile advancing growth cones

Motile growth cone changed their appearance over the course of minutes as filopodia, veils or ruffles were extended, moved and retracted. In addition, a subset of motile growth cones showed advancement of the neurite/growth cone boundary at an average of 0.23 ± 0.06 μm/min (n=7). Figure 4.2 illustrates one such motile-advancing growth cone. Over 16 minutes the growth cone changed shape dramatically as filopodia and membrane veils were extended. Both the

Figure 4.1 Fura-2 ratio imaging of a quiescent growth cone

Part A shows a bright field image of a growth cone. The time at which this image was acquired was defined as t = 0. N: neurite, L: lamellipodium. The five red arrowheads are placed in the same position in A and C and indicate dirt particles on the cover-slip that were used when repositioning the image to correct for cover-slip movement. The broad dark regions that have changed position between images A and C are bubbles in the liquid paraffin layer.

Part B, a fura-2 ratio image of the growth cone acquired at t = 27 min. The colours correspond to R values and therefore $[Ca^{2+}]i$ (Ca^{++}) according to the scale on the spectrum at the left. This scale applies to all the ratio images in this chapter. The image appears black where the fluorescent signal was below an arbitrary threshold (1/8th of the camera saturation value). Fluorescence from the thin, narrow neurite was less than this threshold, so that the neurite does not appear in the fura-2 ratio image. The image is mainly blue, indicating a low $[Ca^{2+}]_i$ (overall R=1.32, $[Ca^{2+}]_i$=61 nM). Part C shows a bright field image acquired 15 seconds after image B. Neither the position nor the appearance of the growth cone had changed relative to image A, the growth cone was therefore quiescent. Quiescent growth cones are often rounded and relatively thick, so that the ratio image in B is broadened because of fluorescence from out-of-focus regions of the growth cone. This phenomenon is not observed in other images in this chapter because the growth cones are thinner.

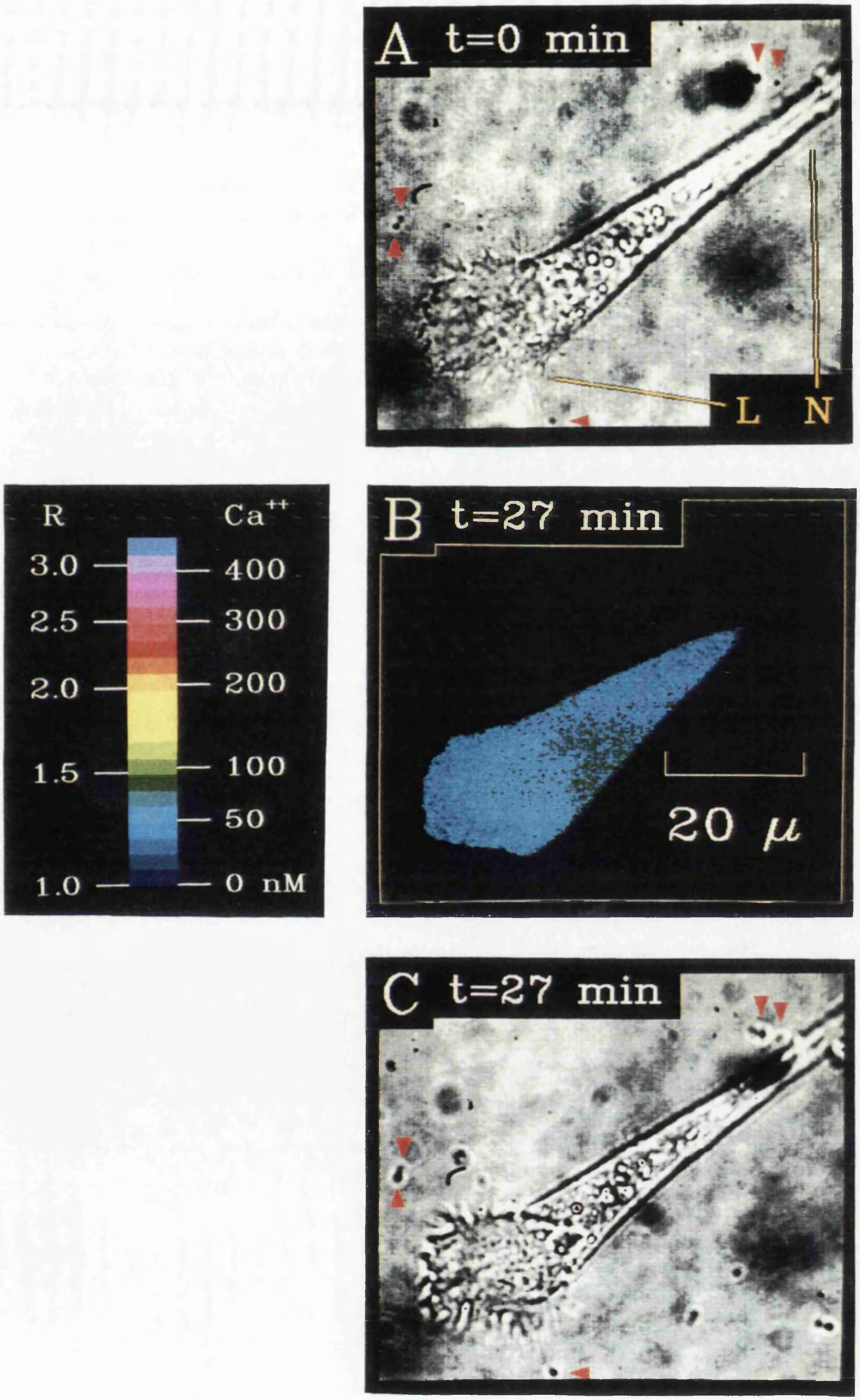
A t=0 min
L
N
R
Ca++
3.0
2.5
2.0
1.5
1.0
400
300
200
100
50
0 nM
B t=27 min
20 μ
C t=27 min

Figure 4.2 Fura-2 ratio imaging of a motile advancing growth cone

Part A shows a bright field image of the growth cone. The time at which this image was acquired was defined as t=0. The growth cone consists of a central region (C) bearing numerous filopodia (F). At the leading edge of the growth cone there are two thin veils (V1, V2). B1 indicates the neurite/growth cone boundary. Part B shows the growth cone 6 minutes later. The lower veil, V2 in A, has been retracted. One filopodium has extended dramatically to become a leading filopodium (LF), and a new, thin, featureless veil (NV) is forming at its base. The white cursors indicate the corners of the area shown enlarged as an insert in C. Part C shows a fura-2 ratio image acquired 32 s after image B. The ratio image is mainly blue indicating a low $[Ca^{2+}]_i$ (overall R=1.36, $[Ca^{2+}]_i$=68 nM). The position of the yellow lines is the same in images B, C and D. Part D shows the growth cone 16 minutes after the acquisition of A. The leading filopodium has advanced further, while the veil NV has broadened. The older veil V1 has lost its thin featureless appearance, probably because organelles have moved in from the central region of the growth cone (Goldberg and Burmeister, 1986). In the 16 minutes between the time of acquisition of images A and D the growth cone/neurite boundary has advanced 7 µm from B1 to B2, the growth cone is therefore in the motile advancing behavioural state. The insert in Part C shows a close up of the area within the white box in B. Calcium is resolved within the spreading new veil at the base of the filopodium. No spatial gradients of $[Ca^{2+}]_i$ are seen. Mean R for the insert is 1.36, equal to mean R for the entire growth cone.

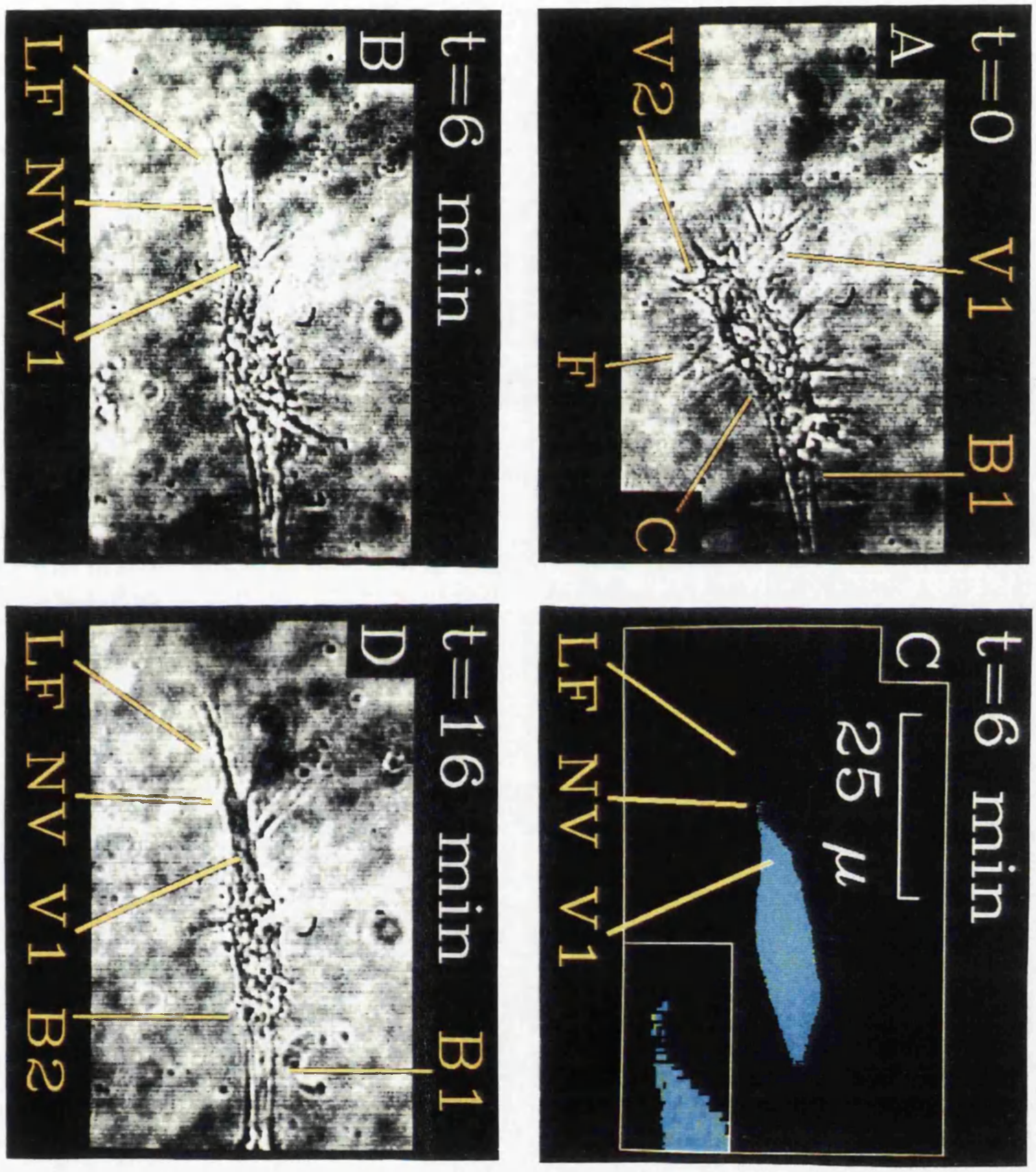

t=0
A
V1
B1
V2
F
C
t=6 min
B
LF
NV
V1
t=6 min
C
25 μ
LF
NV
V1
t=16 min
D
B1
LF
NV
V1
B2

leading edge and the neurite/growth cone junction advanced (from B1 in Fig. 4.2A to B2 in Fig. 4.2D). The fura-2 ratio image (Fig. 4.2C) was mainly blue, indicating a low $[Ca^{2+}]_i$. This result was obtained consistently: in seven motile advancing growth cones mean R was 1.32±0.03, $[Ca^{2+}]_i$ = 60±5 nM; that is $[Ca^{2+}]_i$ was not significantly different in quiescent and truly growing growth cones.

4.2.4 Motile non-advancing growth cones

Many growth cones exhibited motile behaviour such as extension of filopodia and membrane veils and movement of ruffles, without net advancement of the neurite/growth cone boundary. Figure 4.3 illustrates one such motile non-advancing growth cone. In the 41 minutes between the acquisition of images 4.3A and 4.3B, the appearance of the growth cone changed principally through movement of two highly motile ruffles (R). However, the boundary between the neurite and the growth cone (indicated by line B) did not advance during this period.

The growth cones illustrated in Figures 4.2 and 4.3 show the range of morphology that motile growth cones exhibited, from thin and filopodial to broad and ruffling. Advancement of the neurite/growth cone junction was not restricted to growth cones of any particular type of morphology: it was impossible to predict from the appearance of a motile growth cone whether that growth cone would show advancement of the neurite/growth cone boundary. Fura-2 ratio images were, in contrast, accurate indicators of whether a growth cone would advance. The fura-2 ratio image in Figure 4.3C appeared mainly green, indicating a higher $[Ca^{2+}]_i$ than in the motile advancing growth cone of Figure 4.2C. This result was obtained consistently: in twenty motile, non-advancing growth cones mean R was 1.50±0.02, $[Ca^{2+}]_i$ = 94±4 nM, very significantly higher ($p<0.001$) than in motile advancing growth cones (Fig. 4.9).

Figure 4.3 Fura-2 ratio imaging of a motile non-advancing growth cone

Part A shows a bright field image of the growth cone. The time at which this image was taken was defined as t=0, R indicates ruffles on the growth cone, B indicates the boundary between the neurite and growth cone. Part B shows a bright field image 41 minutes after image A. The appearance of the ruffles (R) has changed, indicating that they are motile. However during this period the growth cone/neurite boundary has remained static at B. The growth cone is therefore showing motile non-advancing behaviour. Panel C shows a fura-2 ratio image acquired 36 s after image B. Overall R=1.51, $[Ca^{2+}]_i$=97 nM. $[Ca^{2+}]_i$ is lower in local regions around the two ruffles, being 76 and 61 nM, in the upper and lower ruffles respectively.

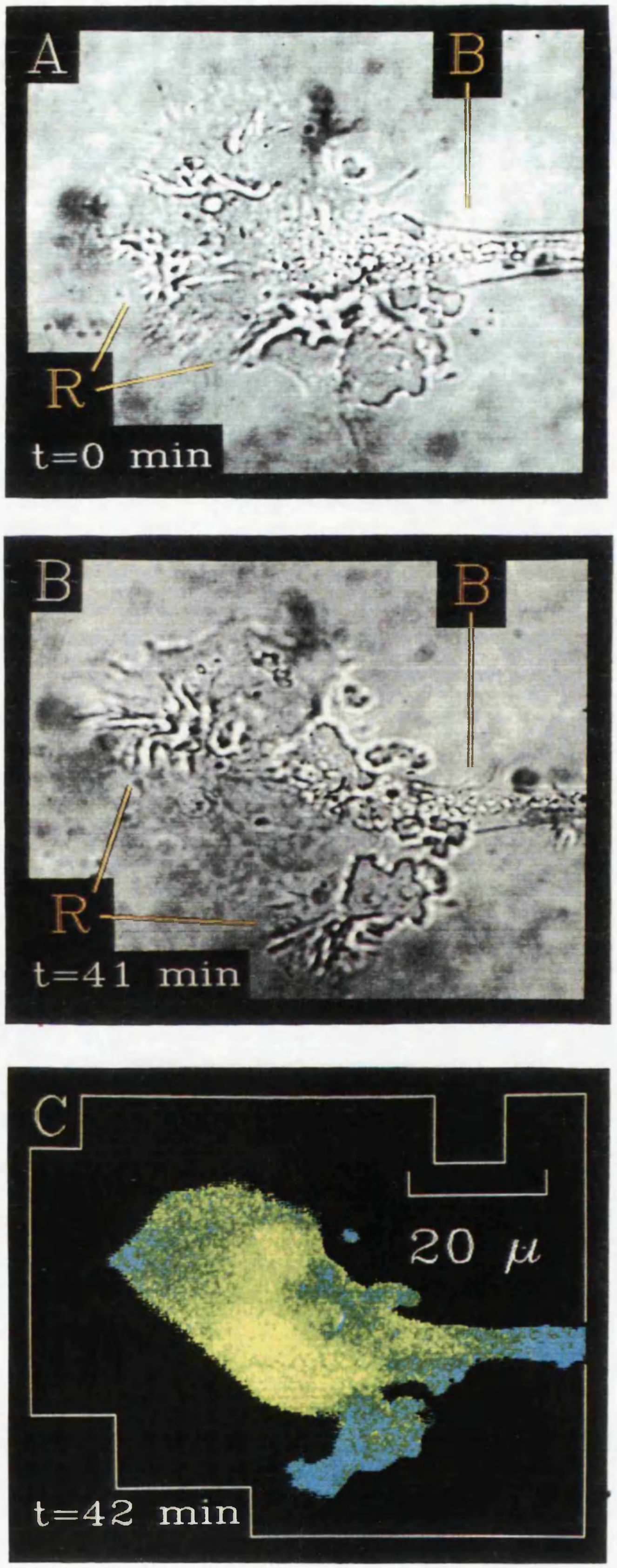
A
B
R
t=0 min
B
B
R
t=41 min
C
20 μ
t=42 min

4.2.5 Flattening growth cones

Motile growth cones occasionally displayed a sequence of behaviour that involved the growth cone decreasing in thickness and increasing in area. During this flattening behaviour the growth cone became difficult to visualize, presumably because of its thinness. The growth cone thickness approximately halved during flattening. This was estimated by focusing on the top and bottom of the growth cone during bright field observation, before and after flattening, and from the fall in fluorescence intensity per unit area of the growth cone during flattening. Filopodia were sometimes extended during flattening. Figure 4.4 illustrates a typical flattening growth cone. In the 21 minutes between the acquisition of Figures 4.4A and 4.4B the main body of the growth cone became wider, and the edges became less distinct. The growth cone also extended filopodia (F) and a veil (V). In the following 41 minutes, the area of the growth cone continued to increase (Fig. 4.4D). However the boundary (B) between the neurite and the growth cone did not advance during the entire 62 minute period. Figure 4.4C is a ratio image acquired 32 seconds before Figure 4.4D. The image was yellow, indicating a higher $[Ca^{2+}]_i$ than was seen in motile growth cones. This result was found consistently: R in flattened growth cones was 1.66 ± 0.05, n=9, $[Ca^{2+}]_i = 127 \pm 10$ nM, very significantly higher than in motile non-advancing growth cones ($p<0.005$) (Fig. 4.9). Flattened growth cones were not stable. The subsequent fate of seven of the nine growth cones was observed. In 6 $[Ca^{2+}]_i$ remained high, and the growth cones began retracting (see below). In the remaining growth cone $[Ca^{2+}]_i$ fell and the growth cone resumed motility.

4.2.6 Retracting growth cones

Growth cones sometimes showed a sequence of behaviour in which motility ceased and the growth cone retracted, often via an intermediate flattening stage. Retraction occurred in two phases. In the first phase, motile structures (ruffles,

Figure 4.4 Fura-2 ratio imaging of a flattening growth cone

Panel A shows a bright field image of the growth cone. The time at which the image was acquired was defined as t=0, line B indicates the position of the growth cone/neurite junction. Panel B shows the growth cone 21 minutes after image A was taken. New, long filopodia (F) have been extended during this period. A veil (V) has extended forwards over pre-existing filopodia, whose ends protrude from the edge of the veil. Panel C shows a fura-2 ratio image acquired at t=62 minutes. Overall R=1.66, $[Ca^{2+}]_i$ = 127 nM. Panel D shows a bright field image acquired 32 s after image C showing further flattening compared with image B. The growth cone/neurite junction (B) remained in the same position during the 62 minute observation period.

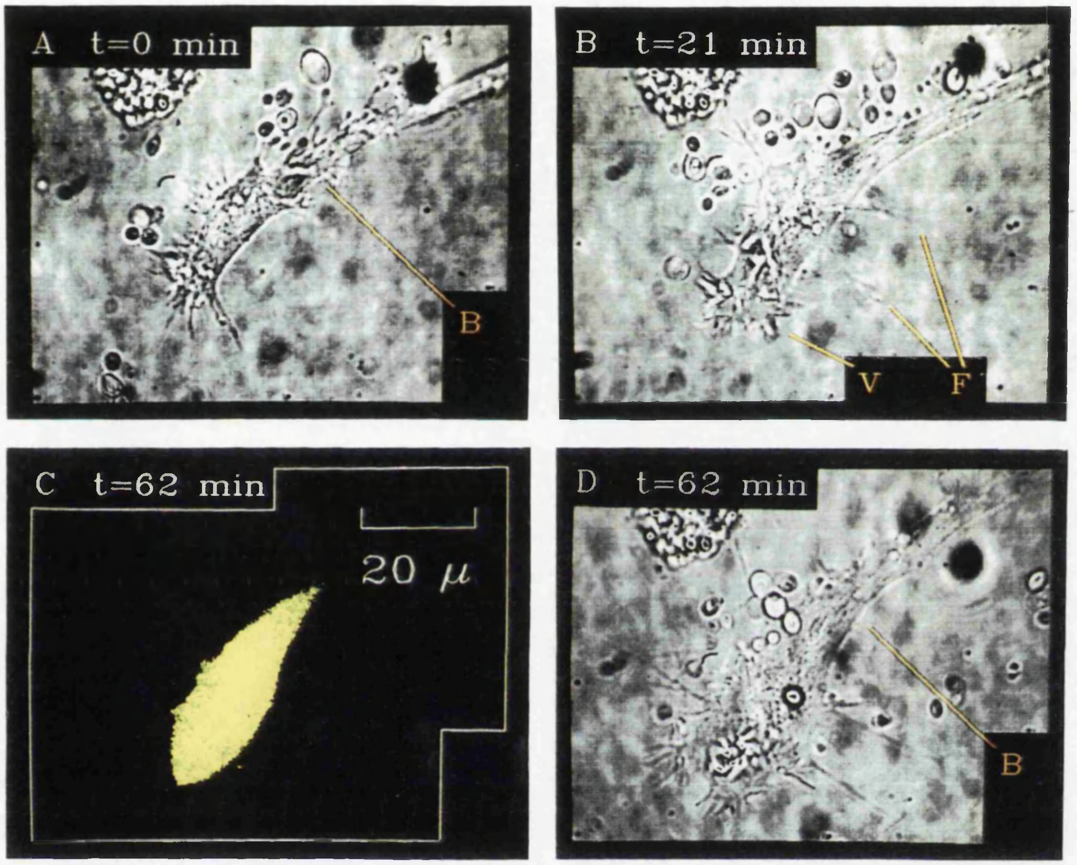
A t=0 min
B
B t=21 min
V
F
C t=62 min
20 μ
D t=62 min
B

Figure 4.5 Fura-2 ratio imaging of a retracting growth cone

Part A shows a bright field image of the growth cone. The time at which this image was acquired was defined as t=0, a membrane veil is indicated by V. Part B shows an image acquired at t=36 minutes. The veil has retracted, leaving retraction fibers (RF). The growth cone is beginning to move upwards, towards the cell body that lies out of the frame of view. Part C shows the fura-2 ratio image acquired 58 seconds after image B. Overall R=2.22, $[Ca^{2+}]_i$=246 nM.

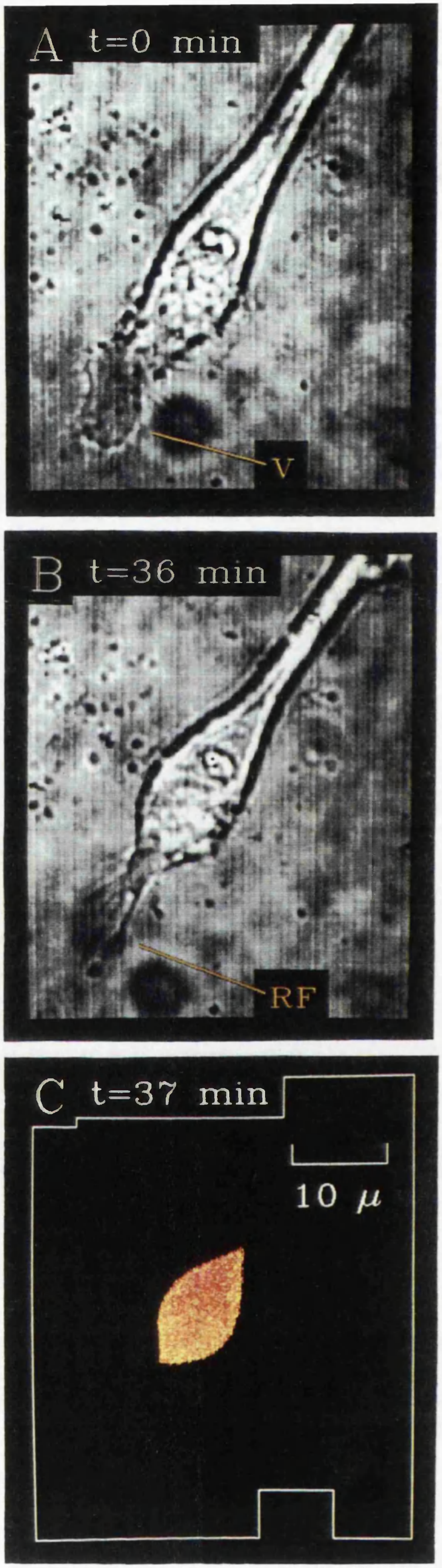
A t=0 min
V
B t=36 min
RF
C t=37 min
10 μ

veils and filopodia) were retracted into the central core of the growth cone. Retraction fibres remained where veils had been retracted. The second phase of retraction consisted of a balling-up of the growth cone together with a mass movement of the growth cone back towards the cell body. Figure 4.5 illustrates a retracting growth cone. The fura-2 ratio image (Fig. 4.5C) is orange, indicating a relatively high $[Ca^{2+}]_i$. In nine retracing growth cones R was 2.12±0.26, $[Ca^{2+}]_i$=225±58 nM (Fig. 4.9). Within this wide range of $[Ca^{2+}]_i$ the lower values (R=1.62±0.04, n=5; $[Ca^{2+}]_i$=119±9 nM) were found in growth cones during the retraction of veils, while higher values (R=2.59±0.27, n=5; $[Ca^{2+}]_i$=324±62 nM) were found in growth cones that were retracing back towards the cell body.

Growth cones switched between all of the behavioural states, in both directions, with the exception that a switch out of the quiescent state was never observed. As the behavioural state changed, so did $[Ca^{2+}]_i$. Figure 4.6 shows an example of a growth cone that switched from the veil retracted state to the motile non-advancing state as $[Ca^{2+}]_i$ fell.

Figure 4.9 summarizes the correlation of growth cone behaviour with $[Ca^{2+}]_i$ for N1E-115 cells differentiated in the presence of DMSO. Although growth cone behaviour was categorized using strict criteria to allow analysis, the behaviour was graded. Figure 4.9 illustrates more clearly the range of both behaviour and calcium concentrations observed.

4.3 Spatial gradients of $[Ca^{2+}]_i$

Spatial gradients of R value and therefore $[Ca^{2+}]_i$ within growth cones were always small. The value of R, and therefore $[Ca^{2+}]_i$, was consistently lower in the growth cone as compared with the cell body ($R_{growth\ cone} - R_{soma} = -0.15 \pm 0.06$, n=28, $[Ca^{2+}]_{i,growth\ cone} - [Ca^{2+}]_{i,soma} = -31 \pm 12$ nM). This difference was not a simple artifact produced by the greater path length or signal at the cell body because the

Figure 4.6 Recovery of motility coincides with a fall of $[Ca^{2+}]_i$

The growth cone was monitored for 18 minutes prior to the acquisition of bright field image A; during this period the growth cone showed behaviour intermediate between flattening and retraction. The time of acquisition of A was defined as t=0. Panel B shows a fura-2 ratio image acquired 51 seconds after image A; overall R=2.01, $[Ca^{2+}]_i$=201 nM. Panel C shows a ratio image at t=12 minutes. Overall R=1.56, $[Ca^{2+}]_i$=108 nM. Panel D shows a bright field image acquired 27 seconds after image C. Panel E shows a ratio image at t=38 minutes. Overall R=1.46, $[Ca^{2+}]_i$=88nM. Part F shows the growth cone 60 seconds after image E. Over the 21 minutes between images A and F, a ruffle (R) appeared on the upper edge of the growth cone and extended upwards. The Fura-2 ratio images show a local region of low $[Ca^{2+}]_i$ at the ruffle. In image E, the region corresponding to the ruffle had a $[Ca^{2+}]_i$ 27 nM lower than the overall mean for the growth cone.

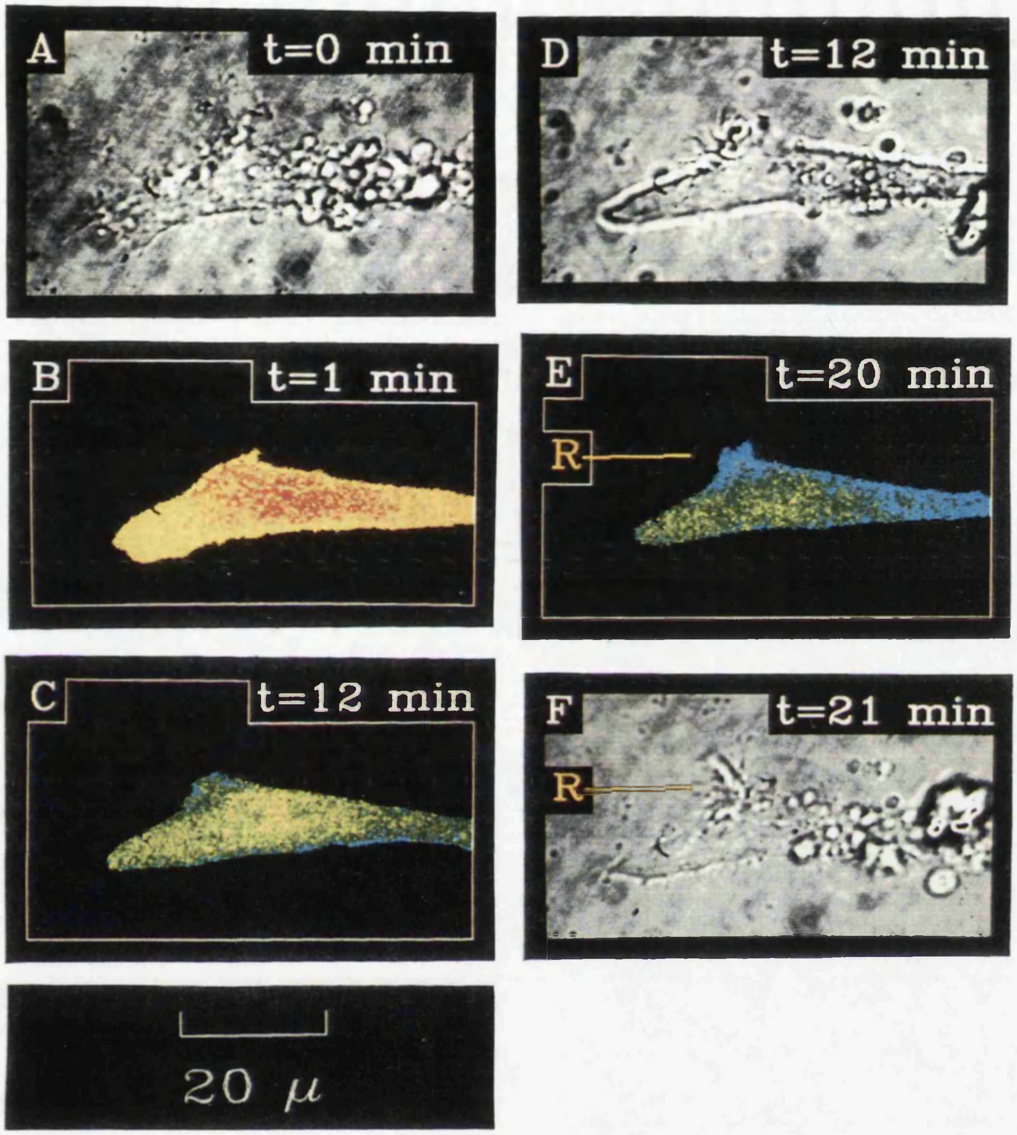
A
t=0 min
D
t=12 min
B
t=1 min
E
t=20 min
R
C
t=12 min
F
t=21 min
R
20 μ

difference recorded in cells injected with ANTS, a dye with excitation and emission spectra similar to fura-2 but which is insensitive to $[Ca^{2+}]_i$, was much smaller and was of opposite sign ($R_{growth\ cone} - R_{soma} = +0.03 \pm 0.01$, n=13). However the slight elevation of $[Ca^{2+}]_i$ in the cell body may be a result of local damage caused by injection of fura-2 into the soma.

A gradation of R values within the growth cone was often observed, with R highest in the centre and lower both at the junction with the neurite and at the leading edge (Fig. 4.3). When all the growth cones were averaged only the leading edge/centre difference proved statistically significant ($R_{leading\ edge} - R_{centre} = -0.04 \pm 0.01$, n=47, $p<0.001$). This difference corresponded to a calcium gradient of 10 nM. No such gradient appeared in growth cones injected with ANTS ($R_{leading\ edge} - R_{center} = +0.003 \pm 0.004$, n=12).

Goldberg (1988) has suggested that advancement of veils may be caused by a local elevation of $[Ca^{2+}]_i$. Raised $[Ca^{2+}]_i$ in advancing veils was never observed, to the contrary, $[Ca^{2+}]_i$ was either the same as the average for the whole growth cone (Fig. 4.2) or very slightly lower. In six advancing veils mean $R_{advancing\ veil} - R_{whole\ growth\ cone} = -0.03 \pm 0.01$, ($p<0.05$), corresponding to a $[Ca^{2+}]_i$ difference of 8 nM. Prominent, discrete ruffles (termed 'motile fans' by Bolsover *et al.*, 1988) often showed a locally low $[Ca^{2+}]_i$ (Figs. 4.3 and 4.6), but the phenomenon was more variable and the difference was not statistically significant ($R_{prominent\ ruffle} - R_{whole\ growth\ cone} = -0.04 \pm 0.02$, n=8, corresponding to a $[Ca^{2+}]_i$ difference of 10 nM). The ruffling margins of lamellipodia showed a significantly lower R ($R_{ruffling\ margin} - R_{whole\ growth\ cone} = -0.04 \pm 0.01$, n=7, $P<0.01$, corresponding to a $[Ca^{2+}]_i$ difference of 10 nM) but this gradient was no more pronounced than the general tendency for the leading edge of the growth cone to show a lower $[Ca^{2+}]_i$.

Freeman *et al.*, (1985) have suggested that calcium channels are concentrated in the membrane of filopodia producing a steady Ca^{2+} influx into the filopodia in unstimulated cells. If such a local influx occurred in neuroblastoma cells then $[Ca^{2+}]_i$ would be expected to be higher at the filopodial base. Raised $[Ca^{2+}]_i$ was never observed at the base of filopodia (Figs. 4.2 and 4.4), rather, calcium in these regions was, like other areas of the growth cone margin, slightly but not significantly lower than the growth cone average ($R_{filopodial\ base}$ - $R_{whole\ growth\ cone}$ = -0.08±0.05, n=8, corresponding to a $[Ca^{2+}]_i$ difference of 17 nM).

4.4 Control experiments

4.4.1 Control for the effect of DMSO on behaviour and $[Ca^{2+}]_i$

N1E-115 cells extend neurites 1-2 days after suspension and replating in the absence of DMSO, however, after 2 days the neurites are retracted and the cells re-enter the cell division cycle. A number of these cells were injected with fura-2 and although $[Ca^{2+}]_i$ values were lower, the relationship between $[Ca^{2+}]_i$ and behavioural state was maintained: Soma, R = 1.39±0.06, n=9, $[Ca^{2+}]_i$ 75±13 nM; growth cones: motile advancing, R =1.20±0.02, n=3, $[Ca^{2+}]_i$ = 37±4 nM; motile non-advancing, R = 1.25±0.02, n=7, $[Ca^{2+}]_i$ = 47±4 nM (Fig. 4.8); flattening, R = 1.36_0.06, n=3, $[Ca^{2+}]_i$ = 68±12nM; retracting, R=1.38±0.08, n = 6, $[Ca^{2+}]_i$ = 73±15 nM. Spatial gradients of $[Ca^{2+}]_i$ were similar in the presence and absence (Fig. 4.7) of DMSO. As with cells differentiated in the presence of DMSO, soma $[Ca^{2+}]_i$ was higher than growth cone $[Ca^{2+}]_i$, although the difference was not significant ($R_{growth\ cone}$ - R_{soma} = -0.02±0.05, n=9). Gradients of R value were seen within growth cones, with R highest in the centre and lower both at the junction of the neurite and at the leading edge (Fig. 4.7), however only the junction/centre difference was statistically significant ($R_{junction}$-R_{centre}=-0.03±0.01, n=11, $p<0.025$). This difference corresponded to a calcium gradient of 5 nM. Compared with the whole growth cone $[Ca^{2+}]_i$ was significantly lower in advancing veils ($R_{advancing\ veil}$ - $R_{whole\ growth\ cone}$ = -0.02±0.01, n=8, $p<0.01$, corresponding to a $[Ca^{2+}]_i$ difference of 3

Figure 4.7 $[Ca^{2+}]_i$ in a growth cone differentiating in the absence of DMSO

Part A fura-2 ratio image of a motile non-advancing growth cone of a cell plated and measured in the absence of DMSO; overall R=1.10, $[Ca^{2+}]_i$= 19 nM. The time of acquisition of this image was defined as t=0. Mean R in the region of advancing veils (distal to, and including, the four prominent dark spots that form a line across the growth cone in Part B) was 1.10, equal to the mean for the whole growth cone. Part B shows a bright field image of the growth cone 21 seconds later, filopodia are indicated by F. The yellow lines indicating filopodia are placed in the same position in images A and B. The growth cone/neurite boundary is indicated by B. Part C shows a fura-2 ratio image acquired 10 minutes after image A; overall R=1.12, $[Ca^{2+}]_i$= 22 nM. Mean R in the region of advancing veils (distal to, and including, the four prominent dark spots that form a line across the growth cone in Part D) was 1.10, $[Ca^{2+}]_i$=19 nM, less than the mean for the whole growth cone. Part D shows the growth cone 31 seconds after image C; V indicates the advancing veils. The yellow lines indicating veils are placed in the same position in images C and D. Part E shows the growth cone 42 minutes after acquisition of image A. The veils have advanced further, however, the growth cone/neurite boundary (B, yellow line in same position as in image B) has not advanced. A growth cone from a cell differentiating in the presence of DMSO would have been expected to be either quiescent or motile advancing at such low $[Ca^{2+}]_i$.

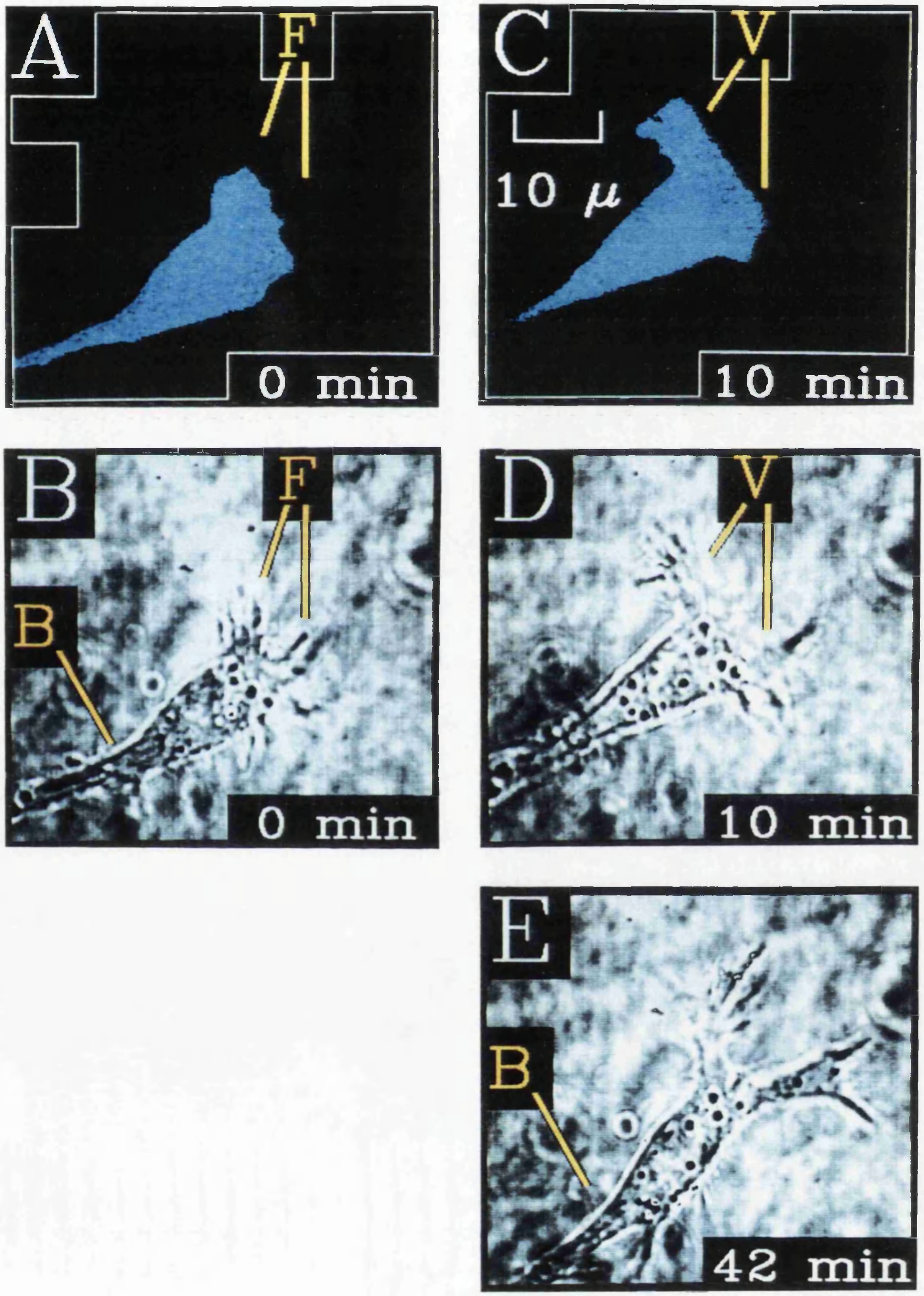
A
F
0 min
C
V
10 μ
10 min
B
F
B
0 min
D
V
10 min
E
B
42 min

nM). As before, there was no evidence for raised $[Ca^{2+}]_i$ at the base of filopodia ($R_{filopodia} - R_{whole\ growth\ cone} = -0.02 \pm 0.01$, n=6, not significant).

4.4.2 Injection of ANTS

An apparent correlation of $[Ca^{2+}]_i$ and growth cone behavioural state might arise not from real differences of $[Ca^{2+}]_i$ but from an artifact caused by factors such as UV absorption, light scattering, or the intracellular environment being different in growth cones of different behavioural states. In order to test this, ratio measurements on DMSO-differentiated cells were made using the same excitation and barrier filters but injecting ANTS (8-aminonaphthalene-1,3,6-trisulphonic acid) instead of fura-2. ANTS is a dye with excitation and emission spectra similar to fura-2 but is unaffected by either $[Ca^{2+}]_i$, or pH. As with fura-2 measurements, R for ANTS was normalized such that R=1 for ANTS in the *in vitro* standard solution (zero Ca^{2+} solution, Table 2.1a). R for intracellular ANTS was consistently less than 1, however the mean R value was not significantly different in any of the growth cone behavioural groups observed: quiescent, $R=0.81 \pm 0.03$, n=4; motile non-advancing, $R=0.83 \pm 0.01$, n=4 and retracting ($R=0.80 \pm 0.04$, n=9) ($p > 0.05$ for all pairs). Therefore the different R values recorded for fura-2 in growth cones of different behavioural states were not an artifact of differing geometry or intracellular conditions but do indeed result from different $[Ca^{2+}]_i$.

4.4.3 Fura-2 AM loading

Fura-2 can be introduced into cells in two ways, by direct injection of the free acid (the calcium-sensitive species) or by incubation in a suspension with the membrane-permeable acetoxymethyl ester, fura-2 AM. In order to compare the $[Ca^{2+}]_i$ data directly with other studies a group of 31 DMSO-differentiated cells were loaded with fura-2 using the AM-loading technique. The protocol was similar to that of Connor (1986). Cell bodies of AM-loaded cells showed

Figure 4.8 Apparent spatial gradients of [Ca^{2+}]$_i$ in cells loaded by incubation in fura-2 AM

Part A shows a bright field image of cells loaded using the acetoxymethyl ester (AM) of fura-2. A neurite (N) of one cell terminates in a growth cone with a prominent ruffle (R). The flattened cell body of a second cell lies to the right of the growth cone. Part B shows the fura-2 ratio image acquired 24 seconds after image A. The growth cone and cell body show localized, discrete regions with high indicated [Ca^{2+}]$_i$. These steady state gradients were never observed in cells injected with fura-2.

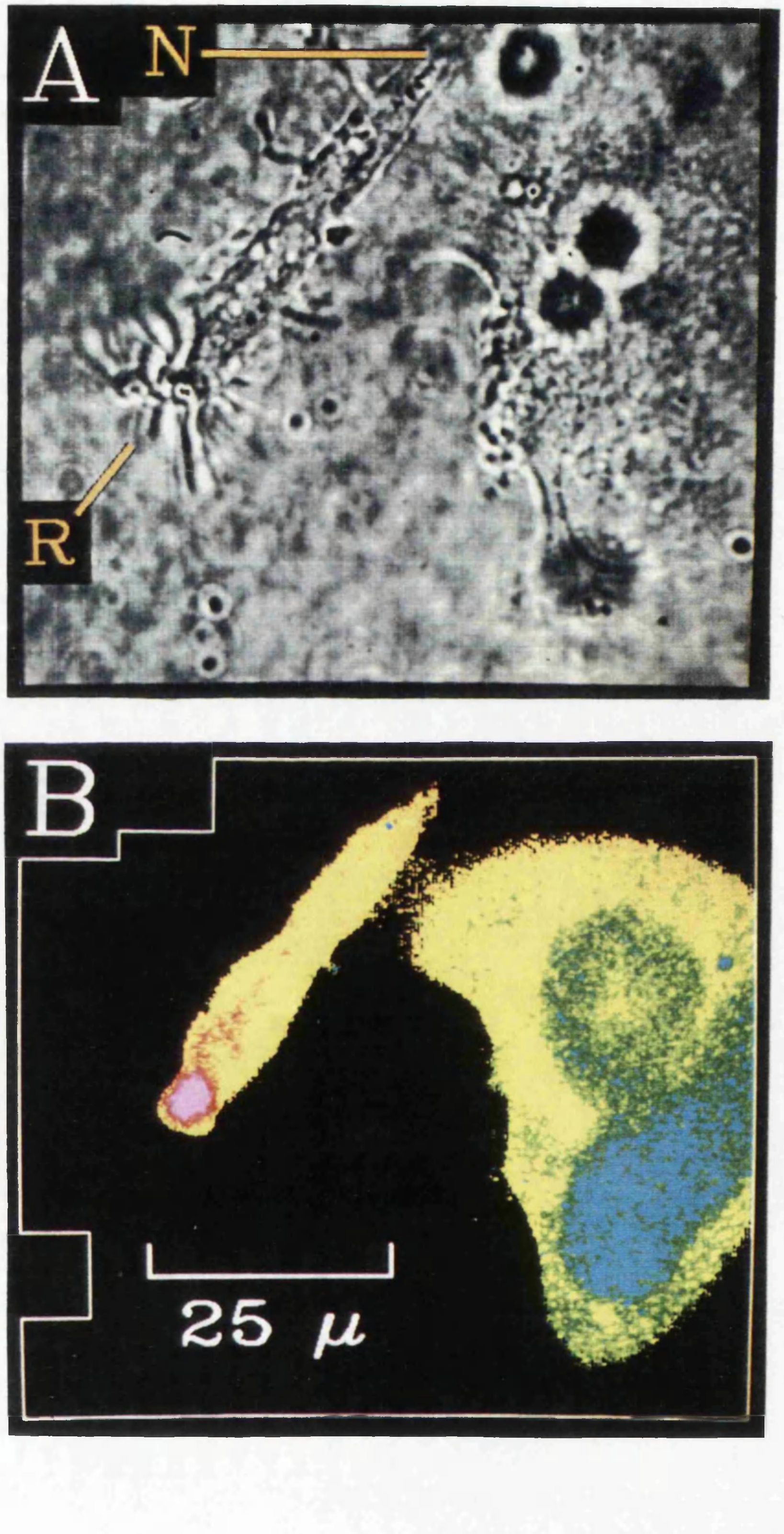
A
N
R
B
25 μ

Figure 4.9 Mean ratio values with corresponding $[Ca^{2+}]_i$, for the five growth cone behavioural states

The graph shows the relationship between growth cone behaviour and correlated ratio (R) and $[Ca^{2+}]_i$ (Ca). Only growth cones of cells differentiated with DMSO and injected with fura-2 are included. Growth cones that could not be placed unequivocally into one of the five behavioural states were not used in the calculation of these means. Bars are ± one standard error. The number of growth cones for each point are, from left to right, 8, 7, 20, 9 and 8 respectively.

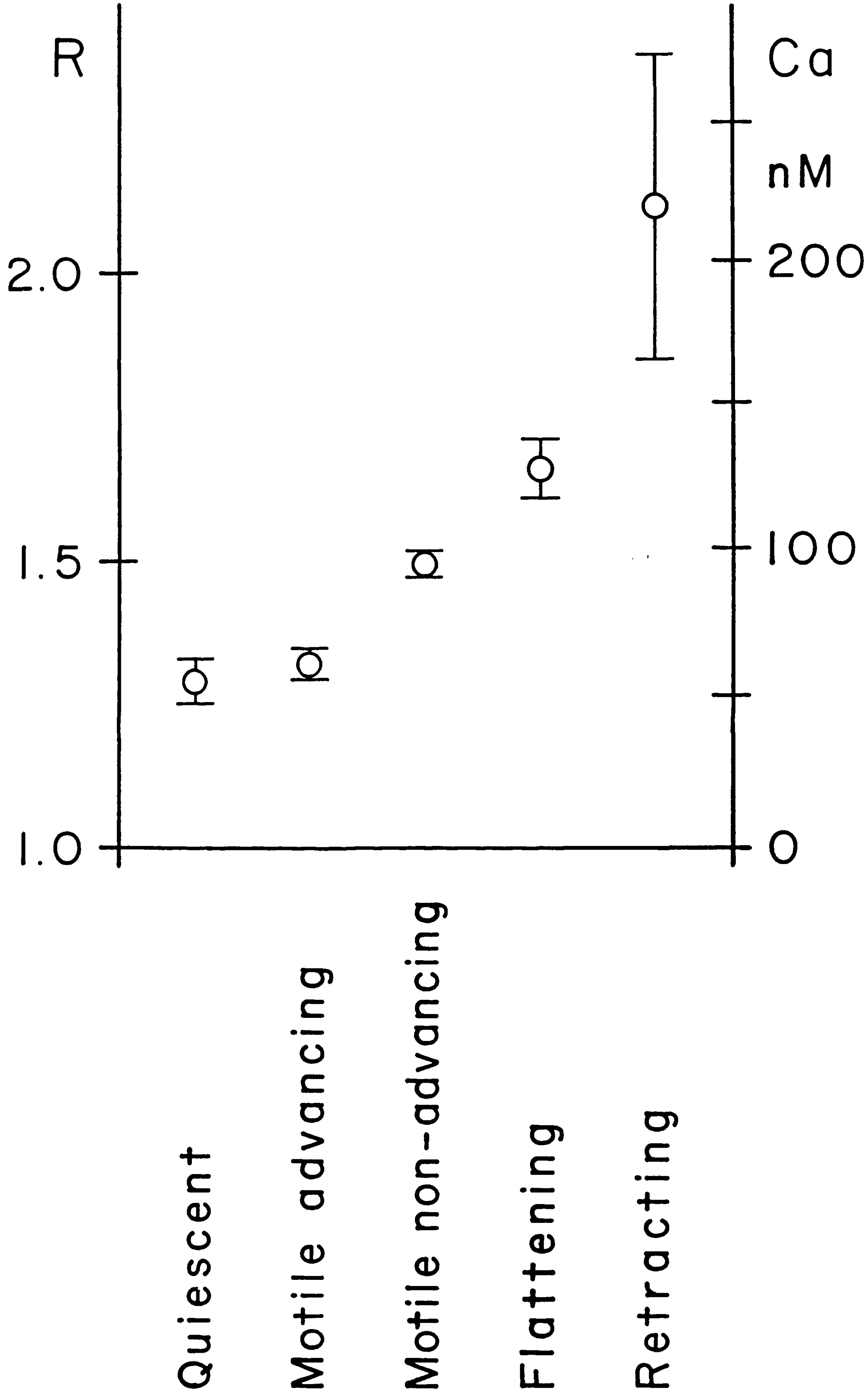
R
2.0
1.5
1.0
Ca
nM
200
100
0
Quiescent
Motile advancing
Motile non-advancing
Flattening
Retracting

pronounced spatial gradients (Fig. 4.8), while seven growth cones showed prominent, discrete regions of high-$[Ca^{2+}]_i$ at the leading edge (Fig. 4.8). These phenomena were never observed when fura-2 was introduced by injection. Regional R and, therefore, indicated $[Ca^{2+}]_i$ were considerably higher in AM-loaded cells, and variation of growth cone $[Ca^{2+}]_i$ among growth cones of each behavioural state was much greater than when fura-2 was introduced by injection. Soma, $R=1.70\pm0.05$, $n=8$, $[Ca^{2+}]_i=134\pm11$ nM. Growth cones: quiescent, $R=1.98\pm0.13$, $n=5$, $[Ca^{2+}]_i=192\pm26$ nM; motile advancing, $R=1.64\pm0.11$, $n=9$, $[Ca^{2+}]_i=124\pm22$ nM; motile non-advancing, $R=1.72\pm0.12$, $n=8$, $[Ca^{2+}]_i=140\pm24$ nM; retracting, $R=1.79\pm0.08$, $n=11$, $[Ca^{2+}]_i=154\pm17$ nM. In no pair of these growth cone values is the difference statistically significant.

4.5 Discussion of results: correlation of growth cone behaviour with $[Ca^{2+}]_i$

True growth at the growth cone consists of advance at two locations. The leading edge of the growth cone moves forward by extending veils (Goldberg and Burmeister, 1986) or by being pulled forward by the tension in filopodia (Bray, 1987). The boundary between the neurite and the growth cone moves forward through an extension of the microtubule/neurofilament cytoskeleton (Goldberg and Burmeister, 1986). In this study true growth occurred only in those growth cones in which $[Ca^{2+}]_i$ was lowest. $[Ca^{2+}]_i$ in motile advancing growth cones was not significantly different from $[Ca^{2+}]_i$ in quiescent growth cones. The correlation, in motile growth cones, between raised $[Ca^{2+}]_i$ and failure of the neurite/growth cone boundary to advance, leads to the conclusion that raised $[Ca^{2+}]_i$ opposes extension of the microtubule/neurofilament cytoskeleton within the neurite. In motile advancing growth cones all the activity associated with growth, including filopodial extension, occurred at low $[Ca^{2+}]_i$. Thus raised $[Ca^{2+}]_i$ is not essential for any of these processes.

Retraction was observed when growth cone $[Ca^{2+}]_i$ rose to 120 nM and above. The first effect seen as $[Ca^{2+}]_i$ rose was a pulling of motile structures such as veils and ruffles into the main body of the growth cone. If $[Ca^{2+}]_i$ fell, motility returned. At higher levels of $[Ca^{2+}]_i$ the growth cone moved back towards the cell body, as if pulled by tension in the neurite. It is likely that raised $[Ca^{2+}]_i$ causes retraction. Injection of Ca^{2+} into growing neuroblastoma cells causes a reversible retraction of motile structures (Bolsover *et al.*, 1988). Calcium induced retraction may be of importance during development when neuronal connections are pruned. The conversion of motile growth cones into retracting growth cones often proceeded through a transitional, flattening stage, during which $[Ca^{2+}]_i$ had a value intermediate between the $[Ca^{2+}]_i$ values characteristic of motile non-advancing and retracting growth cones. During flattening, growth cones extended veils and, less often, filopodia. Growth cone area increased and the leading edge of the growth cone advanced, however, the boundary between the neurite and the growth cone did not advance. Anglister *et al.* (1982) observed flattening of growth cones after treatment with calcium ionophore. Results from flattening growth cones taken with those of Anglister *et al.*, (1982) show that raised $[Ca^{2+}]_i$ can promote veil extension, but only at $[Ca^{2+}]_i$ levels that are non-permissive for neurite growth. Many growth cones passed directly from the motile non-advancing state to retraction; in these growth cones the first effect of raised $[Ca^{2+}]_i$ was not the extension of veils and ruffles but rather a pulling in of these structures. It is possible that the precise layout of the cytoskeleton within the growth cone and the extent to which different parts of the cytoskeleton are exposed to raised $[Ca^{2+}]_i$ determines whether the initial effect of raised $[Ca^{2+}]_i$ is to produce flattening or retraction.

Several authors have suggested that local regions of raised $[Ca^{2+}]_i$ may occur within growth cones, and may trigger local events. Connor (1986) found local regions of high $[Ca^{2+}]_i$ at the base of extending filopodia. Goldberg (1988) suggested that veil extension might occur from regions of the growth cone in which $[Ca^{2+}]_i$ was locally high. In this study local elevations of $[Ca^{2+}]_i$ were never observed at the base of filopodia or within motile structures. Rather, where gradients existed, $[Ca^{2+}]_i$ was on average 5 to 10 nM lower within motile structures. It is unlikely that such small $[Ca^{2+}]_i$ gradients have any physiological role although it is possible that the local regions of low $[Ca^{2+}]_i$ trigger the production of motile structures, it is equally possible that motile regions, perhaps by virtue of their high surface area/volume ratio, may create a low $[Ca^{2+}]_i$ within themselves. Although it was suggested above that local regions of high $[Ca^{2+}]_i$ may promote local veil advance, the results of this study clearly show that all types of motility, including veil advance, can occur in the absence of locally elevated $[Ca^{2+}]_i$. Thus under these conditions, where there is no external stimuli, the site at which motility occurs is dependent on factors other that locally raised $[Ca^{2+}]_i$.

The majority of the results were obtained using N1E-115 cells differentiated with DMSO (Kimhi *et al.*, 1976) and therefore might not be typical of other growth cones. DMSO causes a significant reduction in the concentration of cAMP within N1E-115 cells (Kimhi *et al.*, 1976). Furthermore, DMSO might disrupt $[Ca^{2+}]_i$ gradients, perhaps by distorting the structure of the cell membrane. However, very similar results were obtained in growth cones of N1E-115 cells grown and measured in the absence of DMSO. The results are therefore not an artifact of the DMSO treatment. The results obtained with fura-2 AM loaded cells were very different to those for cells injected with fura-2, the reasons for these differences will be discussed in chapter 6.

To summarize, the results show that the various processes occurring at the growth cone are differentially sensitive to $[Ca^{2+}]_i$. Veil extension can be promoted by raised $[Ca^{2+}]_i$. Ruffling is insensitive to $[Ca^{2+}]_i$ until $[Ca^{2+}]_i$ rises to a levels that cause retraction. Advance of the neurite/growth cone boundary requires low $[Ca^{2+}]_i$.

Chapter 5

The spatial distribution of voltage-gated calcium influx and associated morphological changes at the neuronal growth cone

The experiments described in this chapter were done on cells bathed in saline. $[Ca^{2+}]_i$ was measured with a high temporal resolution (60 ms) during electrical stimulation. The results in this chapter show transient changes in $[Ca^{2+}]_i$ unlike the previous chapter which described steady state $[Ca^{2+}]_i$.

5.1 Changes in fluorescence intensity at the growth cone indicate a change in $[Ca^{2+}]_i$

Voltage-gated calcium influx into the neuronal growth cone was measured by simultaneous digital fluorescence imaging and the whole-cell patch-clamping. Growth cone resting $[Ca^{2+}]_i$ was measured at the holding voltage using ratio imaging (with a temporal resolution of 3 seconds). Growth cones were then illuminated with 380 nm light and the spatial distribution of fluorescence emitted by intracellular fura-2 was recorded (with a 60 ms temporal resolution) during a 1 s depolarizing voltage pulse.

During a voltage pulse that selectively activated the L-type current (a voltage pulse to +10 mV, from a holding voltage of -40 mV), I_{380} (intensity of fluorescence when exciting with 380 nm light) recorded from the growth cone fell dramatically, to 68±4% of control, indicating a rise of $[Ca^{2+}]_i$ of 265±73 nM (n=32). A similar voltage protocol resulted in a 19±4% (n=4) increase of fluorescence when growth cones were illuminated with 350 nm light. No change in the I_{380} signal was observed in control runs in which the growth cone was voltage-clamped at the holding potential but not depolarized. Addition of the calcium channel blocker $CoCl_2$ (10 mM) eliminated both the calcium currents and the associated change in the I_{380} signal (n=7). These results indicate that the fluorescence changes were caused by a large increase of $[Ca^{2+}]_i$ at the growth cone (Fig. 5.1d) since artifacts such as a fall in the concentration of fura-2, a reduction of growth cone thickness, or dye bleaching would cause a fall of fluorescence at both excitation wavelengths or a change in the I_{380} signal at the holding voltage. Several properties of the growth cone fura-2 signal indicated that it was caused by calcium influx through L-type calcium channels. I_{380} fell throughout the 1 s depolarization, consistent with Ca^{2+} influx through a weakly inactivating channel (Fig. 5.1d). The divalent cation sensitivity of both the $[Ca^{2+}]_i$ change and the current (Fig. 5.2) were consistent with L channel activation (Narahasi *et al.*, 1987; Tsien *et al.*, 1988).

The $[Ca^{2+}]_i$ change during T-type current activation (28±8 nM, n=9) was smaller than that during L-type current activation. The voltage dependence and the divalent cation sensitivity of the current (Fig. 5.2) and the $[Ca^{2+}]_i$ change were consistent with Ca^{2+} influx through T-type channels.

5.2 The spatial distribution of calcium influx through L- and T-type channels in the neuronal growth cone

5.2.1 $[Ca^{2+}]_i$ changes caused by influx through L-type channels

The changes in $[Ca^{2+}]_i$ at the growth cone during L-type current activation were highly localized to a limited number of 'hotspots' (Fig 5.1a). The mean diameter of the hotspots measured at the beginning of the depolarizing pulse was 7.3±0.4 μm (n=44), this is similar to the limit of resolution for the DIFM (7 μm). The resolution of the DIFM was calculated assuming the focal plane was within the upper and lower growth cone membrane using the measured average growth cone thickness of 5.4±0.5 μm (n=8) and the collection angle measured

Figure 5.1 Calcium hotspots at the neuronal growth cone

Parts a and b show pseudocolour images of the growth cone indicating the spatial distribution of the change in $[Ca^{2+}]_i$. n, a neurite leading to a cell body that lies out of the field of view, p, processes extending from the growth cone. The images were produced by dividing the background-corrected video frame that began 0.5 s after the onset of depolarization by a background-corrected video frame acquired at the holding voltage 0.5 s before the onset of depolarization. Image a was produced by activation of L-type calcium channels during a 1 s voltage pulse to +10 mV from a holding voltage of -40 mV. The increase of $[Ca^{2+}]_i$ was highly localized in three discrete hotspots. Image b was produced by activation of T-type calcium channels during a voltage pulse to -35 mV from a holding voltage of -100 mV. The increase of $[Ca^{2+}]_i$ was 82 nM and uniform. A detectable $[Ca^{2+}]_i$ increase (28±8 nM) was observed during T-type current activation in nine growth cones. In no case were hotspots observed, although gross gradients in which calcium change was greatest at the growth cone periphery were occasionally seen (Fig. 5.2c). Part c shows the spatial distribution of $[Ca^{2+}]_i$ during activation of T- and L-channels. Each distribution is calculated from the values of I_{380} along the vector ab indicated in the images a and b. The dashed line indicates the $[Ca^{2+}]_i$ increase produced by activation of T-channels, calculated from image b. The solid lines show the $[Ca^{2+}]_i$ increase 1/2 s (calculated from image a) and 1 s (image not shown) after activation of L-channels. Part d shows the timecourse of $[Ca^{2+}]_i$ changes during 1 s activation of L channels. ◻: $[Ca^{2+}]_i$ calculated from the whole growth cone I_{380}. ▽: $[Ca^{2+}]_i$ at the lower hotspot on the line ab. The cell was bathed in medium B (Table 2.3) at 20 °C.

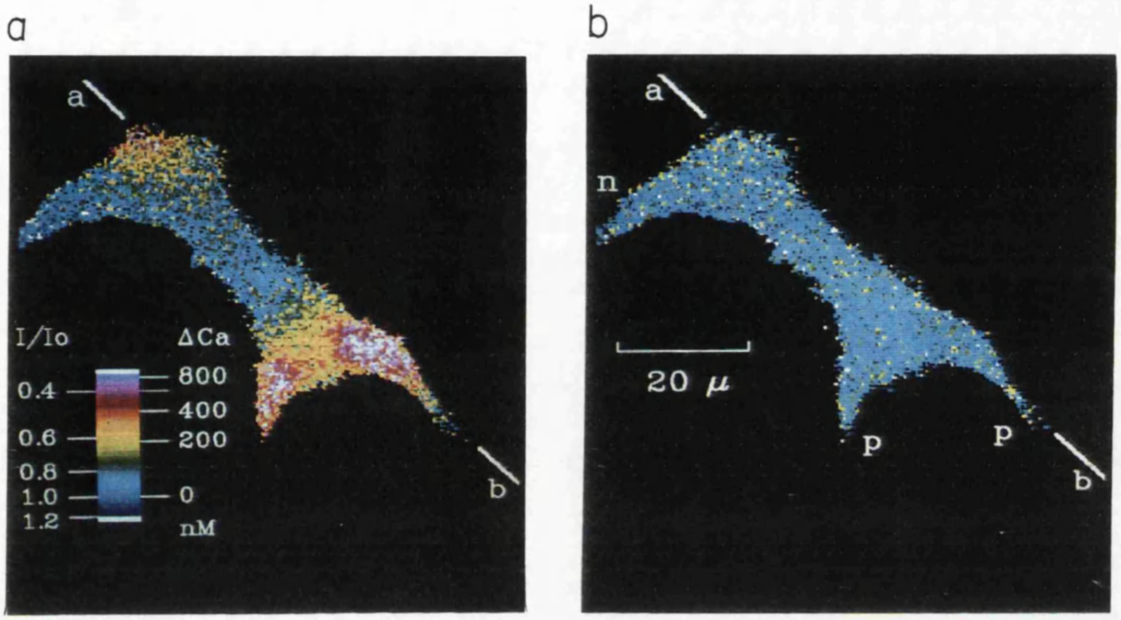
a
b
a
b
I/Io
ΔCa
0.4
0.6
0.8
1.0
1.2
800
400
200
0
nM
a
n
20 μ
p
p
b

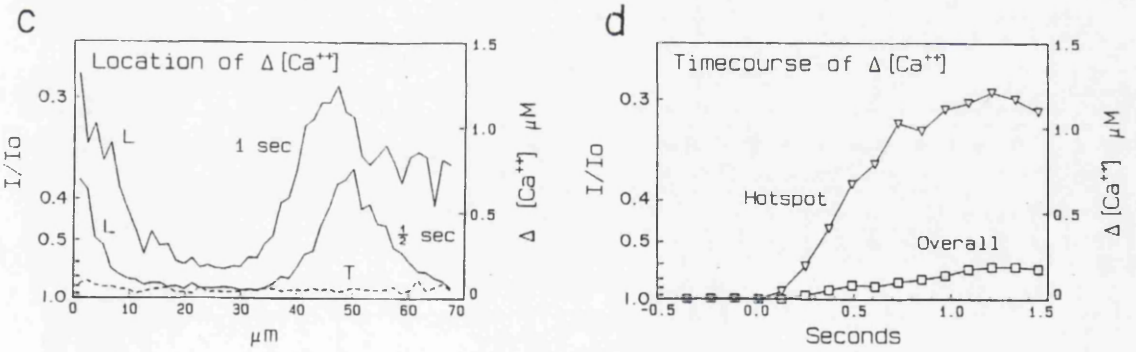
c
Location of Δ[Ca⁺⁺]
I/Io
0.3
0.4
0.5
1.0
L
L
1 sec
½ sec
T
1.5
1.0
0.5
0
Δ [Ca⁺⁺] μM
0
10
20
30
40
50
60
70
μm
d
Timecourse of Δ[Ca⁺⁺]
I/Io
0.3
0.4
0.5
1.0
Hotspot
Overall
1.5
1.0
0.5
0
Δ [Ca⁺⁺] μM
-0.5
0.0
0.5
1.0
1.5
Seconds

from the PSF (see Section 2.2.6). The true hotspot dimensions are therefore likely be smaller than the measured value. Growth cones contained between one and five hotspots (mean 1.9±0.2, n=32) however, there was no correlation between the number of hotspots per growth cone and time in the differentiation medium.

Changes in $[Ca^{2+}]_i$ at the hotspot were considerable. In one hotspot fura-2 became saturated with Ca^{2+} before the end of the 1 s depolarization implying $[Ca^{2+}]_i > 4$ μM. In 34 other growth cones $[Ca^{2+}]_i$ rose by 1.0±0.2 μM. The concentration of fura-2 in the growth cone was estimated to be about 100 μM. Fura-2 at this concentration does not change either the resting $[Ca^{2+}]_i$ or the growth cone behaviour (Section 4.2.1). However, the calcium-buffering capacity of the cytosol is likely to have been increased significantly. Thus under normal conditions $[Ca^{2+}]_i$ changes at the hotspot may be even larger than measured here. The concentration profile across the hotspot broadened as depolarization was maintained (Fig. 5.1C) suggesting that the major mechanism by which $[Ca^{2+}]_i$ increased in the cytoplasm outside the hotspot regions was diffusion of calcium from the hotspot. The effective diffusion constant for calcium in nerve cell cytoplasm has been measured as 8.3×10^{-7} cm/sec (Nasi and Tillotson, 1985). After injection of fura-2, most of the freely diffusible Ca^{2+} will be bound to fura-2. The effective diffusion constant of fura-2 inside cells is equal to the value in free solution, 3.6×10^{-7} cm^2/sec (Baylor and Hollingworth, 1988), approximately half the diffusion constant for Ca^{2+}. Thus injection of fura-2 might be expected to increase the spatial gradients slightly. However, this argument assumes that the calcium buffering is uniform and that the buffering by the plasma membrane is the same in the growth cone as it is in the soma. The growth cone has a high surface area to volume ratio compared to the soma so this assumption may not be valid.

$[Ca^{2+}]_i$ changes measured at the hotspot increased with time in the differentiating medium. Hotspot $[Ca^{2+}]_i$ did not alter significantly from day 2 to day 3, but then increased dramatically (day 2: 0.5±0.1 μM, n=6; day 3: 0.4±0.2 μM, n=11; day 7: 2.4±0.6 μM, n=15. The day 7 value is significantly different from both the day 3 value ($p<0.01$) and the combined day 2 and 3 values ($p<0.005$, t test).

The presence of 70 μM $CdCl_2$ in the external medium reduced both the L-type current (by 72±5%, n=8), and the $[Ca^{2+}]_i$ change at the hotspot (by 70±11%, n=7). The similar Cd^{2+} sensitivity of the whole-cell L-type current and growth cone $[Ca^{2+}]_i$ confirm that L-channels are responsible for calcium influx at the hotspot. Although Cd^{2+} is unlikely to enter the growth cone during L-type current activation (Lansman *et al.*, 1986), any Cd^{2+} that does enter will produce a fluorescent signal similar to Ca^{2+}. To avoid possible problems due to irreversible Cd^{2+} binding to fura-2, no further measurements were made on cells after the first depolarization in medium containing $CdCl_2$.

5.2.2 $[Ca^{2+}]_i$ changes caused by influx though T-type channels

The spatial distribution of $[Ca^{2+}]_i$ changes in the growth cone during T-type current activation (a voltage pulse to -35 mV from a holding voltage of -100 mV) were uniform (Fig. 5.1b). Hotspots were never observed during T-type current activation, although gross gradients in which the calcium change was greatest at the growth cone periphery were occasionally seen (Fig. 5.2c). These small, non-localized gradients were probably caused by gradients of surface area to volume ratio, that is, the growth cone is thinnest at the periphery.

5.2.3 Different spatial distributions of $[Ca^{2+}]_i$ caused by activation of L- and T-type channels occur during small $[Ca^{2+}]_i$ changes

By selecting growth cones that showed a small change in $[Ca^{2+}]_i$ at the hotspot and then applying 70 μM $CdCl_2$ it was possible to reduce the $[Ca^{2+}]_i$

Figure 5.2 Selective Cd^{2+} block of L-type current and calcium hotspot

Part a shows the membrane voltage and leak subtracted whole cell current during activation of L-channels. L, control; L(Cd^{++}); in the presence of 70 µM $CdCl_2$. Part b shows the membrane voltage and membrane leak-subtracted whole cell current during activation of T-channels. T, control; T(Cd^{++}), in the presence of 70 µM $CdCl_2$. Part c shows the spatial distribution of calcium, during activation of T- and L-channels along a line through the centre of a hotspot. T indicates the change in $[Ca^{2+}]_i$ 0.5 s after activation of the T-type current. L indicates the change in $[Ca^{2+}]_i$ 0.5 s after activation of the L-type current. L(Cd^{++}) indicates the $[Ca^{2+}]_i$ 0.5 s after activation of the L-type current in medium containing 70 µM $CdCl_2$. The hotspot $[Ca^{2+}]_i$ change in this growth cone was small, application of $CdCl_2$ reduced this change to the same order as that seen during T-channel activation. This shows that the different spatial distributions of $[Ca^{2+}]_i$ can occur at the same $[Ca^{2+}]_i$. The experiments were done in Medium B (Table 2.3) at 20 °C with pipettes containing Solution C (Table 2.3).

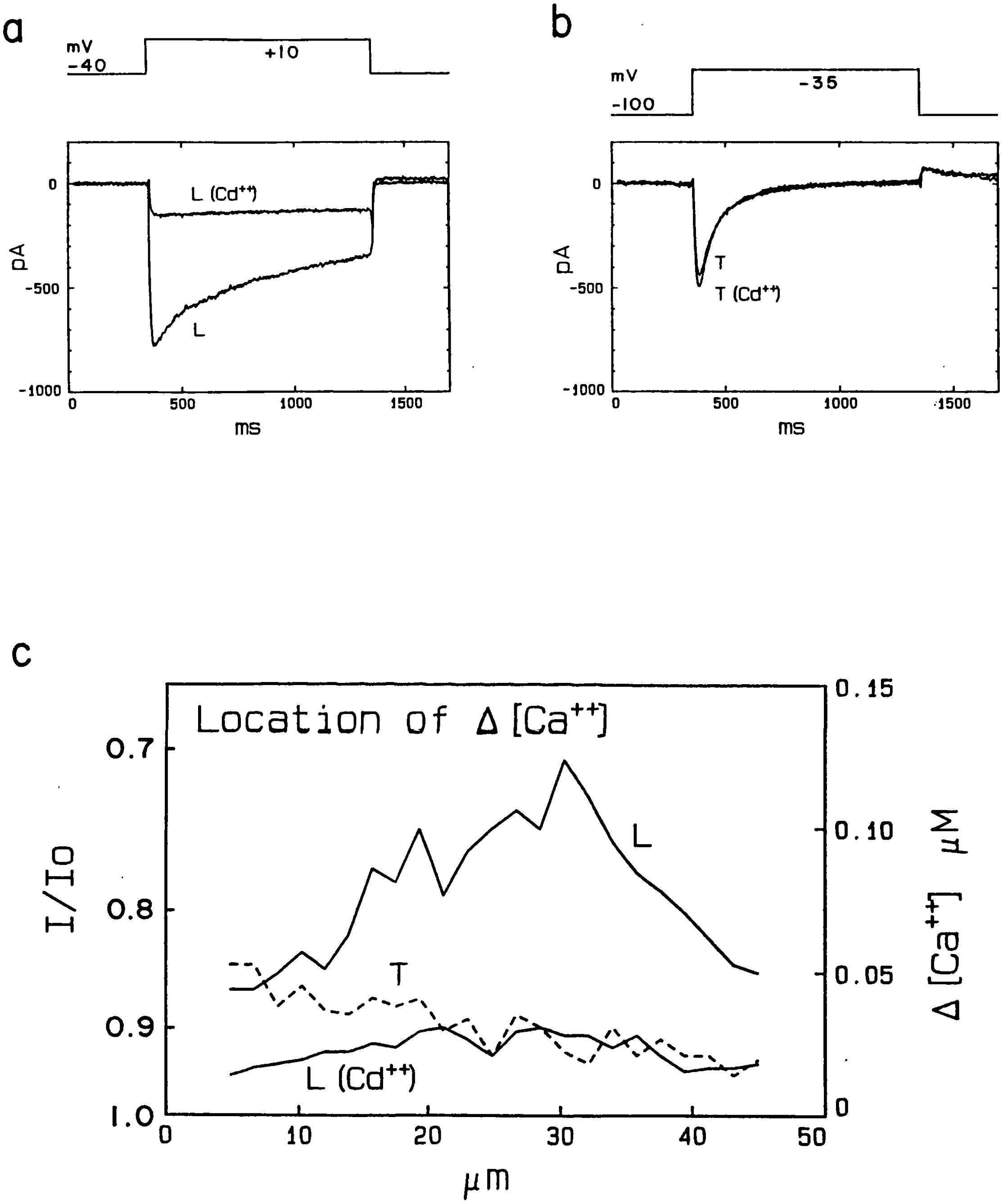
a
mV
-40
+10
0
L (Cd++)
pA
-500
L
-1000
0
500
1000
1500
ms
b
mV
-100
-35
0
pA
-500
T
T (Cd++)
-1000
0
500
1000
1500
ms
c
Location of Δ [Ca++]
0.7
0.8
0.9
1.0
I/Io
0.15
0.10
0.05
0
Δ [Ca++] μM
L
T
L (Cd++)
0
10
20
30
40
50
μm

change at the hotspot to levels seen during activation of the T-type current (Fig 5.2). As will be discussed later this showed that two different spatial distributions of calcium could occur at the same $[Ca^{2+}]_i$.

5.3 Morphological changes associated with localized voltage gated calcium influx

5.3.1 Correlation of hotspot position and growth cone shape

Out of the 32 growth cones studied 24 had processes at the growth cone (e.g. structures marked p in Figure 5.1b). Hotspots were usually located at the base of these processes. In the 24 process-bearing growth cones, processes made up 20% of the total circumference of the growth cone (measured as angles subtended at the growth cone centre). 38 of the 47 hotspots in these growth cones were located at the base of processes, indicating a high spatial correlation ($p<0.001$, χ^2 test). Hotspots were seen in both proximal and distal regions of the growth cone but were never observed in the neurite (n in Figs 5.1a and 5.3a).

5.3.2 Hotspot activation causes localized margin outgrowth

In order to examine the $[Ca^{2+}]_i$ changes produced under more physiological conditions, conventional microelectrodes were used to pressure-inject fura-2 and electrically stimulate cells (Fig. 5.3b) maintained in Medium C, Table 2.3, at 32-36 °C. Distinct $[Ca^{2+}]_i$ hotspots could be detected during a train of 5 action potentials at 10 Hz (Fig. 5.3a). On average, hotspot $[Ca^{2+}]_i$ rose by 89 ± 26 nM per action potential (n=11), that is, 12 action potentials would be required to raise hotspot $[Ca^{2+}]_i$ to micromolar levels.

To examine a possible correlation between the location of hotspots and the location at which the growth cone margin subsequently grew out, the site of maximum margin outgrowth in the 4 minutes following depolarization was identified. A hotspot was considered to be close to the site of maximum margin outgrowth if lines from the centre of the growth cone to the site of maximum

Figure 5.3 Calcium hotspots observed under physiological conditions

Part a shows a pseudocolour image of a growth cone indicating the spatial distribution of the increase of $[Ca^{2+}]_i$ that occurred during two action potentials. The image was produced by dividing images acquired at times shown by horizontal bars in b; n indicates the neurite leading to the cell body that lies out of the field of view. Part B shows a record of membrane voltage (upper trace) during a train of five action potentials elicited by depolarizing current pulses (lower trace). Part c shows the time course of $[Ca^{++}]_i$ changes during the action potential train, △: $[Ca^{++}]_i$ calculated from the whole growth cone I_{380}, □: $[Ca^{++}]_i$ at the hotspot. Measurements were made in Medium C (Table 2.3) at 32-36 °C. The micropipette contained 5 mM fura-2, 140 mM KCl and 5 mM HEPES at pH 7.1. The holding voltage was recorded to be -67 mV, but micropipettes with this filling solution exhibit unpredictable changes of tip potential upon cell impalement. $[Ca^{2+}]_i$ change was calculated using the measured resting $[Ca^{2+}]_i$ of 107±11 nM (n=53).

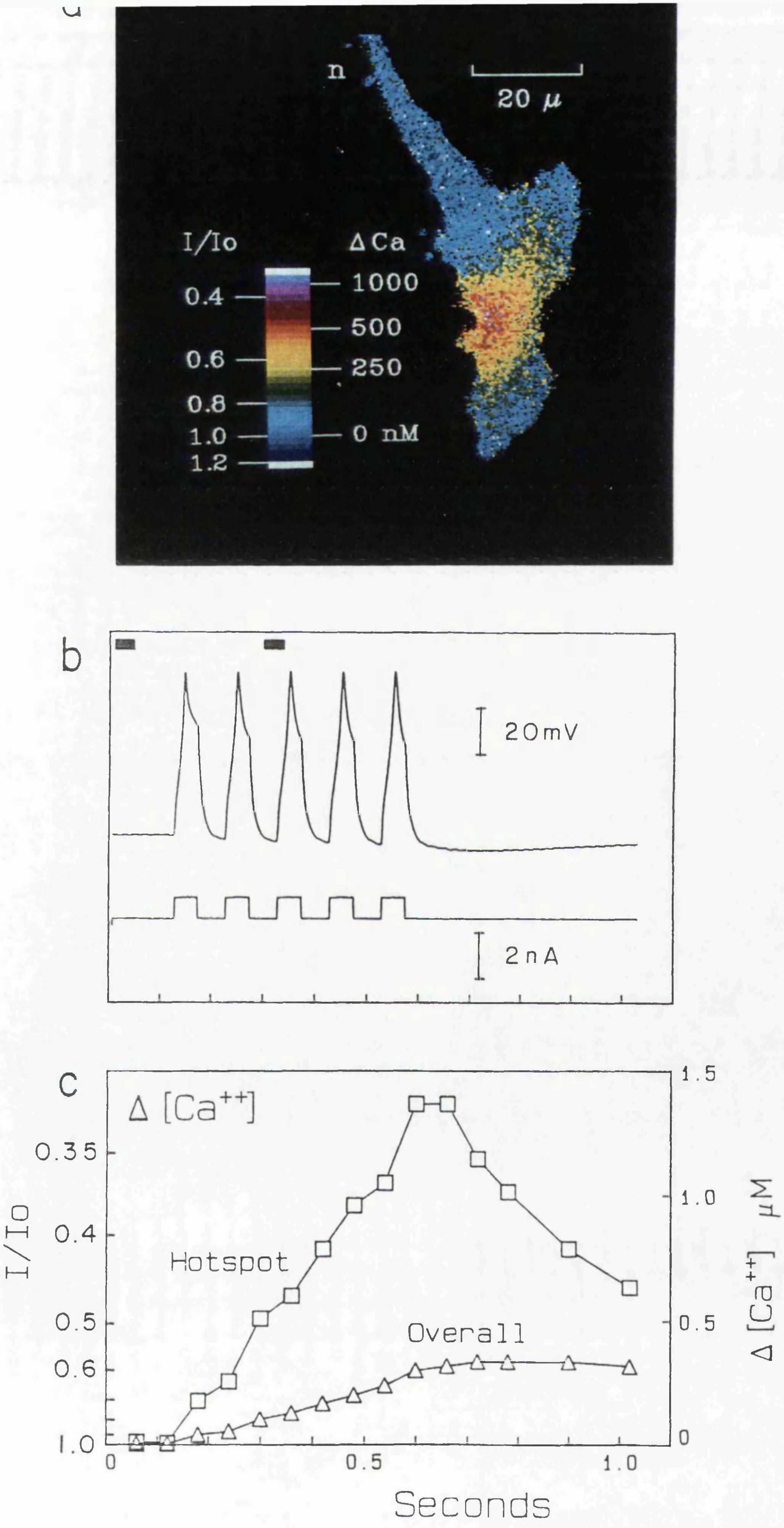
n
20 μ
I/Io
ΔCa
0.4
1000
500
0.6
250
0.8
1.0
0 nM
1.2
b
20mV
2nA
c
Δ [Ca++]
0.35
0.4
0.5
0.6
1.0
I/Io
Hotspot
Overall
1.5
1.0
0.5
0
Δ [Ca++] μM
0
0.5
1.0
Seconds

outgrowth and the centre of the hotspot diverged by 10° or less. In 7 out of the 11 growth cones studied, the growth cone margin grew out by 6±1 μm in the 4 minutes following action potential stimulation. In 5 of these, the site at which the greatest outgrowth occurred was close to a hotspot. The 7 growth cones in which margin outgrowth was seen contained a total of 12 hotspots, assuming 2-dimensional geometry, only 1/18th of all hotspots would be expected to lie in a particular 20° sector. Thus hotspots and margin advance were highly correlated $\chi^2 = 30.2$, $p<0.001$.

5.4 Discussion of results: the spatial distribution of voltage-gated calcium influx in the neuronal growth cone

Depolarization of the neuronal membrane activates calcium influx through voltage-gated calcium channels. Information about the spatial distribution of these channels is crucial for understanding neuronal function, because it will influence both the electrical activity, and the activation of second messenger systems within the cell. Many studies have shown that neurones exhibit gross calcium gradients upon depolarization, with $[Ca^{2+}]_i$ increasing more in regions remote from the soma (Bolsover and Spector, 1986; Kater *et al.*, 1988; Smith and Augustine, 1988; Tank *et al.*, 1988; Regehr *et al.*, 1989). This behaviour also seems to occur during development, with larger changes in $[Ca^{2+}]_i$ at the growth cone (Bolsover and Spector, 1986; Kater *et al.*, 1988). Tank *et al.*, (1988) have also reported more localized $[Ca^{2+}]_i$ hotspots within neurites which rise 70-80 nM above the uniform increase seen during action potentials. The present study demonstrates that highly localized $[Ca^{2+}]_i$ hotspots are present in neurobastoma growth cones and that they are produced by L-type calcium channel activation.

5.4.1 The mechanism of hotspot formation

$[Ca^{2+}]_i$ hotspots could be caused by clustering of L-type channels in the growth cone membrane. Alternatively a uniform distribution of calcium channels within the cell membrane could produce $[Ca^{2+}]_i$ hotspots by three possible mechanisms. First, hotspots might represent areas where Ca^{2+}-buffering capacity is low. Second, hotspots might lie under invaginations of the cell membrane that produce a locally high surface area/volume ratio. Third, Ca^{2+} influx might activate release of Ca^{2+} from internal stores that are distributed non-uniformly throughout the cytoplasm. Activation of calcium influx through T-type channels caused a smaller but uniform increase in $[Ca^{2+}]_i$. The fact that hotspots were never seen during calcium influx through T-type channels is inconsistent with the above models: hotspot models with uniform calcium channel distributions predict hotspot formation in the same location for calcium influx through both types of channel.

The uniform $[Ca^{2+}]_i$ change observed during activation of the T-type current does not rule out the possibility that hotspots seen during L-type current activation are caused by either an inhomogeneity of Ca^{2+} buffering or Ca^{2+}-induced Ca^{2+} release that only appears at high $[Ca^{2+}]_i$ levels. To test these possibilities, Cd^{2+} was used to reduce selectively L-type currents and hotspot $[Ca^{2+}]_i$ change. When the $[Ca^{2+}]_i$ changes during L- and T-type current activation were the same size (Fig. 5.2c), hotspots were still present during L- channel activation, ruling out a concentration dependent explanation. Thus it is highly likely that the hotspots are caused by non-uniform clustering of L-type channels within the growth cone membrane.

Once expressed, the L-type current density remained constant (Section 3.3.2) with time, that is the average number of L-type channels per unit area of the membrane remained constant as the cells increased in size and extended neurites. The finding that the number of hotspots per growth cone does not change with time in the differentiation medium may imply that maturing cells pack more and more L-type channels into a few discreet clusters in the growth cone. This hypothesis is consistent with the result that hotspot $[Ca^{2+}]_i$ rises more dramatically in older cells.

The morphological changes caused by hotspot activation will be discussed in the next chapter.

Chapter 6

Discussion

6.1 How do growth cones grow?

In the traditional view of growth cone growth, filopodia and membrane protrusions are extended and adhere to the substrate. These structures then contract, exerting force which pulls the growth cone forward (Bray, 1982). More recently Goldberg and Burmeister (1986) used electronically enhanced microscopy to study *Aplysia* growth cones growing *in vitro*. They considered the growth cone as being formed of a 'central region' containing organelles, and a 'distal region' of newly formed veils with few organelles. Goldberg and Burmeister (1989) proposed that forward growth occurred in three stages: protrusion, engorgement and consolidation. In the first step, protrusion, filopodia extended forward from the distal region, either into the liquid medium or along the substrate. The plasma membrane then advanced as flat featureless veils between filopodia which, act as a scaffold to define the pathway for veil advance. In the second step, engorgement, membranous organelles and cytoplasm move forward into some of the veils, converting them into a new 'central region'. The last phase, consolidation, involves the conversion of the proximal central region, which is characterized by random movement of organelles, into a cylindrical neurite with regular microtubule arrays and bidirectional fast axonal transport. This sequence of behaviour has also been seen in PC12 cells, rat sympathetic nerve cells (Aletta and Greene, 1988) and seems to fit N1E-115 growth cones (Fig. 4.2).

6.2 What are the molecular events underlying growth cone growth and neurite elongation?

The cytoskeleton has three distinct protein polymer components: actin filaments (also called microfilaments), intermediate filaments (also called neurofilaments in neurons) and microtubules. Neurofilaments are found in the highest amounts in mature neurons that have assumed a fixed shape and are therefore not thought to be important in developing neurons. Differences in the spatial distribution and biochemistry of the other two cytoskeletal components, microtubules and microfilaments, provide a key to the mechanisms involved in motility and growth during cell differentiation. Microtubules originate at microtubule organizing centres (centrosomes) at the cell body and extend in ordered arrays along the axon. The majority of microtubules terminate in the proximal region of the growth cone, only a few spread out into the lamellipodia (Forscher *et al.*, 1987). Microfilaments, in contrast, form a dense network in the growth cone and lamellipodia. Bundles of actin filaments radiate from the growth cone centre and form filopodia (Letourneau, 1983).

It is useful to distinguish between growth cone motility and neurite elongation. Motility seems to be actin-based while neurite elongation is more fundamentally dependent on microtubules. The sequence of events described in the Goldberg and Burmeister model provides a convenient framework in which to discuss the implications of the present results for a role of calcium in the molecular processes underlying growth cone behaviour.

During protrusion filopodia are extended. Actin bundles that make up filopodia form by rapid polymerization with monomer addition at the barbed (+) end. It is generally accepted that the energy for extension is derived from adenosine triphosphate (ATP), but the mechanism of extension has not been elucidated (Smith, 1988). In the presence of ATP actin does not act as a simple equilibrium polymer. This is because actin molecules possess an ATP binding site that governs polymerization and can hydrolyse ATP. The metabolically driven polymerization-depolymerization steady state reaction is capable of doing physical work (Hill and Krischner, 1982) and causes actin monomer treadmilling. The energy released by ATP hydrolysis is adequate to drive filopodial extension. Veil protrusion may involve a similar actin-driven motor, but with the actin forming a less ordered array.

Regulation of actin polymerization is highly dependent on several actin binding proteins (ABP), some of which are calcium dependent. One such ABP is gelsolin which regulates actin polymerization by three actions. Firstly it can cap actin filaments, which reduces access for polymerization. Secondly, by binding to g-actin, it forms a complex which acts as a nucleation site. Thirdly, gelsolin can side-bind to actin filaments and cause severing by weakening non-covalent actin-actin bonds (Forscher, 1989). Phosphatidylinositol 4, 5,-bisphosphate (PIP_2) also regulates gelsolin and a second ABP called profilin. Profilin binds to g-actin forming profilactin and reduces the concentration of free g-actin available for polymerization. PIP_2 binds to profilin, releasing g-actin and therefore increasing the rate of actin polymerization (Lassing and Lindberg, 1985).

Janmey *et al.* (1987) have shown that actin polymerization in the presence of gelsolin and PIP_2 is accelerated by the addition of EGTA. They proposed that this effect was caused by gelsolin binding PIP_2 thereby uncapping microfilaments. This stimulation of polymerization by a fall in $[Ca^{2+}]_i$ is consistent with the resumption of motility seen in Figure 4.6. Whatever the mechanism of filopodial extension it is likely that most of the basic components are present in many cell types since the transfection of GAP-43, a protein associated with neuronal growth and plasticity, induces the formation of filopodia in non-neuronal cells (Zuber *et al.*, 1989).

The actin binding protein (ABP), myosin, binds to actin filaments to form actomyosin. Actomyosin has been proposed as the motor for membrane veil and filopodial extension. This model has however, lost ground because antibody block (Höner *et al.*, 1988), and synthesis prevention, of myosin II have little effect on motility in *Dictyostelium* (DeLozanne and Spudich, 1987; Knecht and Loomis, 1987). However, myosin I which has two binding sites for actin may play a role in motility. A recent study has shown myosin I localized to the lamellipodia of *Dictyostelium* (Fukui *et al.*, 1989). Myosin I is regulated by phosphorylation of the light chain and thus could be modulated by second messenger-dependent kinases including calcium dependent kinases (Korn *et al.*, 1988).

Filopodial extension often occurred during motile advancing (Fig. 4.2), motile non-advancing and flattening behaviour (Fig. 4.4), but was absent at $[Ca^{2+}]_i$ levels above about 150 nM. Studies using calcium channel blockers and reduced extracellular calcium to lower $[Ca^{2+}]_i$ have shown reduced filopodial formation. The present results show that motile activity such as filopodial extension, veil formation and ruffling do occur at basal $[Ca^{2+}]_i$. The inhibition of filopodia formation and ruffling activity at high $[Ca^{2+}]_i$ (>150 nM) was probably caused by Ca^{2+}-induced cytoskeletal disruption and/or disassembly.

Freeman *et al.* (1985), using a novel vibrating probe to measure current density showed the presence of a calcium current entering the filopodia. They proposed that localized Ca^{2+} influx may cause localized vesicle fusion and filopodial extension. An early imaging study showed a correlation between local $[Ca^{2+}]_i$ elevation and filopodial extension (Connor, 1986); this suggested a role for a localized $[Ca^{2+}]_i$ elevation in triggering actin nucleation and polymerization and therefore, filopodia formation via calcium-dependent enzymes. In the same vein Goldberg (1988) proposed that veil extension might occur at regions of the growth cone where $[Ca^{2+}]_i$ was locally high. In the present investigation of unstimulated cells, $[Ca^{2+}]_i$ was not found to be elevated at the base of filopodia and was 5-10 nM lower in motile structures. When the acetoxymethyl ester (AM) of fura-2 was used to load the cells with dye, results similar to those reported by Connor (1986) were obtained (Fig. 4.8). It seems likely that Connor's result is an artifact caused by his method, and not some species-dependent difference. Malgaroli *et al.*, (1987) have suggested a mechanism for this artifact. When fura-2 is loaded by bathing cells in medium containing the membrane-permeable ester, fura-2 AM, intracellular organelles such as secretory and endocytotic vesicles load with dye (Almers and Neher, 1985; Malgaroli *et al.*, 1987). Regions of cytoplasm rich in organelles therefore appear to have locally high $[Ca^{2+}]_i$, even though the cytoplasmic $[Ca^{2+}]_i$ may be uniform. The perinuclear high-Ca^{2+} ring in the cell on the right of Figure 4.8 is characteristic of this type of artifact, and probably results from endocytosis of dye micelles (Malgaroli *et al.*, 1987). It is likely that the high-Ca^{2+} regions at the tip of growth cones loaded with fura-2 AM, but never seen in growth cones injected with fura-2, are a similar artifact since the leading edge of the growth cone is an active site of endocytosis (Bunge, 1977). Variation of apparent $[Ca^{2+}]_i$ was much greater in fura-2 AM-loaded growth cones compared with growth cones of cells injected with fura-2, possibly because of differences in the degree to which intracellular organelles loaded with dye.

Gross membrane veil protrusion occurs during flattening behaviour (Fig. 4.4) which can be caused by exposure of the growth cone to the calcium ionophore A23187 (Anglister *et al.*, 1982). These results indicate that elevated $[Ca^{2+}]_i$ promotes gross veil formation. Spreading of cells upon permissive substrates is related to the stickiness of the substrate and is thought to occur by an increase in cell-substrate adhesion sites. However, it is unlikely that raised $[Ca^{2+}]_i$ causes growth cone flattening by increasing cell-substrate adhesion because

Anglister *et al.* (1982) have shown that cell-substrate adhesion sites neither move nor increase in number during $[Ca^{2+}]_i$-induced flattening. Veil protrusion may occur by weakening of the actin network, producing a reduced elastic resistance to hydrostatic pressure in the cytoplasm (Smith, 1988). Such a model could explain $[Ca^{2+}]_i$-induced flattening since calcium activation of ABPs such as gelsolin and proteolytic enzymes such as calpain (Melloni and Pontremoli, 1989) could produce the necessary weakening of the actin network.

Several features indicate that veil formation during flattening is not a good model for veil outgrowth during steady forward growth. During growth veil formation is usually localized and directed (Fig. 4.2). Newly formed membrane veils have an ultrastructure consisting of planar sheets of actin filaments (Tosney and Wessells, 1983); this regular structure would not be expected if veil formation was produced by local breakdown of the actin lattice. Active ruffling of the growth cone margin seems to be important in growth and may represent the 'power stroke' which would occur if the membrane had adhered to the substrate. However, during flattening ruffling tended to be inhibited. Growth occurs at basal $[Ca^{2+}]_i$ and in motile membrane veils $[Ca^{2+}]_i$ tends to be 5-10 nM lower which is inconsistent with the hypothesis that elevated $[Ca^{2+}]_i$ triggers veil formation during normal forward growth. The thickness of the growth cone remains relatively constant during normal forward growth, unlike the gross structural changes seen in flattening growth cones. Lastly, veil protrusion is not promoted by treatment with cytochalasin, a drug that causes actin depolymerization by capping microfilaments (Forscher and Smith, 1988). Taken together these results argue against actin network breakdown as a mechanism for veil advance during growth.

It is possible that veil advance has the same motor as filopodial extension since a veil can be considered as a planar filopodium. Polymerization of this planar structure could provide the energy for extension. This model is consistent with the finding that veil formation is inhibited by cytochalasin. The involvement of myosin in veil motility is strongly suggested by the finding that ruffling is inhibited by butane dione monoxime, a specific actomyosin inhibitor (S. Bolsover and I. Spector, unpublished observations). However, since no steady spatial gradients are present in motile structures there must be other highly localized factors apart from $[Ca^{2+}]_i$ involved in the formation and regulation of filopodia and veils.

In contrast to its inhibitory effect on veil formation, cytochalasin treatment does promote engorgement, which is consistent with the hypothesis that organelles and cytoplasm move forward as a result of disassembly of the dense actin network. The translocation of organelles may occur simply by Brownian motion or by some transport system attached to microtubules or the remaining actin filaments. Myosin I is thought to be the motor for the actin-based transport system (Adams and Pollard, 1986). cAMP elevation has been shown to increase organelle transport in *Aplysia* growth cones (Forscher *et al.*, 1987). This points to the cAMP-dependent kinase as a possible regulator of myosin activity. Engorgement could also be promoted by a polymerization of microtubules that pushed the cytoplasm forward. This is probably not important during flattening since this occurs at a $[Ca^{2+}]_i$ level which is likely to inhibit microtubule polymerization.

During consolidation the proximal region of the growth cone is converted into a cylindrical neurite displaying predominately bidirectional fast axonal transport along linear arrays of microtubules (Goldberg and Burmeister, 1989). The boundary between the neurite and growth cone moves forward through an extension of the microtubule/neurofilament skeleton (Goldberg and Burmeister, 1986). In the present study, neurite elongation was the defining feature of the motile advancing group (Fig. 4.2). In this group $[Ca^{2+}]_i$ was low and not significantly different from that in the quiescent group (Fig. 4.9). Kater *et al.* (1988) have proposed that a rise in $[Ca^{2+}]_i$ from the concentration found in quiescent growth cones activates growth and motility. This model is not consistent with the findings in N1E-115 cells. Furthermore the correlation, in motile growth cones, between raised $[Ca^{2+}]_i$ and failure of the growth cone/neurite boundary to advance leads to the conclusion that raised $[Ca^{2+}]_i$ may inhibit extension of the microtubule/neurofilament cytoskeleton within the neurite. Such an inhibitory role for $[Ca^{2+}]_i$ is consistent with the observation that application of calcium channel blockers or a reduction of extracellular calcium promotes neurite extension (Mattson and Kater, 1987) since both the manipulations will reduce $[Ca^{2+}]_i$. *In vitro* studies of tubulin have shown that calcium interacts with calmodulin and microtubule associated proteins (MAPs) (Lee and Wolff, 1984) to inhibit microtubule elongation (Manalan and Klee, 1984). This inhibition is believed to act via a Ca^{2+}-calmodulin stimulated phosphorylation of MAP-2 and τ-factor (Yamamoto *et al.*, 1983). In contrast, cAMP-dependent phosphorylation of MAP-2 and microtubules enhances polymerization (Manalan and Klee, 1984), hence these two second messengers may to have antagonistic effects on tubulin polymerization at the growth cone/neurite boundary. Thus, is possible that changing the level of cAMP could alter the absolute calcium sensitivity of the growth cone.

Retraction of the growth cone towards the soma, which occurred only at high $[Ca^{2+}]_i$ (>300 nM) must involve the disassembly of the neurite cytoskeleton. This observation was consistent with reports that microinjection of Ca^{2+} and Ca^{2+}-saturated calmodulin into the cytoplasm (Kiehart, 1981; Keith *et al.*, 1983) or application of the calcium ionophore A23187 induced microtubule disassembly (Schliwa, 1976). It therefore appears that the degree of microtubule polymerization in the growth cone is highly dependent on $[Ca^{2+}]_i$ with low $[Ca^{2+}]_i$ favouring polymerization and advance of the growth cone/neurite boundary and high $[Ca^{2+}]_i$ favouring depolymerization and growth cone retraction. Microtubules in the growth cone may be more labile than neurite microtubules. Bamburg *et al.* (1986) found that microtubules at the growth cone were 100-fold more sensitive to the depolymerizing drug colcemid than were microtubules in either the neurite or the cell body. Spatial differences in microtubule sensitivity to depolymerization may be due to post-translational modifications to the tubulin subunits (Schultz *et al.*, 1987).

Kater *et al.* (1988) proposed that a rise in $[Ca^{2+}]_i$ above the level found in quiescent growth cones promotes motility and growth. The results of this study are not consistent this idea. The difference in conclusions about the role of calcium is probably caused by three factors. The first, and probably least important, may result from the method of dye loading used. The second may stem from differences in data interpretation. Growth cones classed as motile advancing in this study fit the accepted pattern of growth cone growth (Bray, 1982; Goldberg and Burmeister, 1989). It is possible that Connor (1986) and Cohan *et al.* (1987) may have included within their 'growing' category growth cones that, in this study, would have been classed as belonging to another behavioural state. In this study growth cones in which the leading edge advanced were classed as either motile non-advancing or flattening, unless the growth cone/neurite junction also moved forward. Only that subgroup of motile growth cones in which the growth cone/neurite junction moved forward was considered to be truly growing. In contrast, Cohan *et al.* (1987) did not distinguish between growth cones in which the boundary between the neurite and growth cone moved forward, and those in which the boundary did not move. If the data from the motile advancing, motile non-advancing and flattening growth cones in this study are combined then $[Ca^{2+}]_i$ is significantly higher in the broad motile group than the quiescent group (motile: R=1.49±0.03, n=37, $[Ca^{2+}]_i$=94±6 nM; quiescent: R=1.29±0.04, n=8, $[Ca^{2+}]_i$=55±7 nM, $p<0.001$). Treated in this way the data are in agreement with Cohan *et al.* (1987) in that the $[Ca^{2+}]_i$ is higher in motile growth cones. However, since motility (extension and movement of veils, ruffles and filopodia) was observed equally in motile advancing growth cones at the lowest measured $[Ca^{2+}]_i$ and in motile non-advancing growth cones at higher $[Ca^{2+}]_i$ it is unlikely that raised $[Ca^{2+}]_i$ causes motility. A third reason for the conflicting conclusion may arise from species-dependent differences in the $[Ca^{2+}]_i$ sensitivity of the cytoskeleton and/or the use of transformed cells in the present study. However, the conclusions drawn here are unlikely to be limited to neuroblastoma cells and could be applicable to a wide range of neurons. It is known for example that in *Xenopus* spinal neurons growth cone growth and neurite elongation occurs only at the lowest measured $[Ca^{2+}]_i$ (Dr K.R. Robinson, unpublished observations).

Expression of T-type Ca^{2+} channels is correlated with neurite extension. The simplest conclusion from this type of correlation is that Ca^{2+} influx through the channels stimulates neurite growth. This proposal is similar to that put forward by Kater *et al.* (1988). In a previous study that correlated calcium currents with neuronal development it was the T-type current that seemed to be important early in differentiation (McCobb *et al.*, 1989). Such models are difficult to reconcile with the finding here that neurite elongation occurs only at low $[Ca^{2+}]_i$. Activation of T-type currents produces only very small changes of $[Ca^{2+}]_i$ at the growth cone (Fig. 5.2). One could argue that if Ca^{2+} influx was necessary for neurite elongation evolution would favour the early expression of L-type channels, which produce much larger $[Ca^{2+}]_i$ changes. Neurons can extend neurites in the absence of Ca^{2+} and in the presence of calcium channel blockers, (Blixby and Spitzer, 1984; Mattson *et al.*, 1988) which is inconsistent with the hypothesis that calcium influx though voltage-gated channels is essential for neurite elongation. While a basal level of [Ca^{2+}] is essential for neurite elongation, voltage-gated Ca^{2+} influx seems to be very important in growth cone navigation, innervation (Suarez-Isla *et al.*, 1984) and possibly bifurcation (all discussed in the next Section). Thus calcium currents may be essential *in vivo*, but redundant under *in vitro* conditions where the are no external stimuli that can alter membrane potential and therefore [Ca^{2+}]$_i$. A number of other possibilities could explain the correlation of calcium channel expression and neurite extension. A trigger that causes differentiation must induce the expression of a large number of proteins. The T-type channel protein may simply be one of those expressed as a result of the induction of differentiation. More speculatively, T-type channels may play some role other than as calcium ionophores; perhaps acting as membrane attachment sites for the cytoskeleton in a manner analogous to the role of the band three protein in red blood cells (Alberts *et al.*, 1989).

6.3 How do growth cones navigate?

The functional properties of the nervous system depend critically on the complex network of neuronal connections created during development. The accuracy with which axons select pathways and the mechanism underlying their guidance to precise targets has been the subject of much debate. The growth cone at the tip of extending neurites acts as a sensory device, exploring the immediate environment by extending and retracting filopodia. The growth cone reacts to both extrinsic and intrinsic information. Choices made by the growth cone are central to nervous system development and therefore factors that influence growth cone behaviour are of importance. Extrinsic factors that are thought to influence growth cones *in vivo* can be divided into three groups:

adhesion substrates, neuronal guide posts, and diffusible factors.

6.3.1 Extrinsic factors: adhesive substrates

Adhesion molecules are classified by their location. Extracellular matrix (ECM) adhesion molecules, such as laminin and fibronectin, are usually glycoproteins. Laminin is transiently expressed often in linear arrays and is thought to act as an adhesion pathway for axonal guidance (Letourneau *et al.*, 1988). Adhesion pathways are thought to be especially important for pioneer axons that have no existing fibers to grow along. Laminin promotes axonal extension by interacting with axonal transmembrane glycoproteins that are members of the integrin family of receptors (Bozyczko and Horwitz, 1986; Buck and Horwitz, 1987). Integrins such as the fibronectin receptor link the cytoskeleton to the ECM and may act as organizing centres for the actin network (Alberts *et al.*, 1989).

N-cadherin and N-CAM (neuronal cell adhesion molecule), a second type of adhesion molecule, are located in neuronal membranes. They are integral membrane glycoproteins and are, respectively, the most abundant Ca^{2+}-dependent and Ca^{2+}-independent adhesion molecules present in vertebrate neuronal cells (Dodd and Jessell, 1988). Both of these molecules are homophilic, that is they interact with the same molecular species on opposing surfaces of neighbouring cells. The relatively uniform distribution of the two molecules argues against their playing a major role in axonal guidance.

Proteins such as L1, G4, F11, neurofascin, TAG-1 and TRAP are other examples of integral membrane protein and where defined seem to work by a homophilic mechanism. They are restricted to the axon and may promote selective fasciculation (Dodd and Jessell, 1988).

A third category is membrane proteins that are inhibitory. Oligodendrocytes express two surface proteins of molecular weight 35 KD and 250 KD that inhibit

CNS growth cones (Caroni and Schwab, 1988a). Antibodies to these proteins neutralize their inhibitory effects and allow regrowth (Caroni and Schwab, 1988b). Inhibitory proteins are also expressed on axonal surfaces and this may contribute to selective fasciculation.

6.3.2 Neuronal guide-posts

Pathway guidance has been extensively studied in the grasshopper (Bastiani *et al.*, 1985). Limb bud pioneer axons grow towards the CNS by precisely defined zig-zag paths. The path is defined by a chain of specific 'guide post' cells with which the growth cone makes transient gap junctions. Having made contact with one cell in the chain, pioneer growth cones extend filopodia for up to 100 μm in order to reach the next guide-post cell. Filopodia that make contact are stabilized and guide the growth cone to the next cell. If a guide-post cell is destroyed by a laser beam before the growth cone has reached it the growth cone becomes disoriented (Bentley and Caudy, 1983). Growth cones behind the pioneer axon follow the pioneer by axonal contact guidance.

6.3.3 Diffusible factors

Growth cones are sensitive to gradients of diffusible factors. As diffusible factors appear to operate over short distances (100-300 μm) (Dodd and Jessell, 1988) it is likely that they are important at specific locations where major decisions are made. A role for diffusible factors *in vivo* has been demonstrated in the spinal cord of embryonic rats. Growth cones of commissural neurons grow down to the floor plate, a specialized set of neuroepithelial cells at the ventral midline. Floor plate cells secrete a diffusible factor distinct from nerve growth factor (NGF) and laminin, that evokes a change in the direction of outgrowth of the commissural axons but does not affect other embryonic spinal cord axons (Tessier-Lavigne *et al.*, 1988). A chemotrophic factor distinct from NGF appears to guide trigeminal sensory axons to their peripheral target, the maxillary arch

(Lumsden and Davies, 1983).

Gunderson and Barrett (1980) showed that growth cones of chick sensory neurons grow towards a source of NGF *in vitro*. Growth cones also grew towards sources of dibutyryladenosine 3',5'-cyclic monophosphate (dBcAMP), guanosine 3',5'-cyclic monophosphate (cGMP) and calcium, although the response to calcium requires the presence of the calcium ionophore A23187 in the bathing medium. These results show that spatial gradients of intracellular cAMP, cGMP and Ca^{2+} could play a role in the turning response to NGF. Calcium could act by turning on enzymes such as gelsolin and calpain in areas of the cytoplasm where $[Ca^{2+}]_i$ is highest. This would cause a disruption of the actin network on the side facing the extracellular calcium source. Membrane veil formation, which can be considered as localized flattening, would therefore be promoted in the region where $[Ca^{2+}]_i$ is highest. The normal process of engorgement and consolidation would then act to convert the new veil into neurite.

6.3.4 Are intracellular $[Ca^{2+}]_i$ gradients likely to be important *in vivo*?

Voltage gated calcium influx during electrical activity produces gross $[Ca^{2+}]_i$ gradients in neurons (Kater *et al.*, 1988; Smith and Augustine, 1988; Tank *et al.*, 1988; Regehr *et al.*, 1989). Previous workers have also shown that calcium channels are present at the growth cone (Lipscombe *et al.*, 1988). The present study demonstrates that L-type and T-type calcium channels occur in neuroblastoma growth cones and that the two channel types have different spatial distributions in the growth cone membrane. T-type channels are uniformly distributed and the change in $[Ca^{2+}]_i$ during activation is small (Fig 5.1b). This rules out their involvement in a $[Ca^{2+}]_i$-induced turning response. L-type channels on the other hand, are highly localized in a limited number of clusters on the growth cone membrane (mean of 1.9 clusters/growth cone). Activation of L-channel clusters by action potentials produces highly localized $[Ca^{2+}]_i$ hotspots.

On average just 12 action potentials raised $[Ca^{2+}]_i$ at the hotspot to micromolar levels. This is almost certainly an underestimate of the calcium change for two reasons. First, although the buffering capacity of the growth cone cytosol is unknown it is likely that fura-2 will buffer $[Ca^{2+}]_i$ changes significantly at the dye concentrations used. Second, the poor horizontal and vertical resolution of the fluorescence microscope will overestimate the volume over which the $[Ca^{2+}]_i$ changes occurred and therefore underestimate the $[Ca^{2+}]_i$ changes at the true hotspot.

The micromolar levels of $[Ca^{2+}]_i$ produced during electrical activity will activate Ca^{2+}-dependent enzymes at the site of the hotspot. Examples include gelsolin which severs, caps and nucleates actin filaments (Forscher, 1989) and proteolytic enzymes such as calpain (Melloni and Pontremoli, 1989). Localized activation of such proteins within the growth cone explains both the localized membrane outgrowth seen after activation of the hotspot by action potentials and the high spatial correlation between the site of the hotspots and base of processes that extend from the growth cone. The location of calcium channel clusters on the growth cone is therefore likely to influence the direction of growth after depolarization. If extrinsic factors could modulate the spatial distribution of channel clusters, this would provide a powerful voltage-dependent mechanism for controlling growth cone direction. Channels are probably held in clusters by attachment to the growth cone cytoskeleton so any alteration in their spatial distribution would be likely to involve changes in the calcium channel-cytoskeleton attachment.

Developing neurites express neurotransmitter receptors (Lipton and Kater, 1989). *Helisoma* growth cones respond to the neurotransmitter, serotonin, by an elevation of $[Ca^{2+}]_i$, that in turn inhibits neurite elongation (Cohan *et al.*, 1987). Neurotransmitters are capable of activating different spatial distributions of calcium (Cheek *et al.*, 1989) in chromafin cells by causing either calcium influx or IP_3-dependent calcium release. If similar pathways occur in growth cones, different transmitters could encode a series of commands. Neurotransmitters that depolarize the growth cone may induce a turning response since L-type channel clusters and therefore margin outgrowth are asymmetrically distributed. Transmitters that activate the phosphoinositol pathway will influence actin polymerization via profilin and gelsolin binding.

6.3.5 Intrinsic factors: the cytoskeleton

The initial direction of axonal extension of neurons may depend on the position of microtubule organizing centres. After cell division, neuroblastoma sister cells show a striking resemblance to one another when grown with no external information to determine shape (Solomon, 1979). This implies that some intrinsic cytoskeletal memory is present. A good analogy is the shape of a certain species of tree, no two trees of that species are the same but they all have a shape that conforms to a recognizable intrinsic pattern. In neurons it is difficult to know how important this type of result is since it may be totally overridden by extrinsic factors *in vivo*. However, the characteristic shape of the dendritic tree of hippocampal pyramidal neurons *in vivo* is maintained when the cells are grown on a uniform substrate *in vitro* (Banker and Cowan, 1979). The pattern of dendritic aborization in pyramidal cells is the same in cells differentiating *in situ* in the cortex and in cells transplanted to the cerebellum (Das, 1975). These results argue strongly that some growth characteristics such as the frequency of bifurcation are controlled by an intrinsic mechanism. The cytoskeletal makeup of the cell may store this type of information: properties like bifurcations/process length could arise from simple mechanical properties. However, electrical activity may also be important.

6.3.6 Electrical activity

Cell-specific differences in the expression of voltage and ligand gated ion channels may be responsible for some of the intrinsic determination of neuronal shape. Electrical excitability is strongly correlated with neuronal differentiation, N1E-115 cells with processes always have T-type currents (Fig. 3.2a) and usually L-type currents (Fig. 3.2b). Calcium influx into the growth cone is highly likely to influence the shape of the dendritic tree since it will influence growth rate (Blixby and Spitzer, 1984) and cause asymmetrical margin outgrowth. Process outgrowth caused by activation of hotspots at two locations on the growth cone may induce a bifurcating morphology. It is possible therefore that electrical activity could trigger neurite bifurcation in growth cones with more than one hotspot if both processes continued to grow.

6.4 Are $[Ca^{2+}]_i$ hotspots precursors to active zones?

Active zones are specialized regions of the presynaptic membrane which are thought to be the site of vesicle fusion. Studies using freeze-fracture electron microscopy have shown a high density of transmembrane particles at the active zone (Heuser *et al.*, 1979). Pumplin *et al.* (1981) have proposed that they are calcium channels clusters. The present study demonstrates that there is a cellular mechanism for clustering L-type calcium channels. Insertion of channels into the clusters may occur during differentiation since hotspot $[Ca^{2+}]_i$ increased over the 7 day period studied. The changes at the hotspot could also represent the refinement of a highly specialized region for vesicle fusion. The size of the channel clusters may be comparable to the synaptic active zone. The hotspot dimensions are likely to be smaller than the measured value which was the same as the resolution of the microscope. Thus growth cone L-channel clusters may be the precursors of synaptic active zones. However this is purely speculative and it must be noted that N1E-115 neuroblastoma cells do not form synapses.

6.5 How important is $[Ca^{2+}]_i$ to growth cone growth? A summary

There are two main conclusions from this study. First, in an isolated environment with no external stimuli any elevation of $[Ca^{2+}]_i$ above the basal level inhibits neurite elongation. Second, voltage-gated calcium influx seems to be a very important factor in the transduction of external stimuli. Electrical activity activates L-type channel clusters which produce highly localized $[Ca^{2+}]_i$ hotspots in the neuronal growth cone. Micromolar levels of $[Ca^{2+}]_i$ at the hotspot induce localized membrane outgrowth. The asymmetric distribution of hotspots provides a mechanism for triggering turning of electrically active neurites, and could have a crucial role during development.

References

Adams, R.J. and Pollard, T.D. (1986). Propulsion of organelles isolated from the *Acanthamoeba* along actin filaments by myosin I. Nature 322, 754-756.

Agard, D.A. (1984). Optical sectioning microscopy: cellular architecture in three dimensions. Annual Reviews of Biophysics and Bioengineering 13, 191-219.

Alberts, B., Bray, D., Lewis, J., Raff, M., Roberts, K. and Watson, J.D. (1989). Molecular Biology of the Cell, 2ed edn. Garland: New York.

Aletta, J.M. and Greene, L.A. (1988). Growth cone configuration and advance: A time-lapse study using video-enhanced differential interference contrast microscopy. Journal of Neuroscience 8, 1425-1435.

Almers, W. and Neher, E. (1985). The calcium signal from Fura-2 loaded mast cells depends strongly on the method of dye loading. FEBS Letters 192, 13-18.

Alvarez-Leefmans, F.J., Rink, T.J. and Tsien, R.Y. (1981). Free calcium ions in neurones of *Helix aspersa* measured with ion-selective micro-electrodes. Journal of Physiology 315, 531-548.

Anglister, L., Farber, I.C., Shahar, A. and Grinvald, A. (1982). Localization of voltage-sensitive calcium channels along developing neurites: their possible role in regulating neurite elongation. Developmental Biology 94, 351-365.

Argiro, V., Bunge, M.B. and Johnson, M.I. (1985). A quantitative study of growth cone filopodial extension. Journal of Neuroscience Research 13, 149-162.

Baccaglini, P.I. (1978). Action potentials of embryonic dorsal root ganglion neurones in *Xenopus* tadpoles. Journal of Physiology 283, 585-604.

Bamburg, J.R., Bray, D. and Chapman, K. (1986). Assembly of microtubules at the tip of growing axons. Nature 321, 788-790.

Banker, G.A. and Cowan, W.M. (1979). Further observations on hippocampal neurons in dispersed cell culture. Journal of Comparative Neurology 187, 469-494.

Bastiani, M.J., Doe, C.Q., Helfand, S.L. and Goodman, C.S. (1985). Neuronal specificity and growth cone guidance in grasshopper and *Drosophila* embryos. Trends in Neurosciences 8, 257-266.

Baylor, S.M. and Hollingworth, S. (1988). Fura-2 calcium transients in frog skeletal muscle fibres. Journal of Physiology 403, 151-192.

Bentley, D. and Caudy, M. (1983). Pioneer axons lose directed growth after selective killing of guidepost cells. Nature 304, 62-65.

Bentley, D. and Toroian-Raymond, A. (1986). Disoriented pathfinding by pioneer neurone growth cones deprived of filopodia by cytochalasin treatment. Nature 323, 712-715.

Berridge, M.J. and Irvine, R.F. (1984). Inositol triphosphate, a novel second messenger in cellular signal transduction. Nature 312, 315-321.

Berridge, M.J. and Irvine, R.F. (1989). Inositol phosphates and cell signalling. Nature 341, 197-205.

Blaustein, M.P. (1988). Calcium transport and buffering in neurones. Trends in Neurosciences 11, 438-443.

Blixby, J.L. and Spitzer, N.L. (1984). Early differentiation of vertebrate spinal neurons in the absence of voltage-dependent Ca^{2+} and Na^{+} influx. Developmental Biology 106, 89-96.

Bolsover, S.R. (1986). Two components of voltage-dependent calcium influx in mouse neuroblastoma cells: measurement with Arsenazo III. Journal of General Physiology 88, 149-165.

Bolsover, S.R., Gilbert, S. and Spector, I. (1988). Motility at the growth cone of N1E-115 neuroblastoma cells: effect of Ca++ injection. Journal of Physiology 407, 86P.

Bolsover, S.R. and Spector, I. (1986). Measurements of calcium transients in the soma, neurite and growth cone of single cultured neurons. Journal of Neuroscience 6, 1934-1940.

Bozyczko, D. and Horwitz, A.F. (1986). The participation of a putative cell surface receptor for laminin and fibronectin in peripheral neurite extension. Journal of Neuroscience 6, 1241-1251.

Bray, D. (1970). Surface movements during the growth of single explanted neurons. Proceedings of the National Academy of Sciences (USA) 65, 905-910.

Bray, D. (1982). The mechanism of growth cone movements. Neurosciences Research Program Bulletin 20, 821-829.

Bray, D. (1987). Growth cones: do they pull or are they pushed?. Trends in Neurosciences 10, 431-434.

Bray, D. and Bunge, M.B. (1973). The Growth Cone in Neurite Extension. Ciba Foundation Symposium 14, pp 195-209, Elsevier: Amsterdam.

Buck, C.A. and Horwitz, A.F. (1987). Integrin, a transmembrane glycoprotein complex mediating cell-substratum adhesion. Journal of Cell Science suppl. 8, 231-250.

Bulmer, M.G. (1967). Principles of Statistics, 2ed edn. p214. Oliver & Boyed: Edinburgh.

Bunge, M.B. (1977). Initial endocytosis of peroxidase or ferritin by growth cones of cultured nerve cells. Journal of Neurocytology 6, 407-439.

Caroni, P. and Schwab, M.E. (1988a). Two membrane protein fractions from rat central myelin with inhibitory properties for neurite growth and fibroblast spreading. Journal of Cell Biology 106, 1281-1288.

Caroni, P. and Schwab, M.E. (1988b). Antibody against myelin-associated inhibitor of neurite growth neutralizes non-permissive substrate properties of CNS white matter. Neuron 1, 85-96.

Carrington, W.A., Fogarty, K.E. and Fay, F.S. (1990). Deconvolution in 3D confocal microscopy. Journal of Microscopy, in press.

Chad, J.E. and Eckert, R. (1986). An Enzymatic Mechanism for Calcium Current Inactivation in Dialysed *Helix* Neurones. Journal of Physiology 378, 31-51.

Chalazonitis, A. and Greene, L.A. (1974). Enhancement in excitability properties of mouse neuroblastoma cells cultured in the presence of dibutyryl cyclic AMP. Brain Research 72, 340-345.

Cheek, T.R., O'Sullivan, A.J., Moreton, R.B., Berridge, M.J. and Burgoyne, R.D. (1989). Spatial localization of the stimulus-induced rise in cytosolic Ca^{2+} in bovine adrenal chromaffin cells: distinct nicotinic and muscarinic patterns. FEBS Letters 247, 429-434.

Cohan, C.S., Connor, J.A. and Kater, S.B. (1987). Electrically and chemically mediated increases in intracellular calcium in neuronal growth cones. Journal of Neuroscience 7, 3588-3599.

Cohan, C.S. and Kater, S.B. (1986). Suppression of neurite elongation and growth cone motility by electrical activity. Science 232, 1638-1640.

Connolly, J.L., Seeley, P.J. and Greene, L.A. (1985). Regulation of growth cone morphology by nerve growth factor: a comparative study by scanning electron microscopy. Journal of Neuroscience Research 13, 183-198.

Connor, J.A. (1986). Digital imaging of free calcium changes and of spatial gradients in growing processes in single, mammalian central nervous system cells. Proceedings of the National Academy of Sciences (USA) 83, 6179-6183.

Das, G.D. (1975). Differentiation of dendrites in transplanted neuroblasts in the mammalian brain. Advances in Neurobiology 12, 181-199.

De Lozanne, A. and Spudich, J.A. (1987). Disruption of the *Dictyostelium* myosin heavy chain gene by homologous recombination. Science 236, 1086-1091.

Dodd, J. and Jessell, T.M. (1988). Axon guidance and the patterning of neuronal projections in vertebrates. Science 242, 692-699.

Fawcett, J.W., Rokos, J. and Bakst, I. (1989). Oligodendrocytes repel axons and cause axonal growth cone collapse. Journal of Cell Science 92, 93-100.

Fay, F.S., Carrington, W. and Fogarty, K.E. (1989). Three-dimensional molecular distribution in single cells analysed using the digital imaging microscope. Journal of Microscopy 153, 133-149.

Fenwick, E.M., Marty, A. and Neher, E. (1982). A patch-clamp study of bovine chromaffin cells and of their sensitivity to acetylcholine. Journal of Physiology 331, 577-597.

Forscher, P. (1989). Calcium and phosphoinositide control of cytoskeletal dynamics. Trends in Neurosciences 12, 468-474.

Forscher, P., Kaczmarek, L.K., Buchanan, J. and Smith, S.J. (1987). Cyclic AMP induces changes in distribution and transport of organelles within growth cones of *Aplysia* bag cell neurons. Journal of Neuroscience 7, 3600-3611.

Forscher, P. and Smith, S.J. (1988). Actions of cytochalasins on the organization of actin filaments and microtubules in a neuronal growth cone. Journal of Cell Biology 107, 1505-1516.

Fox, A.P., Nowycky, M.C. and Tsien, R.W. (1987). Single-channel recordings of three types of calcium channels in chick sensory neurones. Journal of Physiology 394, 173-200.

Freeman, J.A., Manis, P.B., Snipes, G.J., Mayes, B.N., Samson, P.C., Wikswo, J.P. and Freeman, D.B. (1985). Steady growth cone currents revealed by a novel vibrating probe: A possible mechanism underlying neurite growth. Journal of Neuroscience Research 13, 257-283.

Fukui, Y., Lynch, T.J., Brzeska, H. and Korn, E.D. (1989). Myosin I is located at the leading edges of locomoting *Dictyostelium* amoebae. Nature 341, 328-331.

Gillespie, J.I. and Meves, H. (1980). The time course of sodium inactivation in squid giant axons. Journal of Physiology 299, 289-307.

Goldberg, D.J. (1988). Local role of Ca^{2+} in formation of veils in growth cones. Journal of Neuroscience 8, 2596-2605.

Goldberg, D.J. and Burmeister, D.W. (1986). Stages in axon formation: observations of growth of *Aplysia* axons in culture using video-enhanced contrast differential interference contrast microscopy. Journal of Cell Biology 103, 1921-1931.

Goldberg, D.J. and Burmeister, D.W. (1989). Looking into growth cones. Trends in Neurosciences 12, 503-506.

Grant, N.J., Oriol-Audit, C. and Dickens, M.J. (1983). Supramolecular forms of actin induced by polyamines: an electron microscopic study. European Journal of Cell Biology 30, 67-73.

Grynkiewicz, G., Poenie, M. and Tsien, R.Y. (1985). A new generation of Ca^{2+} indicators with greatly improved fluorescence properties. Journal of Biological Chemistry 260, 3440-3450.

Gundersen, R.W. and Barrett, J.N. (1980). Characterization of the turning response of dorsal root neurites toward nerve growth factor. Journal of Cell Biology 87, 546-554.

Hamill, O.P., Marty, A., Neher, E., Sakmann, B. and Sigworth, F.J. (1981). Improved patch-clamp techniques for high-resolution current recording from cells and cell-free membrane patches. Pflügers Archiv European Journal of Physiology 391, 85-100.

Harrison, R.G. (1907). The living developing nerve fiber. Anatomical Record 1, 116-118.

Harrison, R.G. (1910). The outgrowth of the nerve fiber as a model of protoplasmic movement. Journal of Experimental Zoology 9, 787-846.

Heuser, J.E., Reese, T.S., Dennis, M.J., Jan, Y., Jan, L. and Evans, L. (1979). Synaptic vesicle exocytosis captured by quick freezing and correlated with quantal transmitter release. Journal of Cell Biology 81, 275-300.

Hill, T.L. and Kirschner, M.W. (1982). Subunit treadmilling of microtubules or actin in the presence of cellular barriers: possible conversion of chemical free energy into mechanical work. Proceedings of the National Academy of Sciences (USA) 79, 490-494.

Höner, B., Citi, S., Kendrick-Jones, J. and Jockusch, B.M. (1988). Modulation of cellular morphology and locomotory activity by antibodies against myosin. Journal of Cell Biology 107, 2181-2189.

Jacob, R., Merritt, J.E., Hallam, T.J. and Rink, T.J. (1988). Repetitive spikes in cytoplasmic calcium evoked by histamine in human endothelial cells. Nature 335, 40-45.

Janmey, P.A., Kazuko, I., Yin, H.L. and Stossel, T.P. (1987). Phosphoinositide micelles and polyphosphoinositide-containing vesicles dissociate endogenous gelsolin-actin complexes and promote actin assembly from the fast growing end of actin filaments blocked by gelsolin. Journal of Biological Chemistry 262, 12228-12236.

Jones, O.T., Kunze, D.L. and Angelides, K.J. (1989). Localization and mobility of ω-conotoxin-sensitive Ca^{2+} channels in hippocampal CA1 neurons. Science 244, 1189-1193.

Kalil, R.E., Dublin, M.W., Scott, G. and Stark, L.A. (1986). Elimination of action potentials blocks the structural development of retinogeniculate synapses. Nature 323, 156-158.

Kater, S.B., Mattson, M.P., Cohan, C. and Connor, J. (1988). Calcium regulation of the neuronal growth cone. Trends in Neurosciences 11, 315-321.

Keith, C., DiPaola, M., Maxfield, F.R. and Shelanski, M.L. (1983). Microinjection of Ca^{2+}-calmodulin causes a localized depolymerization of microtubules. Journal of Cell Biology 97, 1918-1924.

Kiehart, D.P. (1981). Studies on the in vivo sensitivity of spindle microtubules to calcium ions and evidence for a vesicular calcium-sequestering system. Journal of Cell Biology 88, 604-617.

Kimhi, Y., Palfrey, C., Spector, I., Barak, Y. and Littauer, U.Z. (1976). Maturation of neuroblastoma cells in the presence of dimethylsulfoxide. Proceedings of the National Academy of Sciences (USA) 73, 462-466.

Knecht, D.A. and Loomis, W.F. (1987). Antisense RNA inactivation of myosin heavy chain gene expression in *Dictyostelium discoideum.* Science 236, 1081-1086.

Konishi, M., Olson, A., Hollingworth, S. and Baylor, S.M. (1988). Myoplasmic binding of Fura-2 investigated by steady-state fluorescence and absorbance measurements. Biophysical Journal 54, 1089-1104.

Korn, E.D., Atkinson, M.A.L., Brzeska, H., Hammer, J.A., Jung, G. and Lynch, T.L. (1988). Structure-function studies on *Acanthamoeba* myosin IA, IB, and II. Journal of Cellular Biochemistry 36, 37-50.

Kostenko, M.A., Musienko, V.S. and Smolikhina, T.I. (1983). Ca^{2+} and pH affect the neurite formation in cultured mollusc isolated neurones. Brain Research 276, 43-50.

Kuffler, S.W., Nicholls, J.G. and Martin, A.R. (1984). From Neuron to Brain: a Cellular Approach to the Function of the Nervous System, 2ed edn, pp. 12-13. Sinauer Associates: Sunderland MA.

Lai, F.A., Erickson, H.P., Rousseau, E., Liu, Q.-.Y. and Meissner, G. (1988). Purification and reconstitution of the calcium release channel from skeletal muscle. Nature 331, 315-319.

Landis, S.C. (1983). Neuronal growth cones. Annual Review of Physiology 45, 567-580.

Lansman, J.B., Hess, P. and Tsien, R.W. (1986). Blockade of current through single calcium channels by Cd^{2+}, Mg^{2+} and Ca^{2+}. Journal of General Physiology 88, 321-347.

Lassing, I. and Lindberg, U. (1985). Specific interaction between phosphatidylinositol 4,5-bisphosphate and profilactin. Nature 314, 472-474.

Lee, Y.C. and Wolff, J. (1984). Calmodulin binds to both microtubule-associated protein 2 and Tau proteins. Journal of Biological Chemistry 259, 1226-1230.

Letourneau, P.C. (1983). Differences in the organization of actin in the growth cones compared with the neurites of cultured neurons from chick embryos. Journal of Cell Biology 97, 963-973.

Letourneau, P.C., Madsen, A.M., Palm, S.L. and Furcht, L.T. (1988). Immunoreactivity for laminin in the developing ventral longitudinal pathway of the brain. Developmental Biology 125, 135-144.

Levi-Montalcini, R., Meyer, H. and Hamburger, V. (1954). *In vitro* experiments on the effects of mouse sarcomas 180 and 37 on the spinal and sympathetic ganglia of chick embryo. Cancer Research 14, 49-57.

Lipscombe, D., Madison, D.V., Poenie, M., Reuter, H., Tsien, R.Y. and Tsien, R.W. (1988). Spatial distribution of calcium channels and cytosolic calcium transients in growth cones and cell bodies of sympathetic neurons. Proceedings of the National Academy of Sciences (USA) 85, 2398-2402.

Lipton, S.A. and Kater, S.B. (1989). Neurotransmitter regulation of neuronal outgrowth, plasticity and survival. Trends in Neurosciences 12, 265-270.

Longhurst, R.S. (1973). Geometrical and Physical Optics, pp. 321-375. Longman Group Ltd: Harlow.

Lumsden, A.G.S. and Davies, A.M. (1983). Earliest sensory nerve fibres are guided to peripheral targets by attractants other than nerve growth factor. Nature 306, 786-788.

Malgaroli, A., Milani, D., Meldolesi, J. and Pozzan, T. (1987). Fura-2 measurement of cytosolic free Ca^{2+} in monolayers and suspensions of various types of animal cells. Journal of Cell Biology 105, 2145-2155.

Manalan, A.S. and Klee, C.B. (1984). Calmodulin. Advances in Cyclic Nucleotide and Protein Phosphorylation Research 18, 227-278.

Martell, A.E. and Smith, R.M. (1974). Critical Stability Constants. Plenum Press, Volume 1, 269-272

Matteson, D.R. and Armstrong, C.M. (1986). Properties of two types of calcium channels in clonal pituitary cells. Journal of General Physiology 87, 161-182.

Mattson, M.P., Dou, P. and Kater, S.B. (1988b). Outgrowth-regulating actions of glutamate in isolated hippocampal pyramidal neurons. Journal of Neuroscience 8, 2087-2100.

Mattson, M.P. and Kater, S.B. (1987). Calcium regulation of neurite elongation and growth cone motility. Journal of Neuroscience 7, 4034-4043.

Mattson, M.P., Taylor-Hunter, A. and Kater, S.B. (1988a). Neurite outgrowth in individual neurons of a neuronal population is differentially regulated by calcium and cyclic AMP. Journal of Neuroscience 8, 1704-1711.

Matus, A. (1988). Microtubule-associated proteins: Their potential role in determining neuronal morphology. Annual Reviews of Neuroscience 11, 29-44.

McCobb, D.P., Best, P.M. and Beam, K.G. (1989). Development alters the expression of calcium current in chick limb motoneurons. Neuron 2, 1633-1643.

Melloni, E. and Pontremoli, S. (1989). The calpains. Trends in Neurosciences 12, 438-444.

Miller, R.J. (1987). Multiple calcium channels and neuronal function. Science 235, 46-52.

Narahashi, T., Tsunoo, A. and Yoshii, M. (1987). Characterization of two types of calcium channels in mouse neuroblastoma cells. Journal of Physiology 383, 231-249.

Nasi, E. and Tillotson, D. (1985). The rate of diffusion of Ca^{2+} and Ba^{2+} in a nerve cell body. Biophysical Journal 47, 735-738.

Nowycky, M.C., Fox, A.P. and Tsien, R.W. (1985). Three types of neuronal calcium channel with different calcium agonist sensitivity. Nature 316, 440-443.

O'Sullivan, A.J., Cheek, T.R., Moreton, R.B., Berridge, M.J. and Burgoyne, R.D. (1989). Localization and heterogeneity of agonist-induced changes in cytosolic calcium concentration in single bovine adrenal chromaffin cells from video imaging of Fura-2. EMBO Journal 8, 401-411.

Pumplin, D.W., Reese, T.S. and Llinás, R. (1981). Are the presynaptic membrane particles the calcium channels?. Proceedings of the National Academy of Sciences (USA) 78, 7210-7213.

Ramon y Cajal, S. (1890). Sur l'origine et les ramifications des fibres nerveuses de la moelle embryonnaire. Anatomischer Anzeiger 5, 609-613.

Regehr, W.G., Connor, J.A. and Tank, D.W. (1989). Optical imaging of calcium accumulation in hippocampal pyramidal cells during synaptic activation. Nature 341, 533-536.

Schliwa, M. (1976). The role of divalent cations in the regulation of microtubule assembly. Journal of Cell Biology 70, 527-540.

Schubert, D., LaCorbiere, M., Whitlock, C. and Stallcup, W. (1978). Alterations in the surface properties of cells responsive to nerve growth factor. Nature 273, 718-723.

Schultz, E., Asai, D.J., Bulinski, J.C. and Kirschner, M. (1987). Post-translational modification and microtubule stability. Journal of Cell Biology 105, 2167-2177.

Silver, I.A. and Erecinska, M. (1990). Intra- and extracellular changes in [Ca^{2+}] in hypoxia and ischemia in rat brain *in vivo*. Journal of General Physiology, in press.

Smith, S.J. (1988). Neuronal cytomechanics: The actin-based motility of growth cones. Science 242, 708-715.

Smith, S.J. and Augustine, G.J. (1988). Calcium ions, active zones and synaptic transmitter release. Trends in Neurosciences 11, 458-464.

Snedecor, G.W. and Cochran, W.G. (1976). Statistical Methods, 6th edn, Iowa State University Press.

Solomon, F. (1979). Detailed neurite morphologies of sister neuroblastoma cells are related. Cell 16, 165-169.

Spector, I. (1981). Electrophysiology of clonal nerve cell lines. In: Excitable Cells in Tissue Culture, eds P.G. Nelson and M. Lieberman, pp. 247-277. Plenum: New York.

Spitzer, N.C. (1979) Ion Channels in Development. Annual Review of Neuroscience 2, 363-397.

Suarez-isla, B.A., Pelto, D.J., Thompson, J.M. and Rapoport, S.I. (1984). Blockers of calcium permeability inhibit neurite extension and formation of neuromuscular synapses in cell culture. Brain Research 316, 263-270.

Suppattapone, S., Worley, P.F., Baraban, J.M. and Snyder, S.H. (1988). Solubilization, purification, and characterization of an inositol trisphosphate receptor. Journal of Biological Chemistry 263, 1530-1534.

Tank, D.W., Sugimori, M., Connor, J.A. and Llinás, R. (1988). Spatially resolved calcium dynamics of mammalian Purkinje cells in cerebellar slice. Science 242, 773-777.

Tessier-Lavigne, M., Placzek, M., Lumsden, A.G.S., Dodd, J. and Jessell, T.M. (1988). Chemotropic guidance of developing axons in the mammalian central nervous system. Nature 336, 775-778.

Thompson, S. and Coombs, J. (1988). Spatial distribution of Ca^{2+} currents in molluscan neuron cell bodies and regional differences in the strength of inactivation. Journal of Neuroscience 8, 1929-1939.

Tosney, K.W. and Wessells, N.K. (1983). Neuronal motility: the ultrastructure of veils and microspikes correlates with their motile activities. Journal of Cell Science 61, 389-411.

Tsien, R.W., Lipscombe, D., Madison, D.V., Bley, K.R. and Fox, A.P. (1988). Multiple types of neuronal calcium channels and their selective modulation. Trends in Neurosciences 11, 431-438.

Tsien, R.Y. (1980). New calcium indicators and buffers with high selectivity against magnesium and protons: design, synthesis and properties of prototype structures. Biochemistry 19, 2396-2404.

Tsien, R.Y. (1981). A non-disruptive technique for loading calcium buffers and indicators into cells. Nature 290, 527-528.

Tsien, R.Y., Pozzan, T. and Rink, T.J. (1982). Calcium Homeostasis in Intact Lymphocytes: Cytoplasmic Free calcium Monitored With a New, Intracellularly Trapped Fluorescent Indicator. Journal of Cell Biology 94, 325-334.

Yamada, K.M., Spooner, B.S. and Wessells, N.K. (1971). Ultrastructure and function of growth cones and axons of cultured nerve cells. Journal of Cell Biology 49, 614-635.

Yamamoto, H., Fukunaga, K., Tanaka, E. and Miyamoto, E. (1983). Ca^{2+}- and calmodulin dependent phosphorylation of microtubule-associated protein 2 and τ-factor, and inhibition of microtubule assembly. Journal of Neurochemistry 41, 1119-1125.

Zuber, M.X., Goodman, D.W., Karns, L.R. and Fishman, M.C. (1989). The neuronal growth-associated protein GAP-43 induces filopodia in non-neuronal cells. Science 244, 1193-1195.